UNIVERSITÀ DEGLI STUDI DI PADOVA

DIPARTIMENTO DI INGEGNERIA INDUSTRIALE

DIPARTIMENTO DI TECNICA E GESTIONE DEI SISTEMI INDUSTRIALI

in collaborazione con

MICROSTRUCTURAL KINETICS GROUP - DEPT. OF MATERIALS SCIENCE & METALLURGY

UNIVERSITY OF CAMBRIDGE

Tesi di laurea magistrale in ingegneria dei materiali

REJUVENATION OF METALLIC GLASSES BY CRYOGENIC CYCLING

Relatore: Prof. Franco Bonollo

Correlatori: Prof. A. Lindsay Greer

Dr. YongHao Sun

Dr. Sarig Nachum

Laureando: Alessandro Checchi

ANNO ACCADEMICO 2014-2015

TABLE OF CONTENTS

1. INTRODUCTION

The development of new alloys with improved properties has often been a matter of increasing the departure from equilibrium, whether it is in the final product or during manufacturing processes. Thanks to technological advancements, with whom was possible to achieve even larger departures from equilibrium, in the 1950s at Caltech an entirely new class of alloys, metallic glasses, was discovered. As their name suggests, metallic glasses are composed of metallic atoms that lack of long-range order, typical of crystalline metals, their structure is indeed amorphous like the one of other more common glasses, window glass for example. Since their discovery great interest built up and great efforts were made to study and improve physical properties and forming ability, resulting, nowadays, in the possibility to manufacture several compositions of metallic glasses in bulk shape.

1.1 Metallic glass nature: glassy state, thermodynamic and kinetic properties

The glassy state can be defined from a structural point of view almost identical to a liquid but with the resistance to shear deformation characteristic of a solid. In fact glasses are formed when, during cooling, crystallization process is surpassed and the liquid uniformly congeals into solid state. A way to achieve the glassy state involves the increment of the cooling rate.

Many amorphous alloys exist as well as a wide variety of methods to obtain them. Not every amorphous alloy are glass though. On the structural point of view amorphous and glassy solids can be significantly different. Emblematic is the case of silicon: liquid silicon has a high density and it is metallic, while amorphous silicon, usually produced by vapour deposition as well as by solidification from the liquid, has local tetrahedral coordination with covalent bonding, identical to crystalline silicon [1]. Therefore solid amorphous silicon is rather different compared to liquid silicon and its hypothetical glassy state.

We proceed to analyse in deep the structure of a glassy state. Figure 1.1.1 shows the temperature dependence of some key properties, specific enthalpy and specific volume, for

a liquid at constant pressure. This figure is crucial in order to understand the nature of physical changes that occur when a liquid is cooled into a crystalline or glassy state.

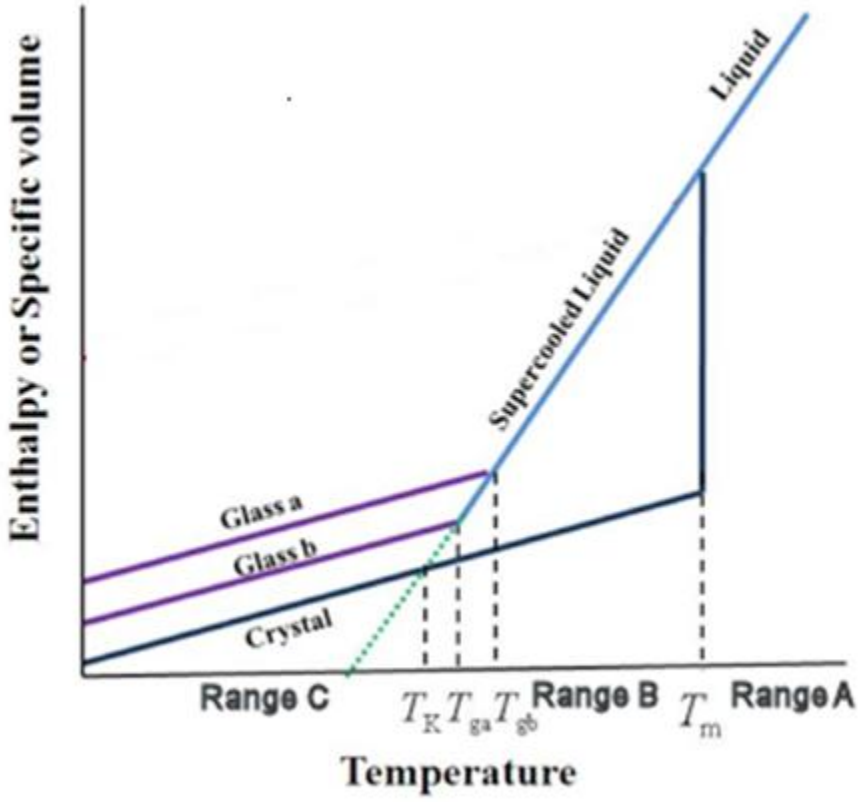

Figure 1.1.1: Representation of specific volume, *v*, and specific enthalpy, *H*, of liquid, glass and crystal as a function of temperature, at constant pressure. The crystal forms, at the freezing temperature, T_m, when the liquid is slowly cooled. A glass forms by rapid cooling and the glass transition from liquid to solid occurs at T_g. A glass formed on fast cooling (a) has higher values of *v* and *H* than a glass (b) formed on slower cooling. T_K is the Kauzmann temperature.

Considering range A, above the melting temperature the melt is in equilibrium. (Even if metastable states are very rare in this range, it is not impossible to superheat any crystal, especially metallic crystals above their thermodynamic melting point [2]).

In defining the boundary between ranges A and B, T_m, melting temperature, is used. In this case Figure 1 refers especially to alloys without a solidus-liquidus gap.

At this stage, entering range B, the liquid can follow two possible distinct paths in relation to the cooling rate that is subjected to.

If cooling rate is relatively small the liquid would prefer to follow the equilibrium route and starts crystallize. This process, dark blue line in figure 1.1.1, is accompanied by a sharp and

rapid drop in the specific volume (and specific enthalpy) as a much more stable state, crystalline state represents the system absolute free-energy minimum, is reached. Additional decrease in temperature below T_m leads to a slow decrease of the specific volume related to its thermal expansion coefficient.

On the other hand, when sufficient cooling rate is applied, the liquid undergoes no sharp change and enters the thermodynamically supercooled region, light blue line in figure 1.1.1. In this range, at least at the higher temperatures, the liquid has low viscosity, and crystallization (driven by the supercooling) can be avoided only because the cooling rate is such as to prevent nucleation of the crystalline phase. But, as the temperature is further decreased, the liquid viscosity increases rapidly and atomic mobility as well as crystallization are blocked. A glass can still be formed even in the presence of nuclei because the low atomic mobility blocks the crystal growth [3].

At all temperature in range B the atomic mobility is adequate for the liquid to remain in configurational equilibrium [3], that means we can reach different glassy states (in the figure *a* or *b*) in relation to the severity of the cooling process, thus different glass transition temperatures T_g (in the picture $T_{g\,a}$ and $T_{g\,b}$) can be defined. The slower the liquid is cooled down and the longer is the time available for configurational re-ordering of the atoms that tends to minimum free energy state, in this case the crystal lattice. Consequently more stable (lower enthalpy) and denser glassy structures, lower T_g, can be reached for lower cooling rates. At the extreme side, when the supercooled liquid curve meets the crystalline curve, “ultrastable glasses” can be formed; a relatively new class of metallic glasses, obtained by vapour deposition that show a notable thermodynamic and kinetic stabilities similar to glasses aged for thousands of years [4].

It is important to recognize that T_g is not a thermodynamically defined temperature; its location is determined only by kinetics. Therefore a common definition is related to the viscosity of the supercooled liquid. In Figure 1.1.2 the same graph presented above is accompanied by others that show temperature dependence of several fundamental properties of the material.

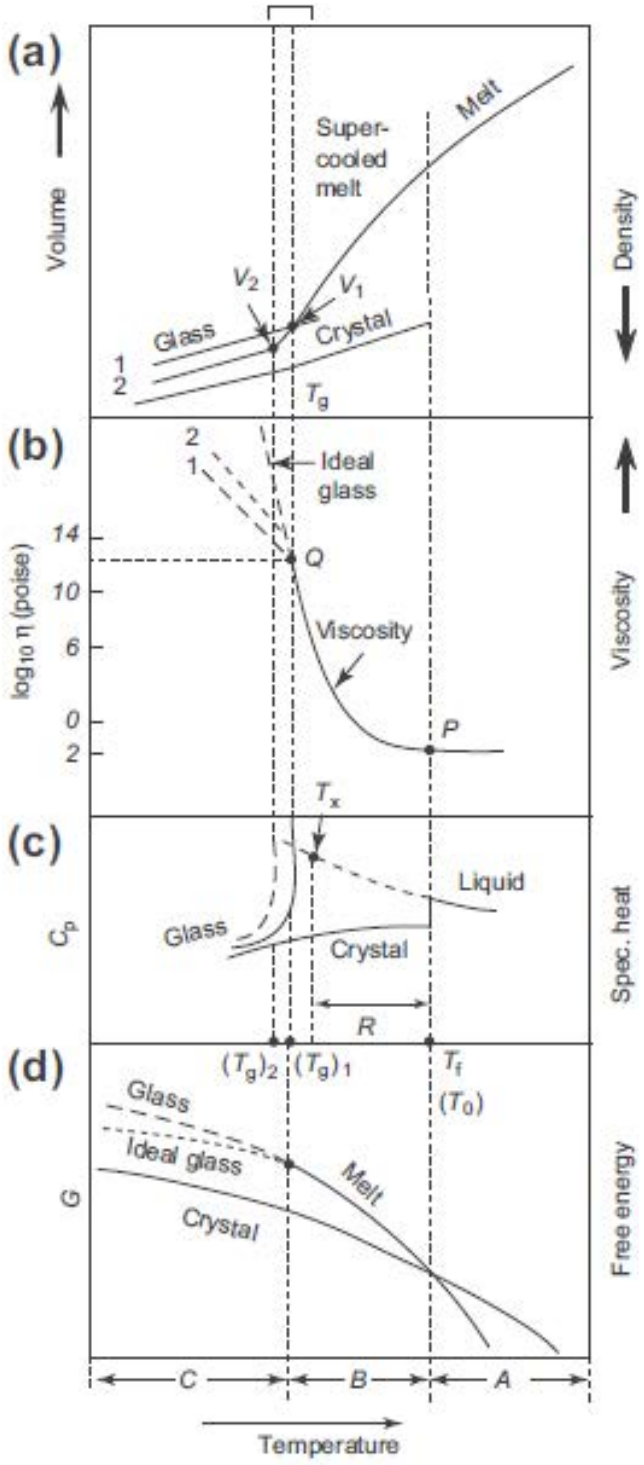

Figure 1.1.2: Variation of several proprieties of the material with the temperature. Three different ranges are marked by the glass transition temperature, T_g, and by the melting temperature T_m [3].

Considering Figure 1.1.2 b) in range B the viscosity varies over fifteen orders of magnitude and the nature of the glass transition is strongly related to this aspect, as said before. Experimental evidences for different materials, have shown that T_g is close to the temperature at which viscosity, η, reaches the value of 10^{12} Pa s. This viscosity value then represents a kinetic limit above that the atomic motion is so slow that there are no further

configurational changes with the proceeding of the cooling. Hence, in the glassy state configurational changes do not occur with decreasing of temperature below T_g so glass proprieties, compared to liquid, have slightly weak temperature dependence, approximately matching the behaviour of the crystal [3].

Interesting studies about the central kinetic role played by the viscosity in the glass transition were conducted by Angell [5]. He defined two types of glass forming liquids: "strong" and "fragile", basing this classification on the different behaviour during cooling. Strong liquids, such as network formers like SiO_2, have a near Arrhenius dependence of viscosity. Fragile liquids, like o-terphenyl (OTP), show a strongly non-Arrhenius temperature dependence of viscosity and their molecules exert largely non-directional, dispersive forces on each other.

This situation is well presented in Figure 1.1.3 [6], showing that metallic glasses lie in-between the two example proposed by Angell.

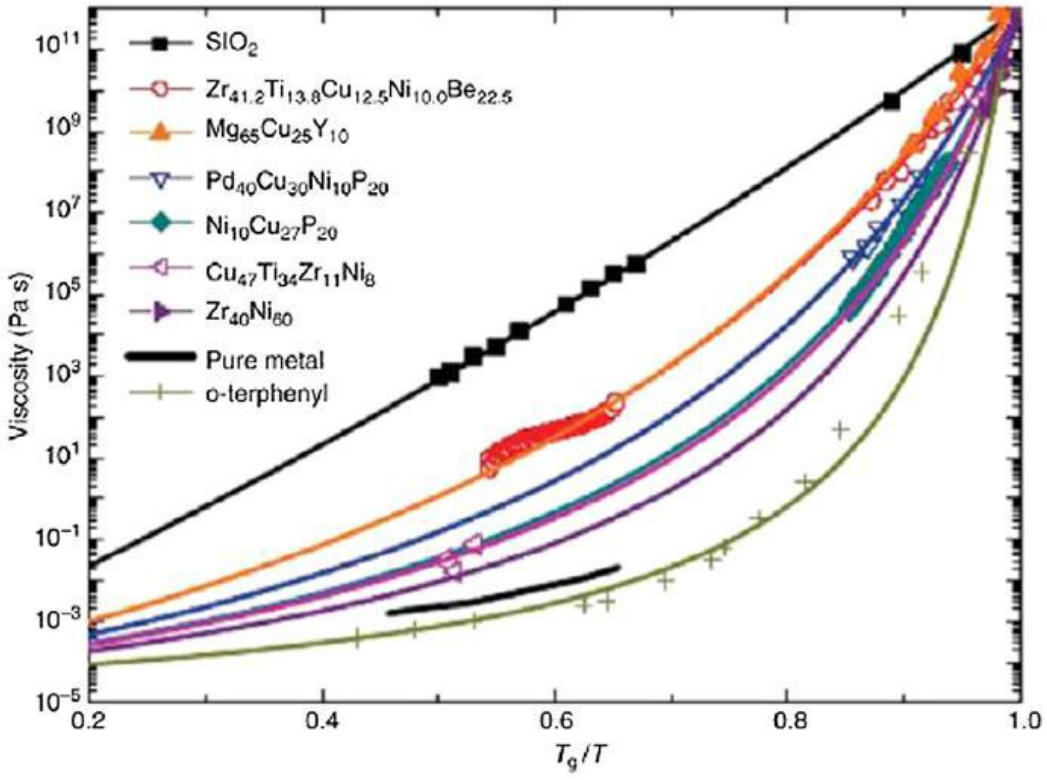

Figure 1.1.3: Viscosity of glass forming liquids as a function of inverse temperature, normalized on the glass transition temperature, *Tg*. The metallic alloys are intermediate between strong network-forming liquids and fragile liquids.

It has to be specified that glass transition and consequent glass formation are not viscosity and kinetics dependent only. There is a tendency for stronger liquids to have better glass

forming ability (GFA) but the correlation is far from perfect. Thermodynamics has to be taken into account, for example the composition $Pd_{40}Cu_{30}Ni_{10}P_{20}$ possesses the highest forming ability but clearly is not the strongest of the liquids in figure 1.1.3. That kinetics features are not the only important part is clearly shown in Figure 1.1.4. Gibbs free-energy driving force for solidification for different metallic glasses is presented.

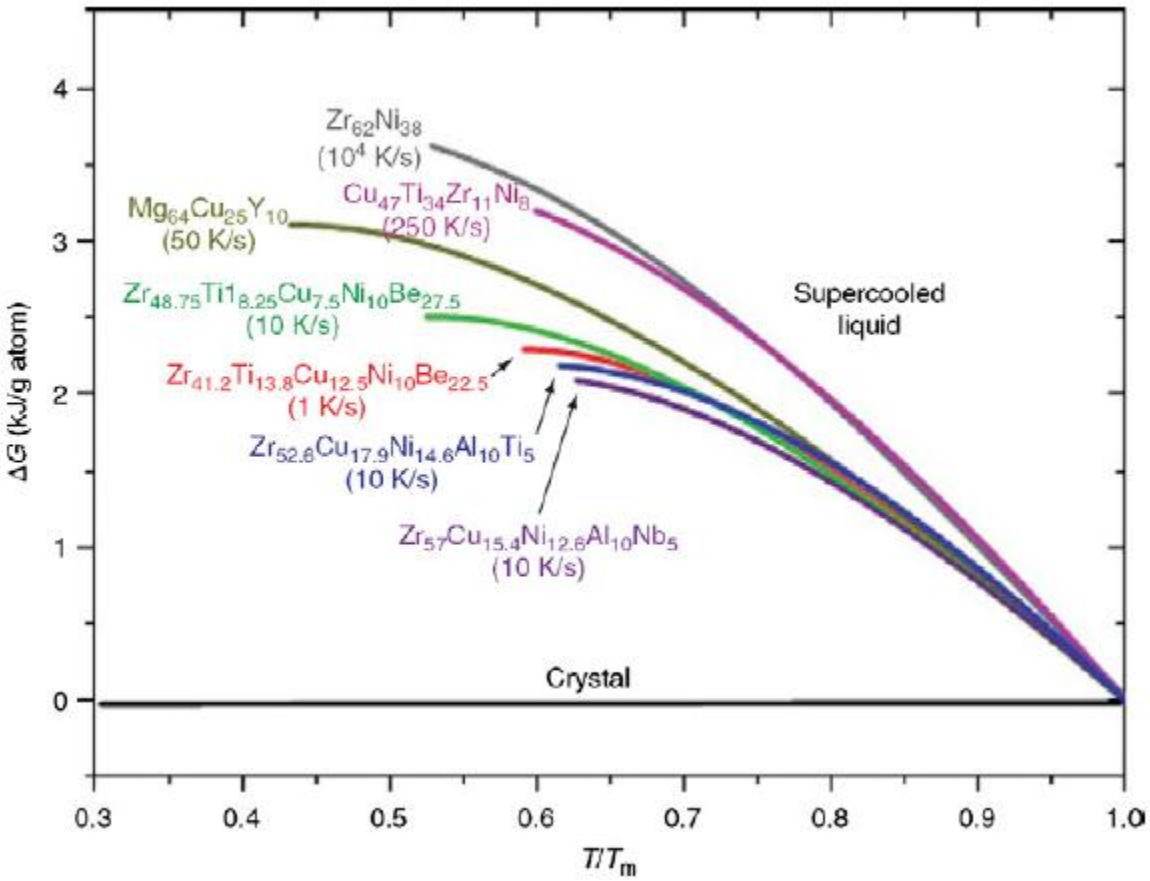

Figure 1.1.4: The difference in Gibbs free energy between the supercooled liquid of glass-forming systems and the crystalline phase.

For pure metals it is generally considered that this ΔG should increase linearly with supercooling ($T_m - T$). For glass-forming liquid instead it is clearly observable that ΔG rises less than linearly. Also at lower temperatures some curves present a nearly zero-slope, and being the slope proportional to ΔS, this means that the liquid state about to become a glass has entropy essentially equal to that of the crystal, showing an apparently unexpected high degree of order [7]. This fact is also confirmed by the large excess specific heat of liquid in respect to crystal or glass, figure 1.1.2 c).

1.2 Metallic glasses production

Historically metallic glasses (MGs) are produced from cooling rapidly enough the liquid phase and this is still the main production route. Some of these techniques involves melt-spinning, atomization, scanned laser or electron beam, fluxing, solidification in free fall.
However, other techniques have been explored involving *amorphization* of solid crystalline materials, for example irradiation, mechanical methods and chemical reactions. Measurement of properties suggest that amorphous metallic phases from other production methods are similar to glasses produced by cooling the liquid [3].
To be mentioned also other techniques concerning chemical methods (electrodeposition, hydrogenation) and physical methods (PVD, sputtering PVD).

1.2.1 Production of Ribbons: techniques

The most diffuse techniques are melt-spinning and planar flow casting. These techniques were the first to be massively used, since the 1950s, because they allow extremely high cooling rate, of the order of 10^5-10^6 K/s. The result products are thin, 10-100 μm, ribbons and foils.

The most commonly melt-spinning configuration used is called chill-block melt spinning. In the process a small quantity of the alloy is melted inside a crucible or by levitation methods, and then the molten metal is ejected by pressurization through a fine nozzle onto a fast-rotating, cold copper wheel sink where the jet is reshaped and allowed to solidify. As solidification starts, the ribbon is expelled from the surface of the fast-rotating heat sink [8].
In Figure 1.2.1 it is possible to see a schematic representation of this method.

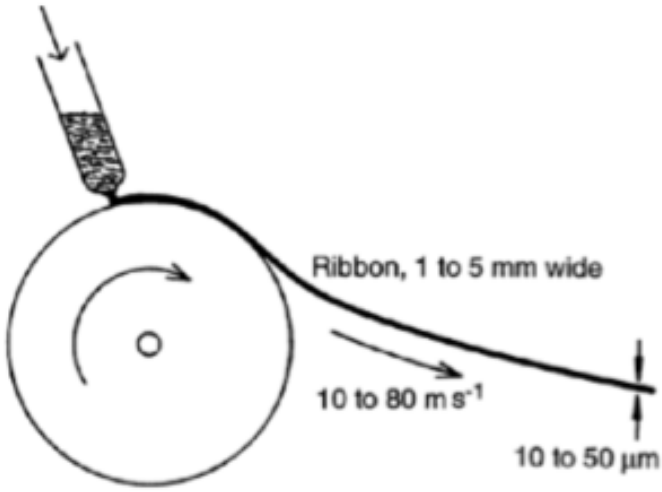

Figure 1.2.1: Schematic illustration of the typical melt-sinning process for a ribbon. Noble gas is used to press the melt in order to avoid any contamination.

The standard dimensions of the resulting ribbons are about 2-55mm in width, whereas the thickness varies in the range of 10-200µm. To extend more the ribbon width planar flow casting can be used.

The process equipment and procedures of the two methods are similar. They differ in the design and location of the crucible. Usually, melt-spinning crucibles have a circular orifice, mounted some distance above the cooling wheel, from which a stream of liquid metal is ejected and impinges onto the rotating cooling wheel. In contrast, the crucibles used for the planar-flow casting have rectangular nozzle and are located close to the rotating cooling wheel.

1.2.2 Production of bulk metallic glasses

Bulk metallic glasses (BMGs) are those metallic glasses that have a section thickness of at least a few millimeters [8]. It is clear that to be taken into consideration for multiple applications metallic glasses production should be capable of synthetizing various dimensions and shape, not only ribbons or foils. Currently, as well as in the last decades, research focuses on expanding the range of compositions that do not require rapid quenching and that permit glass formation in bulk. Hence, research and studies have been

conducted on glass forming ability and its prediction, i.e. quantification of critical cooling rate for glass formation.

The main criteria to drive research was formulated by Turnbull [9]: crystallization can happen only in the temperature region between T_m and T_g , the closer these two are the greater the possibility to form a glass, avoiding crystallization.

Binary and multicomponent alloys that show eutectics are then a possible optimum choice for good glass forming alloys, as thermal properties, such as T_m , can be deeply influenced by composition. Figure 1.2.2.1 shows for the binary system Pd-Si composition dependence of T_m a), T_g b) their ratio and the calculated critical cooling rate, R_c c).

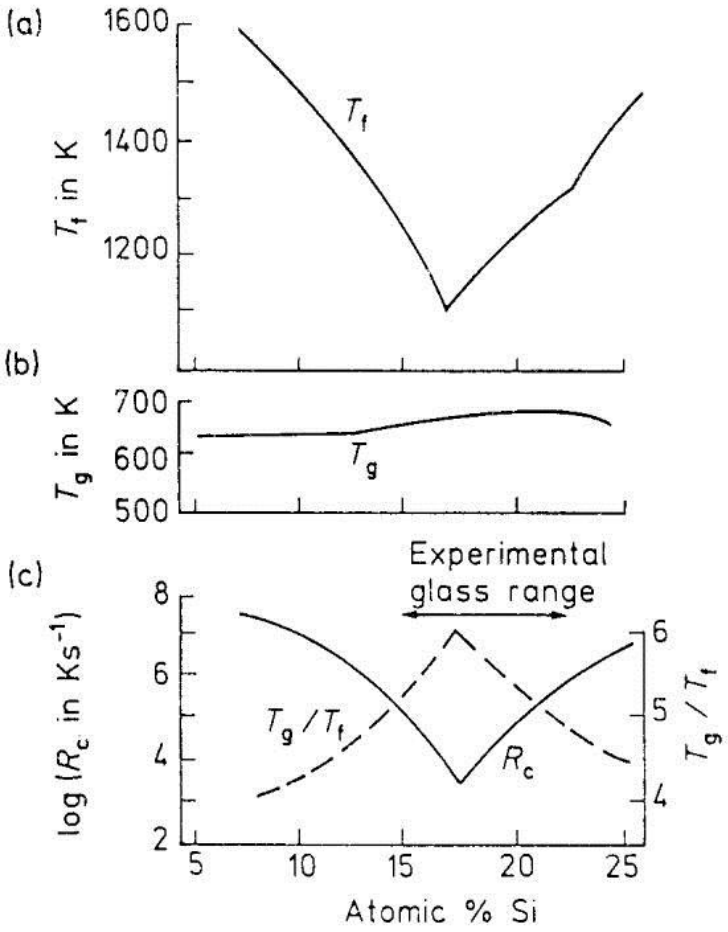

Figure 1.2.2.1: Trend of the freezing temperature, Tf , the glass-transition temperature, Tg, the ratio Trg = Tg/ Tf, and the calculated critical cooling rate for glass formation, Rc, as function of the range of compositions in the Pd-Si alloy system.

It is clear that critical cooling rate has a minimum where T_m has a minimum itself. Thus the search for glass-forming system is the search for deep eutectics.

Chemical elements of interest and their role in glass-forming binary systems are presented in Table 1.2.2.1 and Table 1.2.2.2.

Abbreviation	Description	Examples
AM	Alkali and alkaline-earth metals	Mg, Ca, Be
SM	Semi- or simple metals	Al Ga
ETM	Early transition	Ti, Zr, Hf, Nb, Ta, Cr, Mo, Mn
LTM	Late transition metals	Fe, Co, Ni, Cu, Pd, Pt, Ag, Au, Zn
RE	Rare-earth metals	Sc, Y, L, Ce, Nd, Gd
NM	Metalloids and non-metals	B, C, P, Si, Ge

Table 1.2.2.1: Classification of common constituent elements in metallic glasses

Prototype	Base metal	Examples
LTM+NM	LTM	Ni–P, Pd–Si, Au–Si–Ge, Pd–Ni–Cu–P, Fe–Cr–Mo–P–C–B
ETM+NM	ETM	Ti–Si
ETM+LTM	ETM or LTM	Zr–Cu, Ni–Zr, Ni–Nb, Ti–Ni, Zr–Cu–Ni–Al, Zr–Ti–Cu–Ni–Be
RE+LTM	RE	Gd–Fe
SM+RE	SM or RE	Al–La, Ce–Al, Al–La–Ni–Co, La–(Al,Ga)–Cu–Ni
AM+LTM	AM	Mg–Cu, Ca–Mg–Zn, Ca–Mg–Cu

Table 1.2.2.2: Classification of typical metallic glasses based on binary prototypes

Considering multicomponent alloys even deeper eutectics may be achieved, and this is the case of BMGs.

GFA is often discussed in terms of three “empirical rules” proposed by Inoue [11]: 1) the alloy system should have three or more elements. 2) these elements should have a size mismatch (atomic diameter) exceeding 12%. 3) these elements should show negative heat of mixing with each other. In the following table, Table 1.2.2.3, are presented some compositions of BMGs that can be cast fully glassy.

BMGs do not need rapid quenching, they can be formed with cooling rate of the order of 10^3 - 1 K/s [8]. A number of different techniques have been developed to synthesize BMG

alloys. These developments have occurred in different laboratories, and sometimes, for some specific applications or materials: water quenching, high-pressure die casting, copper mold casting, suction-casting and squeeze casting are the most important.

The simplest one is the water-quenching method. The cooling rates achieved by this method are inherently dependent on the heat transfer efficiency, the size of the specimen, its heat transfer properties, and they have been usually reported to varied between 10 and 100 K/s [12].

Base metal	Composition	Critical diameter (mm)	Production method
Pd	$Pd_{40}Ni_{40}P_{20}$,	10	Fluxing
	$Pd_{40}Cu_{30}Ni_{10}P_{20}$	72	Water quenching
Zr	$Zr_{65}Al_{7.5}Ni_{10}Cu_{17.5}$,	16	Copper mold
	$Zr_{41.2}Ti_{13.8}Cu_{12.5}Ni_{10}Be_{22.5}$	25	Copper mold
Cu	$Cu_{46}Zr_{42}Al_7Y_5$, $Cu_{49}Hf_{42}Al_9$	10	Copper mold
Rare earth	$Y_{36}Sc_{20}Al_{24}Co_{20}$	25	Copper mold
	$La_{62}Al_{15.7}Cu_{11.15}Ni_{11.15}$	11	Copper mold
Mg	$Mg_{54}Cu_{26.5}Ag_{8.5}Gd_{11}$	25	Copper mold
	$Mg_{65}Cu_{7.5}Ni_{7.5}Zn_5Ag_5Y_5$	14	Copper mold
Fe	$Fe_{48}Cr_{15}Mo_{14}Er_2C_{15}B_6$	12	Copper mold
	$Fe_{41}Co_7Cr_{15}Mo_{14}C_{15}B_6Y_2$	16	Copper mold
Co	$Co_{48}Cr_{15}Mo_{14}C_{15}B_6Er_2$	10	Copper mold
Ti	$Ti_{40}Zr_{25}Cu_{12}Ni_3Be_{20}$	14	Copper mold
Ca	$Ca_{65}Mg_{15}Zn_{20}$	15	Copper mold
Pt	$Pt_{42.5}Cu_{27}Ni_{9.5}P_{21}$	20	Water quenching

Table 1.2.2.3: Representative bulk metallic glass compositions

The alloy is sited inside a quartz tube, where the flux treatment is provided (addition of an oxide like B_2O_3 that improves the glass forming ability by removing the impurities). It is then heated to a temperature above the liquidus temperature of the alloy in order to completely melt it. After that the quartz tube containing the molten alloy is quenched into flowing or agitated water.

High-pressure die casting has been developed to reach high solidification rates, and it is common among industries. Figure 1.2.2.2 shows the schematic of the high-pressure die-casting equipment designed and used to synthesize Mg-based BMGs [8]. The metallic alloy is melted in the sleeve under an argon atmosphere with a high-frequency induction coil. After the alloy is melted, the plunger is moved by hydraulic pressure into the copper mold, and the molten liquid solidifies once it comes into contact with the highly conductive copper mold [8].

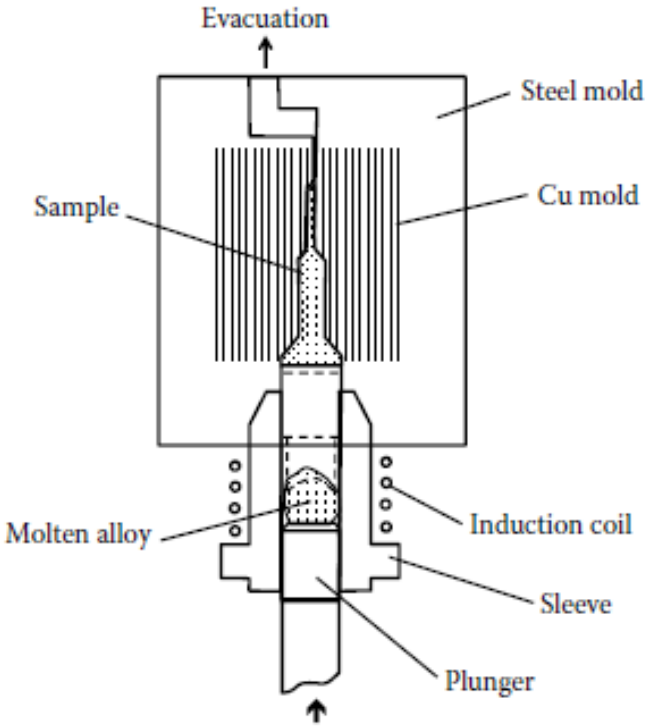

Figure 1.2.2.2: Schematic diagram of the high-pressure die casting process.

This equipment guarantees a rapid solidification completed in few milliseconds, and also a high productivity.

The moderately high cooling rate, around 10^3 k/s, is due to the contact between the melt and the mold that results in a large heat transfer coefficient at the die/liquid interface. Moreover casting defects, like shrinkage holes due to liquid contraction during the solidification process, are reduced, and it is possible to produce complex shapes also with high viscosity liquids [8], [12].

Copper mold casting appears to be perhaps the most common and popular method of producing BMGs alloys. Figure 1.2.2.3 shows a schematic representation of the equipment normally used for copper mold casting.

The alloy is melted and poured into a copper mold where it solidifies quickly because of the rapid heat extraction by the metal mold. The starting raw materials for alloy preparation could include either pure metals or master alloys of some of the elements and/or combinations of them. Melting is carried out generally by induction in a specific container.

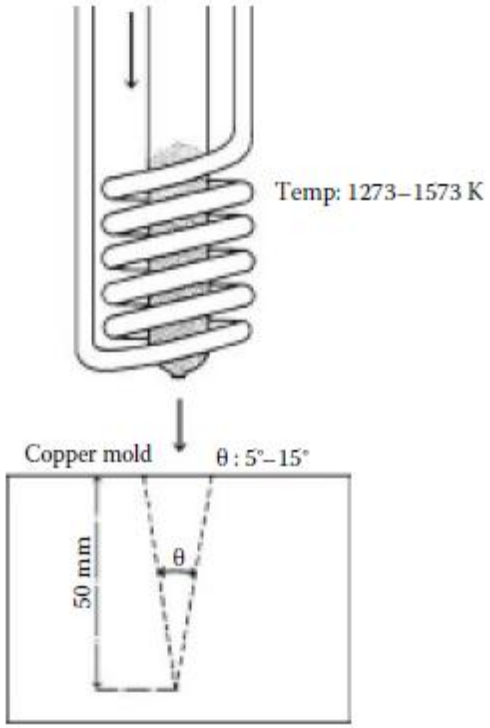

Figure 1.2.2.3: Schematic diagram of the equipment used to prepare a bulk metallic glass by copper mold wedge-casting technique

The molten alloy is then poured into a copper mold, generally a low pressure is provided to aid. The casting can be done in air or vacuum, inert atmosphere, or under argon, in case oxidation has to be avoided.

The mold used can take different forms. The most common and simple form of the mold has a cylindrical or rod-shaped cavity, but it could have also different internal diameters. A useful type of mold is a wedge- or cone-shaped mold, figure 1.2.2.3. The advantage of using the wedge-shaped mold is the possibility to obtain specimens of different diameters in one single casting [13].

Another popular method for synthetizing bulk metallic glasses is the suction-casting [14]. The principle is to suck the melted alloy in a die cavity using a pressure differential.

Squeeze casting [15], well-known technique for standard crystalline alloys, is also a successful method used to produce bulk metallic glasses with very low porosity. The squeeze-casting process consists in the solidification of the melted alloy under a high pressure within a closed die by utilizing a hydraulic press.

1.3 Metallic Glass Structure

As expressed in previous paragraphs metallic glasses do not have long-range order and therefore their distinctive feature is that they do not present microstructure. There is no crystal lattice to which defects such as grain boundaries or dislocation can be defined [3]. Glasses, and MGs in particular, though lacking periodicity do have structure, they are not well described as a random ensemble of atoms. In fact, considering figure 1.1.2 and 1.1.4, it is clear that during glass transition a certain degree of ordering is present.

Metallic glass structure for these reasons has been a long-standing mystery. On the one hand, they are amorphous materials with no long-range structural order; on the other hand, topological and chemical short-to-medium range order is expected to be pronounced in these alloys, due to their high atomic packing density and the varying chemical affinity between the constituent elements. The unique internal structure of MGs underlies their interesting properties, which render MGs potentially useful for various applications [10]. Many studies have been made in order to clarify the intimate structure of metallic glasses and much effort has still to be spent. For example, how the structure differs in different MGs and changes with composition, temperature, and processing history, and more importantly, how the structure influences the properties of MGs, are still unresolved questions.

Good progress has been made in elucidating the nature of metallic glasses short-range order (SRO), i.e. the structure at the level of nearest-neighbor atomic coordination. The nature of their medium-range order (MRO) , i.e. positional correlations over 1-2 nm, is more difficult to characterized and remain poorly understood.

Although every distinct metallic glass compositions can be different from the others, there are many common features which understanding is crucial. For example, annealing to obtain a little higher density is associated with a viscosity increase of some five orders of magnitude in a rapidly quenched metallic glass [16].

Consequently it is central to understand the links between structure and properties.

1.3.1 Structural characterization

The problem of determining the structure of a crystal consists of identifying the coordinates of all the atoms in the unit cell, and in principle this problem is precisely resolvable. Contrarily, for a glass, the structure can be described only on a statistical basis: there are no unit cells and the environment of different atoms of a given species are necessarily diverse. Almost all structural characterization analysis have been based on pair distributions function (PDFs) [17], because they can be determined from scattering experiments. PDFs give a measure of the probability of finding an atom center at a distant *r* from an average central atom. Thus, only statistical information about distance is provided, and this is insufficient to specify the structure. (angular distribution can be easily extracted from structural models, but cannot be determined from conventional scattering experiments.) [3]. Determination of glassy structure then derives from comparison between PDFs measured experimentally with ones calculated from trial structural models.

Even without such comparison, the measured PDFs reveal basic feature of metallic glass structure [18,19]. The first peak in the radial distribution function (RDF) indicates the nearest neighbor separation distance and the area under the peak gives the average coordination number. The latter is in general relatively high and indicates that MGs are densely packed, as expected by supercooled liquid properties.

It is also found, for the system metal-metalloid $Co_{81}P_{19}$, considering partial PDFs, that the distribution of different elements can be far from random [3,20], metalloid neighbours appeared completely avoided. And that seems a general feature for metal-metalloid alloys, at least for relatively small content of metalloid elements [21].

More recently other characterization techniques have been used in order to study the local atomic environment; for example XAFS, NMR, TEM, Mossbauer spectroscopy. Local symmetries and crystal-like structural units and local chemical order are found [3], confirming the presence of short-range order for a variety of compositions.

1.3.2 Structural models

The first structural model suggested for metallic glasses was based on “microcrystallites” or nanocrystallites. The idea was that nanocrystalline solid alloys were not glasses but simply polycrystalline solids with a very small grain size. Nowadays there is no longer doubt on the glassy nature of metallic glasses. Calorimetric studies are just an example in which the difference between polycrystalline material and glassy alloys is clearly presented. Indeed, on annealing nanocrystalline solids transform to a polycrystalline aggregate of larger grain size by a process of continuous grain growth rather than by nucleation and growth of crystals as in a glass [22]. It is intrinsic to a glass that the structure is hereditary from the liquid it derives from. An interesting basic model is the one developed by Bernal for liquids [23]. It consists in thinking to the structure of a pure metal liquid as a packing of hard spheres all of the same diameter, realized physically by kneading a large population of steel balls in a bag. This dense random packing (DRP) is statistically reproducible and the structure can be made by connecting only five fundamental polyhedra represented in Figure 1.3.2.1.

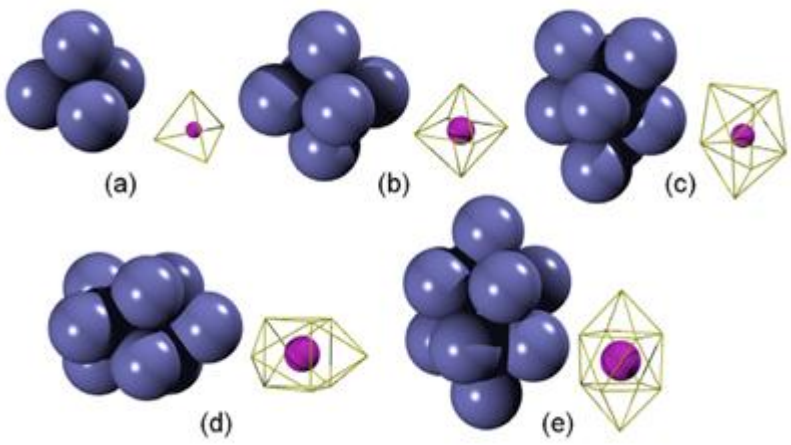

Figure 1.3.2.1: Polyhedra formed by dense random packing of hard spheres, according to Bernal: (a) tetrahedron (b) octahedron (c) tetragonal dodecahedron (d) trigonal prism capped with three half octahedra (e) Archimedean antiprism capped with two half octahedra.

It is interesting that the smaller polyhedra are tetrahedral and octahedral and in the dense random packing distribution are the great majority.

Although the dense random packing represents an interesting and intuitive model it has significant prediction limits; for example it considers only sphere of one size. (Also if the packing is dense it is unlikely to be random.) It fails to predict some fundamental aspects of

the glassy structure such as the avoidance of metalloid-metalloid nearest neighbours, evidenced by Sadoc and Dixmier [20].

In many systems it is interesting to analyze the order in terms of atom-centred clusters. The ratio of the radii of the solute atom at the centre of the solvent atoms around it determines how many solvent atoms will fit in the coordination shell. Typically in metallic glasses coordination numbers vary from 8 to 20.

In Figure 1.3.2.2 a simulated structure of $Ni_{81}B_{19}$ glass is shown [24]. In this case, such as the one mentioned above for Co-P based metallic glasses, metalloid-metalloid nearest neighbours are not found, in fact the external shell of each cluster is composed only by nickel atoms. In other cases, Cu-Zr glasses shell may contain a mixture of atom types.

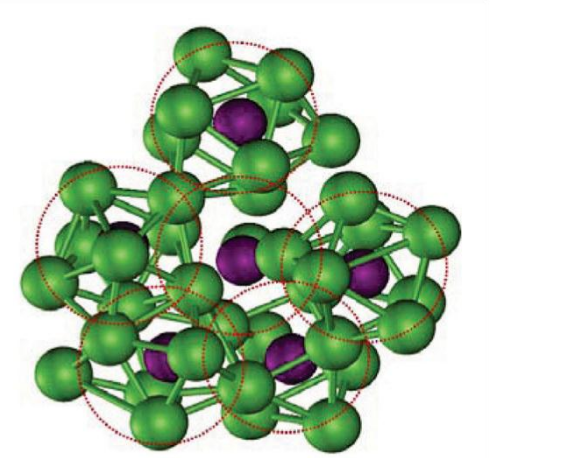

Figure 1.3.2.2: Structure of $Ni_{81}B_{19}$ metallic glass obtained from an ab-initio molecular-dynamics simulation, showing quasi-equivalent solute-centered clusters. The chemical ordering is such that solute boron atoms (purple) are fully coordinated by solvent nickel atoms (green) and do not make contact with each other.

It is evident that there are radius ratios and relative populations of atomic species of different size that will give particularly stable clusters and efficient packing, as it is represented in Figure 1.3.3 [25]. Such considerations underlie the efficient cluster packing model and related approaches that have successively rationalized compositions that favour eutectics and a better glass forming ability [24]–[26]. A structure assembled from such clusters (corner sharing) has MRO of around 1nm and gives excellent fits to scattering data [29].

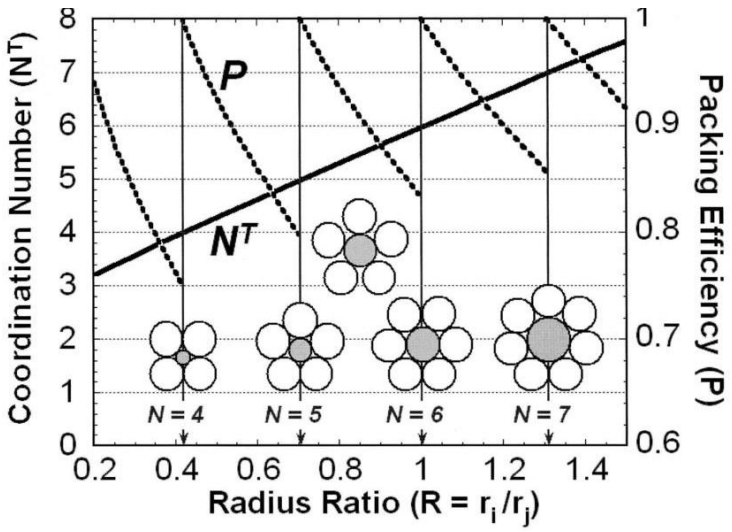

Figure 1.3.2.3 : The theoretical coordination number N^T (continuous line) and packing efficiency P (dotted line) as function of the radius ratio R for two-dimensional clusters of circles. Four two-dimensional configurations with a packing efficiency of 1.are represented for coordination numbers 4, 5, 6 and 7. In the centre a cluster with a packing efficiency less than one is also presented.

Already in 1952 Frank [27] proposed that crystal nucleation in supercooled liquid metals arises because of the atomic packing in the liquid is icosahedral and therefore incompatible with a crystal structure.

Recent scattering experiments and molecular dynamics simulations [28] have shown that the icosahedral clusters fraction, present in a supercooled liquid, increases sharply on cooling toward the glass transition temperature and this fact appears closely associated with the rise of viscosity that brings to glass formation. In addition the simulations also show that the least mobile atoms are those in icosahedral clusters.

1.3.3 Inhomogeneity in metallic glass

Relatively recent new aspects regarding inhomogeneity in metallic glasses have been discovered and some words have to be spent since this topic has a crucial role for results exposed in this thesis.

It has become more and more evident that metallic glasses can be inhomogeneous on different scales, from a nanometer scale, through micrometer scale, to macroscopic level due to locally different cooling rates in different zones of the sample.

Nanometer and micrometer scale inhomogeneity are the more interesting ones as they are not normally expected in an amorphous material. In a recent work Ichitsubo et al. [30] claims that a nanoscale heterogeneity on $Pd_{42.5}Ni_{7.5}Cu_{30}P_{20}$ glass is existent, showing that the sound velocity was greater for nanometer wavelength than for millimeter wavelength (Ichitsubo tested also other compositions in later works [32] confirming the same result). A possible structural model that could match the result was considering a glass as a mix of two different regions: strongly bonded regions and weakly bonded regions (also called respectively solid-like regions and liquid-like regions), showed in Figure 1.3.3.1 [30].

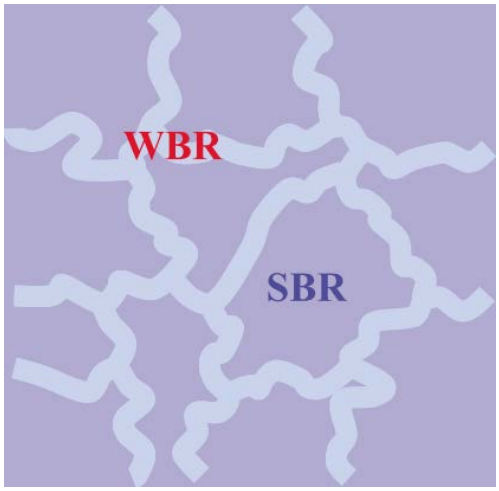

Figure 1.3.4 : Microstructural model of fragile Pd-based metallic glass [30]; WBR: weakly bonded region; SBR: strongly bonded region.

Accordingly with this model, it has been shown that sound velocity of nanometer-order wavelength, which mainly represents the elasticity of predominant strong bonded regions, is faster than that of a millimeter-order wavelength, reflecting the macroscopic elastic stiffness of the overall substance including both kinds of regions.

Metallic glass, has already been shown in previous paragraph, are not completely disordered, and on atomic scale there is tendency to find precise arrangements, clusters, that reminds of structural unites. Ichitsubo discovery though is on a different level as it implies the presence of a microstructure very similar to microcrystalline alloys with crystal grains and grain boundaries.

Other studies on inhomogeneity with atomic force microscope [31], mapped the distribution of elastic constants in the space in a $Pd_{42.5}Cu_{30}Ni_{7.5}P_{20}$ metallic glass. They identified a broad

range of the elastic indentation modulus in comparison with their crystalline counterparts, where, thanks to a long range order, a much more unified elastic modulus is expected.

1.3.4 Structural relaxation

As briefly exposed before, annealing a glass brings its structure in a more relaxed configuration characterized by a small negative change in its (specific) volume, slight increase in density. Considering the hypothetical two states, (a) and (b), represented in Figure 1.1.1, the annealing of a glass in the state (b) at a reasonably high temperature close to $T_{g\,b}$ bring its structure towards the state (a). From this essential diagram it is immediately clear that enthalpy and specific volume decreases. In general when glass is annealed close to its glass transition temperature, T_g, many physical and mechanical properties change as the glassy structure evolves toward the metastable equilibrium state of the supercooled liquid at that temperature. This change in structure and properties is generally called relaxation.

One description of this structural process is possible in terms of free volume.

An as-quenched glass has distributed excess “free” volume that decreases on annealing and bring to densification. This parameter can be used to discriminate a particular glassy state compared to another one and is fundamental to emphasize the importance of the volume in controlling the atomic mobility in the glass. In figure 1.3.4.1 is presented the interdiffusivity in a Fe-Ti amorphous multilayers function of the volume decrease [35].

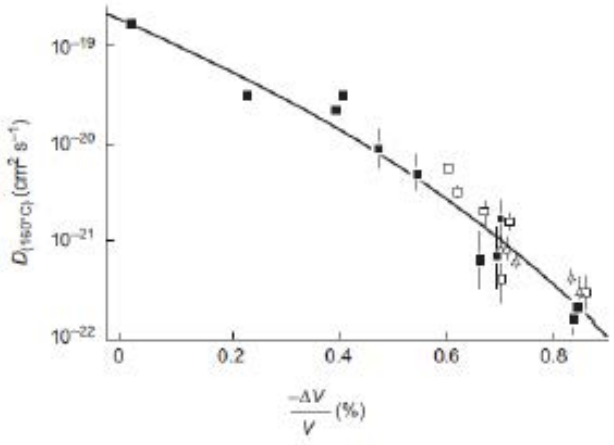

Figure 1.3.4.1: The interdiffusivity in a Fe-Ti amorphous multilayer at 160°C versus the decrease in volume ΔV/V. Interdiffusivity is determined by the change in X-ray modulation peak intensity upon annealing and structural relaxation is determined by the shift in X-ray peak position corresponding to the densification.

This aspect suggests an important fact always true for metallic glasses: while the structural changes associated to relaxation, can be barely detectable, the associated variation in properties can be enormous, a few magnitude orders [35].

(At the atomic level, free-volume is not uniformly distributed; where it is concentrated atoms are in hydrostatic tension. Egami has pioneered MGs structure description in terms of atomic-level stresses. A more relaxed glass has fewer anomalously short or long interatomic separations and thus a narrower spread of atomic level stresses [34].)

Depending on annealing temperature different metastable equilibrium states are reached in different times. At a lower annealing temperature the structural relaxation is initially slower but the total extent that can be achieved by this process, measured by the change in properties, is bigger. This interesting behaviour is represented for Curie temperature in Figure 1.3.4.2, for a $Fe_{80}B_{20}$ metallic glass [36].

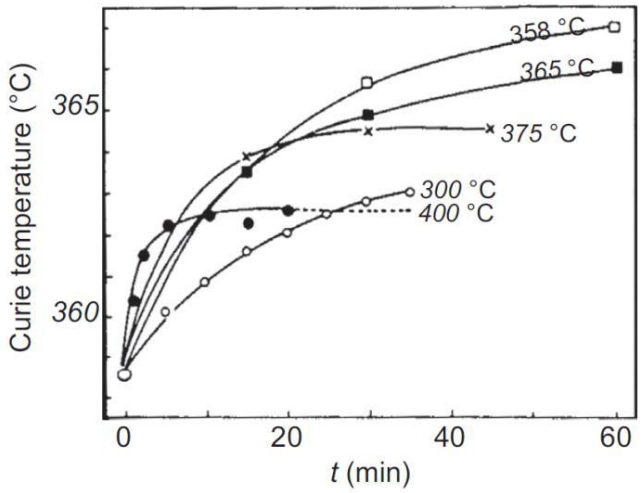

Figure 1.3.4.2: The Curie temperature of Fe80B20 metallic glass as a function of the annealing temperature for selected temperature.

Intersections between different curves suggests that there is not a one-to-one relationship between a property value and the internal state of the glass, in the sense that the same property value can be generated by two different internal states.

1.4 Mechanical Properties

1.4.1 Comparison with other engineering materials

The availability of BMGs has greatly facilitated the study of mechanical properties and makes it possible to compare metallic glasses with conventional engineering materials. For the present comparison materials-selection maps are used [38,39]. Figure 1.4.1.1 is a map presenting elastic limit and Young's modulus. As can be observed MGs, shaded ellipses, approach ideal strength of $\sigma_y = \frac{E}{20}$, more closely than any other bulk metallic material. Furthermore, considering the index $\frac{\sigma_y^2}{E}$, called *resilience*, which is a measure of reversible elastic energy storage capacity, MGs show exceptionally high values. Indeed they possess the absolute lowest *loss coefficient η* among all materials.

Metallic glasses generally have a larger elastic limit in compression, 2% in general, than polycrystalline metals, for which a typical value is 0.2%. This and the previous characteristics make them good for applications that need to store elastic energy.

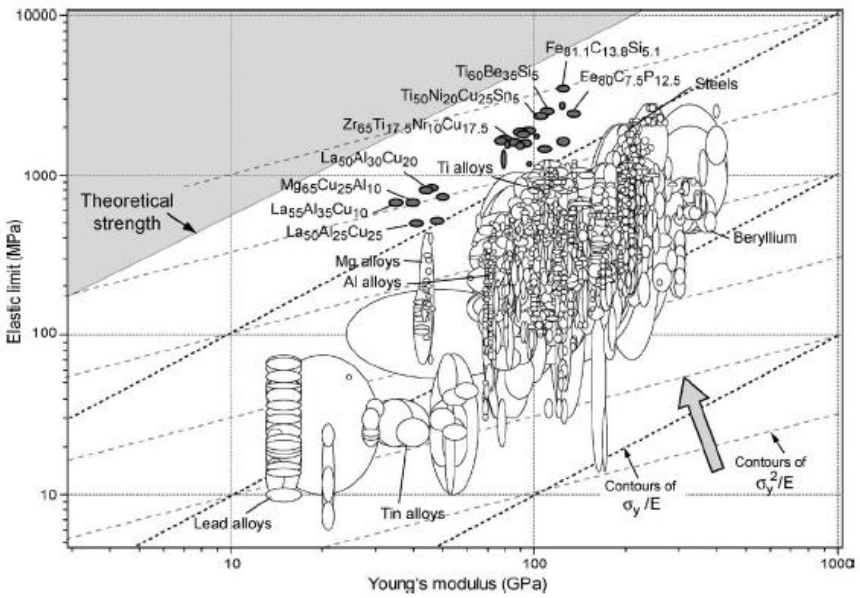

Figure 1.4.1.1: Materials-selection map showing yield stress and Young's modulus for selection of MGs, metals and metal-matrix composites.

A critical aspect is the metallic glasses' degree of brittleness, in particular since other types of glasses, oxide glasses, are characteristically brittle. Considering either the *fracture toughness,* K_c or the *toughness* G_c , $G_c = \frac{K_c^2}{E}$, metallic materials can be defined tough while

ceramic and glassy materials are usually brittle. Remarkably metallic glasses do not belong to a particular group; their K_c and G_c vary over some four magnitude orders, from values similar to the toughest metals to values typical of ceramic, Figure 1.4.1.2.

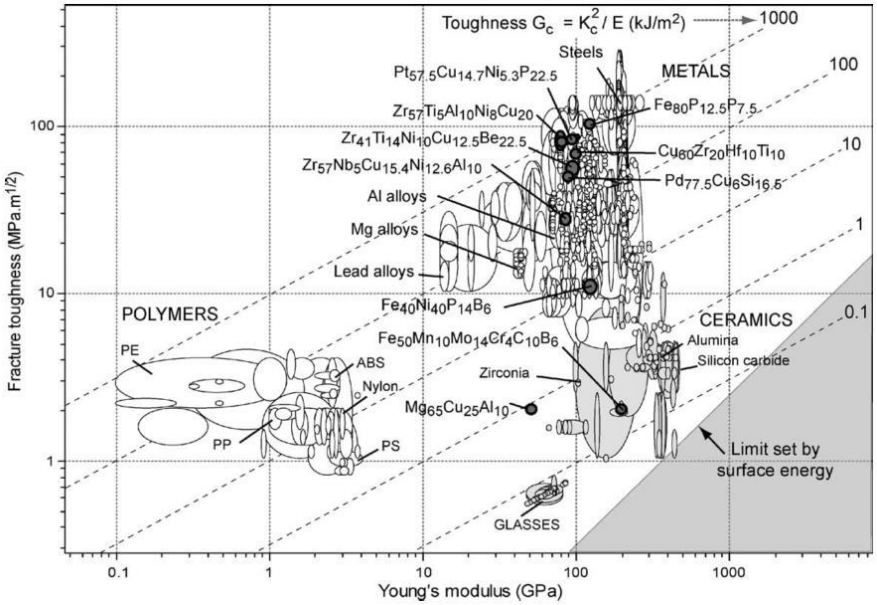

Figure 1.4.1.2: Fracture toughness and Young's modulus for MGS, compared with key conventional materials classes.

Hence, metallic glasses have some drawbacks, and that is mainly because of their plastic flow mechanism.

1.4.2 MGs Deformation Mechanism, STZs and shear bands

In polycrystalline metals plasticity is a consequence of dislocation glide (slip and twinning), and usually results in work-hardening of the material [40]. In metallic glasses defects comparable to dislocation do not exist, due to the lack of long range crystalline order. Instead, a "flow defect theory" [41] inherited from fluidity of liquids has been formulated for glasses, where the defects are described as free volume or as shear transformation zones (STZs). Free volume, as already said, is the excess of volume inside the structure compared with the ideal case, crystalline state. For metallic glasses, free volume enhances the diffusivity [35] (or decreases the viscosity), figure 1.3.4.1 and have an important role in defining the boundary between low temperature and high temperature plastic flow, as will be explained later.

As suggested by Argon [43], the plastic deformation of metallic glasses below their glass transition temperature is based on local cooperative rearrangements of atoms. These spheroidal areas in which this rearrangement occurs are called shear transformation zones (STZ).

STZ is a cluster of atoms with more associated volume than the surrounding matrix, playing the role of weak points [42]. In contrast with dislocations, that are line and mobile defects, shear transformation zones only appear in response to external stimuli, thus are definable *a priori* in the static glass structure before deformation [44]. Also they operate as immobile entities that do not migrate.

STZs, when an external stress is applied, have the tendency to modify their structure; in particular is that when a critical shear stress is reached STZs flip, i.e. atoms rearrangement occurs, and this consists of an inelastic/plastic event. Generally associated with STZs activation (flipping) is a change in the local stress-strain field which induces an increase of structural disorder, due to directional rearrangement in STZs [44]. The surrounding matrix is thus distorted and new flow defects, STZs, may be generated, Figure 1.4.2.1. Hence, STZs activation is accompanied by increase in free-volume locally. When more STZs link up along a certain plane they realize a softening mechanism, in which strain is localized, called shear bands.

It is also possible, but rare, that, consequent to applied cycles of small stress (elastic regime), the STZs excess volume could condense and resistance to further deformation may increase [42].

Shear bands are characteristic deformation features of metallic glasses and strain localization in shear bands is the main cause that retained them to find wider structural application.

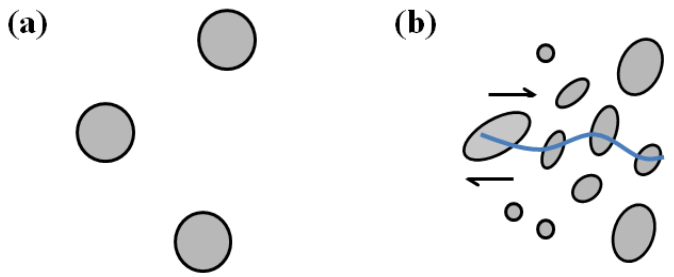

Figure 1.4.2.1: The grey circles indicate the STZs, including an indication of relative size. Figure (a) shows some STZs without stress, while figure (b) under shear stress (black arrows). Applying a shear stress on an STZ, the atomic configurations changes and new STZs forms. The percolation of the STZs forms a shear band (blue line).

Spaepen [46] realized a deformation-mechanism map, showing the transition from homogeneous to localized flow as function of the strain rate and the temperature for metallic glasses. At low stresses the glasses show homogeneous viscous flow. Below the glass-transition temperature, the flow is very slow and can be regarded as creep, whereas at T_g and above, the flow can be rapid, becoming attractive for shaping metallic glasses. At high stresses, in a significant temperature range including room temperature, the plastic flow of the metallic glasses is inhomogeneous and sharply localized into thin shear bands.

Inhomogeneous flow deformation type is characterized by the formation of shear bands, their rapid propagation, and the sudden fracture of the sample. This behaviour, generally associated with small or zero plastic strain, has at its origin in the shear-softening occurring when shear bands appear [44]. As a localized zone is deformed it becomes softer and therefore more susceptible to further deformation. Softening, that causes shear strain localization, is due to a decrease in viscosity at shear bands retained to be caused by induced structural disorder, free-volume, and/or local temperature rise[44].

Shear bands form close to maximum shear stress plane and their shear offsets are sharp. Shear bands are considered 10-20nm thin [CITAZIONE]. In tension , the shear softening usually leads to catastrophic failure on a single dominant shear bands. The sample shows zero ductility, even though there is extensive local plastic flow. Sample fracture surfaces are characterized by a *vein pattern* and significant local heating is registered. In compression, instead, there is clear evidence that shear bands can operate cold, with no significant local heating. Thus, in this condition, more than one shear bands form and propagate, also their offsets are small. A sudden drop in load, in the stress-strain plot, is registered when shear

bands propagate. This deformation regime is characterized by *serrated* or *stick-slip* flow [47], Figure 1.4.2.2. However machine stiffness and sample size play an important role for this regime to happen.

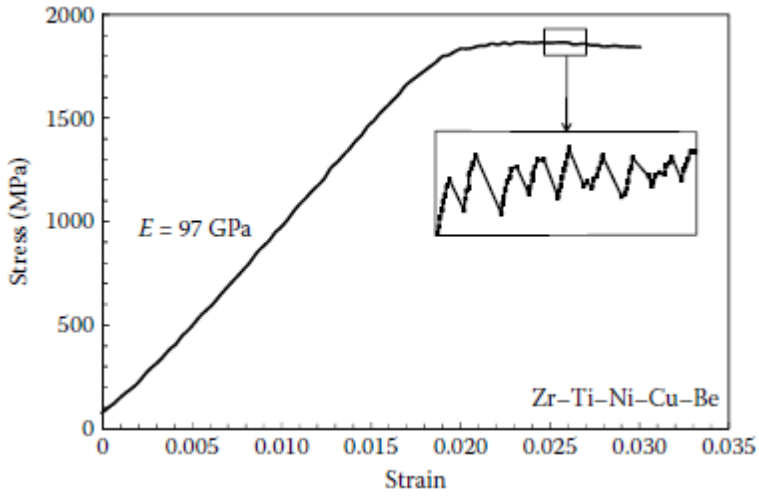

Figure 1.4.2.2: compressive stress–strain curve for the $Zr_{40}Ti_{14}Ni_{10}Cu_{12}Be_{24}$ BMG alloy is shown, tested at a strain rate of $10^{-4}s^{-1}$ [48].

1.4.3 MGs Toughness

So far it is clear that plastic flow in metallic glasses happen in almost all conditions, however in most cases it is highly localized and leads to brittle-like behaviour. It is important to understand what parameters influence MGs toughness.

Pugh, pioneer in these studies [49], noted that for polycrystalline metals plastic resistance is proportional to the shear modulus, μ, and that the resistance to dilatation and cracking is proportional to the bulk modulus, B. Then, a low value of μ/B should favour plastic flow over cracking. In terms of Poisson's ratio with the decreasing of the ratio μ/B , ν tends to his upper limit 0.5 (characteristic of a liquid). Several authors noted that high Poisson's ratio metallic glasses [50,3], for example Pt-based, show exceptionally high plastic strain in compression and high fracture toughness. In figure 1.4.3.1 is presented trend of fracture toughness versus Poisson's ratio of some metallic glasses. It can be noted that MGs show significant toughness only when ν is higher than 0.31-0.32.

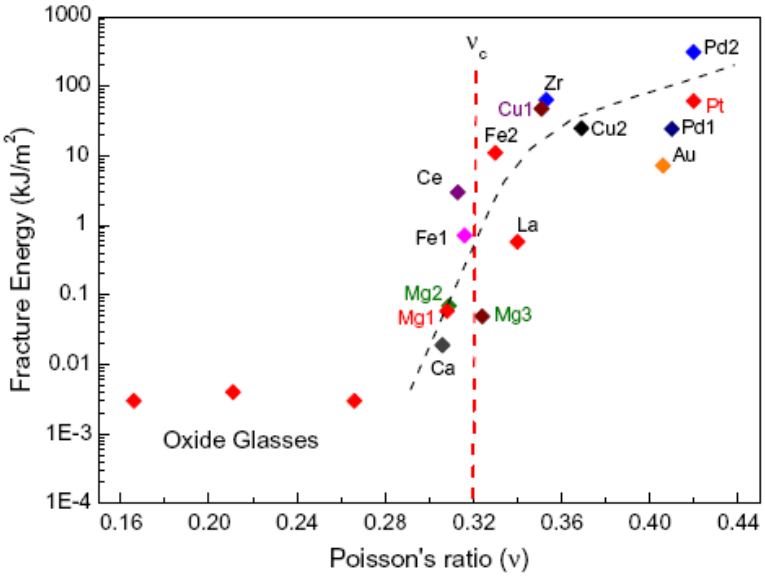

Figure 1.4.3.1: The correlation of fracture energy with Poisson's ratio, *v*, for metallic glasses [50]. The toughness appears to be sharply reduced below a critical Poisson's ratio, *v*, of 0.32.

The field of developing new metallic glass compositions with larger Poisson's ratio *v* is very active, as well as the one that studies the nature of the correlation between Poisson's ratio and improved plasticity.

It is interesting to note that STZs volume, size, is strongly correlated to ductile properties. Figure 1.4.3.2 shows that metallic glasses with larger plastic deformation, larger Poisson's ratio, under uniaxial compression present larger STZs size [45]. Another interesting fact, recently discovered, is that STZs are more likely to be found in local regions characterized with more structural disorder, such as more free-volume or higher atomic level stresses [44].

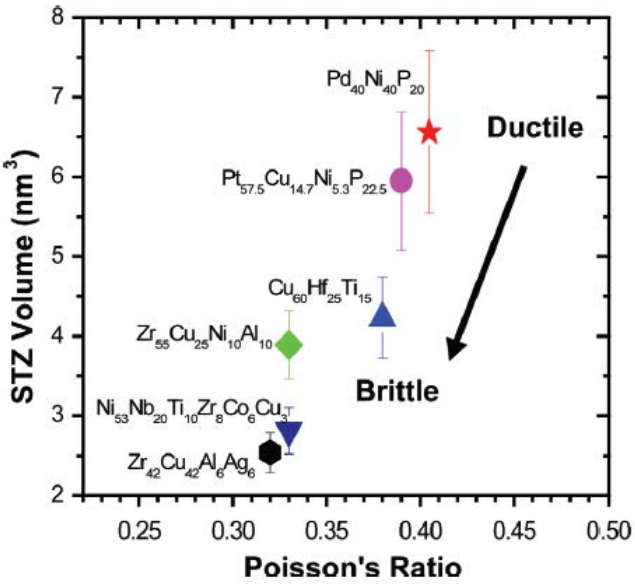

Figure 1.4.3.2: correlation between STZ size, Poisson's ratio and plasticity of various MGs.

Improved ductile properties are also correlated with particular shear bands feature. In high-plasticity metallic glasses is present a finer spacing between shear bands, and consequently each shear offset is small. Thus, a delocalization of shear strain occurs and for that plasticity results enhanced. Not surprisingly is present a shear bands spacing dependence on Poisson's ratio. Furthermore, Poisson's ratio has been correlated also to likelihood of shear-transformation.

1.4.4 Inhomogeneity, plasticity and rejuvenation

J. G. Wang et al. [33], similarly to Wagner et al. , spotted hardness distribution of bimodal nature using a nanoindenter on a Zr-Cu-Al-Ni metallic glass which shows an exceptional large compressive plasticity. In fact in their work J. G. Wang et al. [33] correlated the large plasticity to the presence of two different phases, a strongly bonded region and a weakly bonded region. The coexistence of soft/ductile and hard/brittle phases has been noticed in crystalline alloys and optimum mechanical properties of strength and ductility are achieved when the hard phases is homogeneously distributed in a soft matrix. Exactly these structure has been observed with HRTEM technique, figure 1.4.4.1 [33]

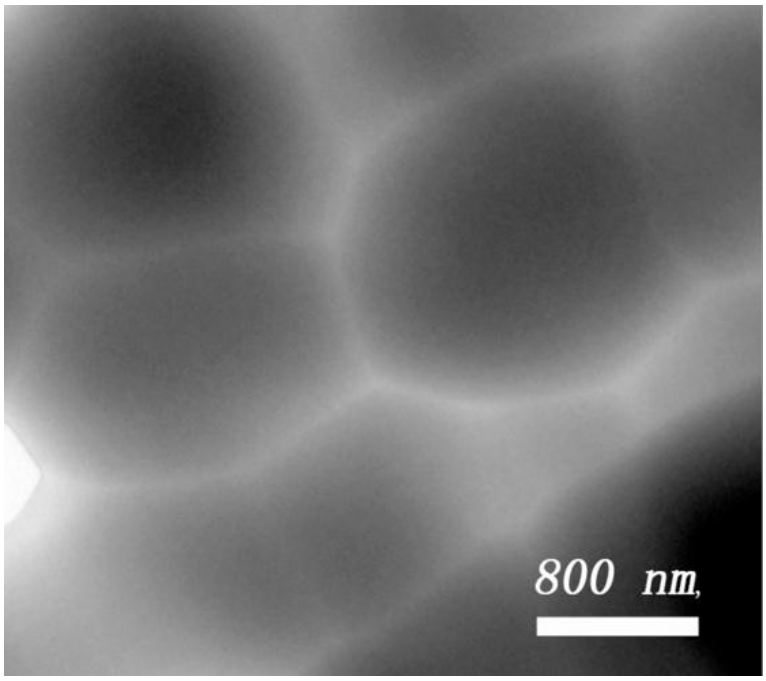

Figure 1.4.4.1: The microstructure of the as-cast ZrCuNiAl in TEM.

Microstructure inhomogeneity are probably inherited from the liquid phase; indeed Ichitsubo et al. [32], analysing other compositions, put in correlation fragility value *m* , as well as Poisson ratio with the degree of inhomogeneity (intended as the fraction of weakly bonded region) and claimed that they are directly proportional: better ductility properties are shown higher is the inhomogeneity, i.e. higher is the fraction of soft phase. It has been claimed that weakly bonded regions may play an important role in governing plasticity/ductility processes; it has indeed more free-volume and so shear transformation zones occur preferentially in this region, as critical shear stress is lower, [33], hence numerous shear bands can initiate, in different sites, and accommodate the strain preventing catastrophic fracture induced by few primary shear bands. Through this process energy dissipation is improved.

It appears clear that ductile properties can be enhanced by stimulating shear bands initiation and hinder shear bands propagation; hence a finer the patter of shear bands is realized, and plastic flow is more uniformly distributed across the entire sample, as the onset of catastrophically localized shear is delayed. In this picture free-volume and inhomogeneity play a crucial role: in a more open structure STZs are more favourable to be found, thus shear bands are easier to nucleate. Inhomogeneity, such as the denser phase described above, implement a blocking mechanism for shear bands propagation. A proven and effective way to enhance plasticity is by plastic deformation, cold-working mostly.

Rejuvenation is referred as exactly the process just described: a mechanism by which is possible to introduce free-volume, disorder and inhomogeneity in the metallic glass structure. Rejuvenation has therefore the opposite effect that annealing has on the structure. The main aim is to improve ductile properties, as the material should be able to sustain more plastic strain and more homogeneously since plastic flow occur with generation of multiple shear bands.

2. EXPERIMENTAL TECHNIQUES

In the following chapter is provides description of the techniques that have been used during the experimental research at the department of Material Science and Metallurgy of Cambridge University.

2.1 Materials and sample preparation

In the present work three metallic glass different compositions were considered and tested. Thermal cycles between room temperature and different cryogenic temperatures have been applied to considered metallic glasses, this method is explained later in Chapter 3. The aim of this treatment is metallic glass structure rejuvenation. To test material's structural changes both thermal and mechanical tests have been employed, later discussed in this chapter.

Metallic glass compositions used are: $La_{55}Al_{25}Ni_{20}$, $La_{55}Al_{35}Ni_{10}$ and $Cu_{46}Zr_{46}Al_7Gd_1$. The first composition is under the form of ribbons, while the other two are in bulk form, cylindrical bar.

In the following table, Table 2.1.1, principal materials' physical properties are presented:

	T_g	E	ν	$\sigma_{y,\,c}$
$La_{55}Al_{25}Ni_{20}$	220 °C	35-40 GPa	0.34	800 MPa
$La_{55}Al_{35}Ni_{10}$	220 °C	35-40 GPa	0.34	800 MPa
$Cu_{46}Zr_{46}Al_7Gd_1$	430 °C	90 GPa	0.38	1600 MPa

Table 2.1.1: principal mechanical and thermal properties, glass transition temperature, T_g, Young's modulus, E, Poisson's ratio ν, and compression yield pressure, $\sigma_{y,\,c}$, for the compositions used [53, 54].

Thermal cycling has been applied using a manually built device for holding the samples in a cryogenic liquid filled dewar. The apparatus used is presented in the following figure, Figure 2.1.1.

A small heater was used as dryer to bring the samples at room temperature more rapidly.

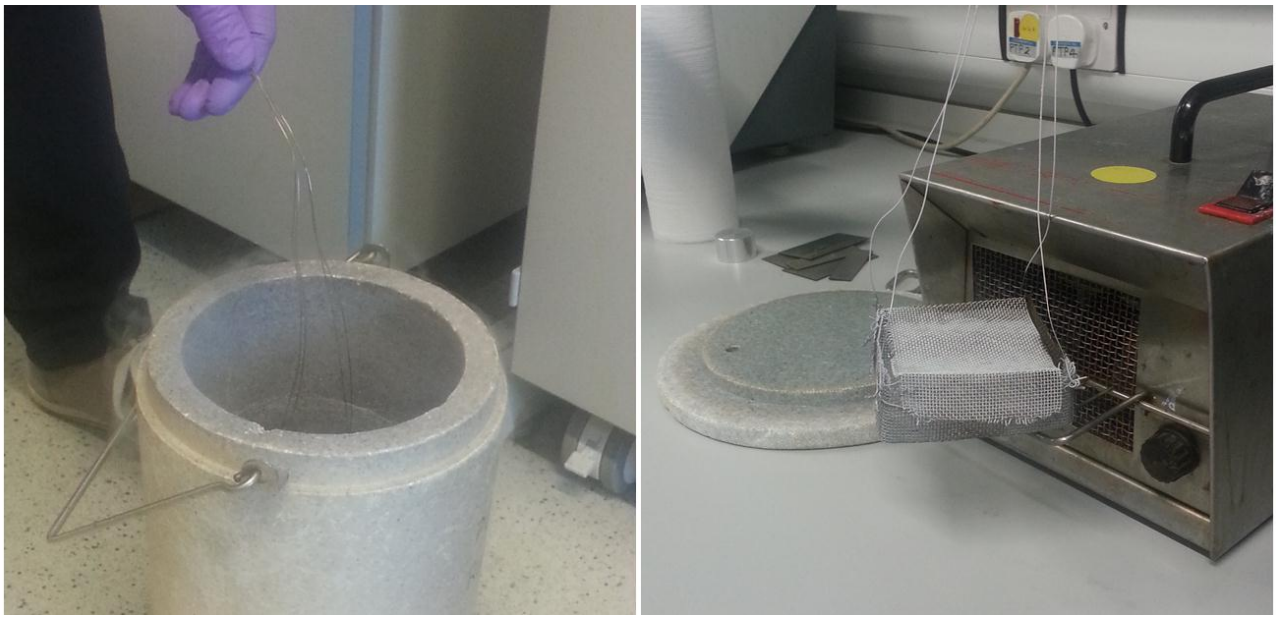

Figure 2.1.1: dewar fill with liquid nitrogen is shown in the left picture; in the right picture the device, a box made of steel wires, used to immerge samples in liquid nitrogen.

2.2 MIcroindentation

A micro-indentation test quantifies the resistance of a material to plastic deformation. A prescribed load is applied on the material's surface through a millimetre-scale diamond indenter. After removal of the load, the indented area is measured and used to calculate hardness. The hardness number is defined as applied force divided by the indent's surface area, expressed as kgf/mm^2 for microindentation. This hardness value is affected by many factors, including the indent's shape, the loading rate, the surface finish and the size of the indentation.

In this work, Vickers tests are conducted with a Mitutoyo MVK-H2 Hardness testing machine . In all Vickers tests, the load is applied without impact and held in place for 15 seconds. The indenter is a pyramid. After load removal, the two diagonals of the diamond-shape indent are measured optically and then the average value, d, is used to compute the area. The Vickers hardness (HV) is calculated by the following equation [51].

$$H_{\mathrm{V}} = 1854.4 \times L/d^2$$

where H_v is the Vickers hardness (kgf/mm^2), L the applied load (in units of grams force) and d is the average diameter (μm). This formula takes into account the effect of the angle of 136° between the opposite faces of the pyramid indenter.

2.3 Nanoindentation

The development of high level nanoindentation instruments has occurred with the discovery of many new families of bulk metallic glasses during the last decades. For this reason nanoindentation has long been used to assess the mechanical properties of metallic glasses and nowadays it represents one of the most common techniques used to investigate this class of materials.

Instrumented indentation testing can reveal a wealth of detailed information about the mechanisms of elastic and plastic deformation in metallic glasses, generally extracting the elastic modulus and hardness of the tested material from the load-displacement curve.. In nanoindentation small loads and tip sizes are used, consequently being the indentation area of the order of several square micrometers, it is impossible to obtain a direct measure by optical techniques.

Differently from microindentation testing, in nanoindentation load and penetration depth are recorded during the loading and the unloading process, and they are generally represented in a load displacement-curve (Figure 2.3.1).

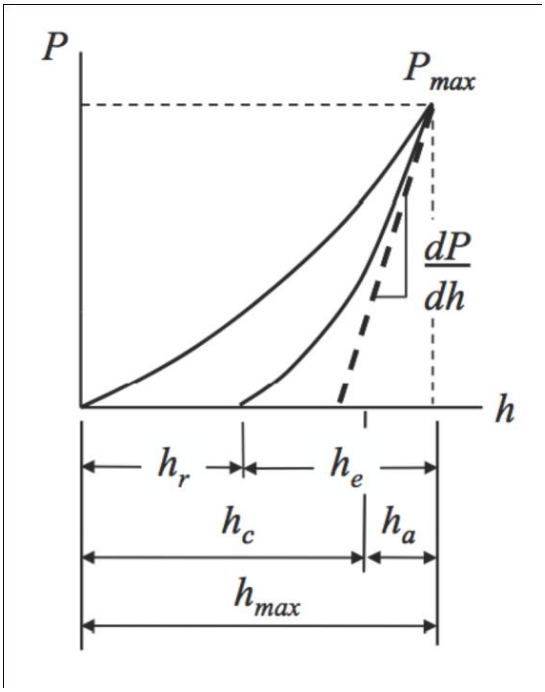

Figure 2.3.1: Load-displacement curve obtained from a nanoindentation experiment with maximum load P_{max} and depth beneath the specimen free surface h_{max}. The depth of the contact circle h_c and slope of the elastic unloading dP/dh allow to calculate the elastic modulus and hardness of the samples. h_r is the depth of the residual impression, and h_e is the displacement associated with the elastic recovery during unloading.

For all the nanoindentation results presented in this thesis it was used a spherical tip measuring 8.074 µm of diameter, made by diamond and with a Poisson's ratio, *v*, of 0.07 and an elastic modulus, *E*, of 1141GPa.

From the penetration depth, h_{max}, the geometry and the dimension of the indenter tip (that are known), it is possible to obtain an indirect measure of the contact area, *A*, at maximum load, P_{max}.

The mean pressure, pm, and hence the hardness, *H*, are defined by the following expression:

$$P_m = H = \frac{F}{A} = \frac{F}{\pi a^2}$$

The contact area, *A*, at P_{max}, can be expressed as a function of the contact depth h_c : $A=F(h_c)$ where the functional form of *F* must be established experimentally in a prior analysis. In this work it is used the fitting function presented below:

$$A = F(h_c) = a_0 \cdot h_c^2 + a_1 \cdot h_c + a_2 \cdot h_c^{\frac{1}{2}} + a_3 \cdot h_c^{\frac{1}{3}} + a_n \cdot h_c^{1/n}$$

where $a_0,\ldots a_n$ are the area coefficients associated with a particular tip.

With the Oliver and Pharr method [52] it is possible to estimate the value of h_c through the expression: $h_c = h_{max} - \varepsilon P_{max} S$

where S is the stiffness and ε is the geometric constant depending on the tip (for a spherical one ε is 0.75).

The stiffness is defined by the slope of the unloading curve: $S = dP/dh$.

The indentation modulus is usually established according to the slope of the maximum unloading curve. The following equation shows that the indentation reduced modulus, E_r, is a function of the stiffness, dP/dh, and the contact area at the maximum load:

$$E_r = \frac{1}{2}\frac{\sqrt{\pi}}{\sqrt{A}}\frac{dP}{dh}$$

The reduced modulus, E_r, is related to the elastic modulus, E, and the Poisson's ratio, ν, of the glass and the indenter through the following equation:

$$\frac{1}{E_r} = \frac{1+\upsilon_i^2}{E_i} + \frac{1+\upsilon_g^2}{E_g}$$

where the letters i and g indicate respectively the indenter and glass.

The shape of the load-displacement curve is a rich font of additional information, not only providing the modulus and hardness of the sample, but also for the identification of non-linear events such as phase transformations, cracking and shear bands.

For metallic glasses the elastic-plastic transition can be easily observed in the load-displacement curve as a pop-in event. A pop-in is characterized by sharp depth drop at constant load with the tip that clearly goes deeper in the material.

This transition in metallic glasses is associated with the formation and propagation of a single shear band.

Figure 2.3.2 shows a typical example of a load-displacement curve for a metallic glass where it is possible to identify visibly the first pop-in event by the evident discontinuity. Moreover the pop-in is evidenced also by a sharp increase in the indentation velocity, with the material that rapidly yields.

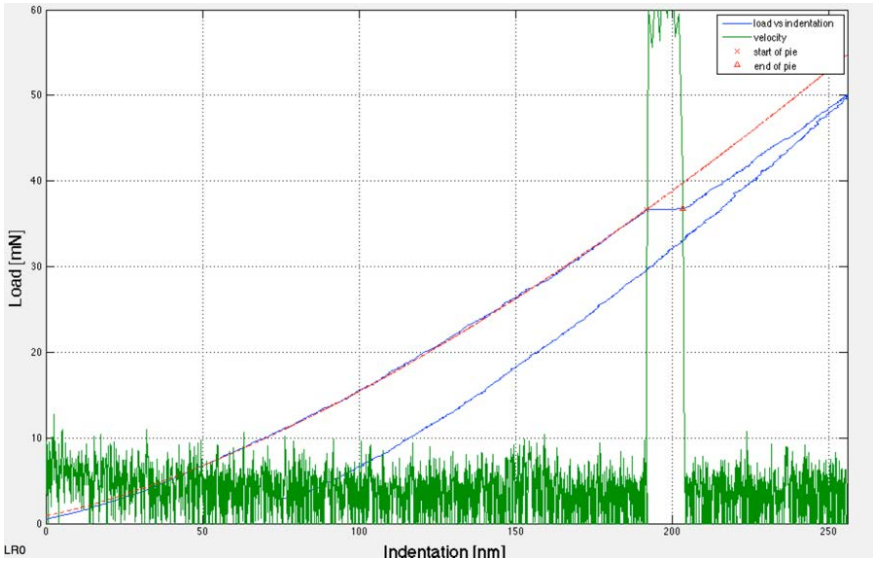

Figure 2.3.2: Typical nanoindentation load displacement curve for a metallic glass.

The pop-in event is clearly visible as a discontinuous horizontal segment in the load-displacement curve (blue). This event is also marked by the sharp increase in velocity of the indenter tip (green) and a departure from the Hertzian elastic solution (red)

From the picture it is possible to detect that a pop-in is valuable in terms of the first important departure of the load-displacement curve from the elastic Hertzian solution defined by the expression: $P = \frac{4}{3} E_r R^{\frac{1}{2}} h^{\frac{3}{2}}$

where *P* is the applied load, *R* is the tip radius, h is the indentation displacement, and E_r is the reduced elastic modulus. The first yield pressure at the first clear pop-in is an important parameter that can be used to characterize a material by nanoindentation.

While the first yield load, F_y , is immediately visible on the load-displacement curve y-axis, the yield pressure, p_y, must be calculated by the analytical expression: $p_y = F_y/A$.

and the contact area at the yielding point, can be approximated as: $A = \pi(2R_i h_c - h_c^2) \approx 2\pi R_i h_c$

where the approximation is appropriated when the indentation depth is much smaller than the radius of the indenter.

In the elastic regime it is possible to operate a further simplification of the area: $A \approx 2\pi R_i h_c = \pi R_i h_y$ because in elastic conditions the contact depth, h_c, is equal to half the total displacement at the yielding point, called h_y. The result expression of the yield pressure is the following one:

$p_y = F_y / \pi R_i h_y.$

Another interesting parameter to evaluate is the material reduced elastic modulus that can be calculated using the Hertzian solution with h_y and $F = \frac{4}{3} E_r R^{\frac{1}{2}} h^{\frac{3}{2}}$.
and can be compared with the reduced modulus calculated from the unloading curve.
All the indentation data presented here have been obtained using a MTS Nanoindenter XP.

2.4 Uniaxial compression test

The compressive strength of a material is the capacity of its structure to tolerate load tending to reduce its size. It can be measured plotting applied force against deformation in a compression test. The ultimate compressive strength of a material is that value of uniaxial compressive stress reached when the material fails completely.
Measurements of compressive strength are usually made on a universal testing machine and are affected by the specific test method and conditions. It is particular important to consider these parameters to extract materials true mechanical properties.
For example, a softer machine stores larger elastic energy and releases it at the onset of yielding. As bulk metallic glasses are work-softened, such big amount of energy release could give a catastrophic failure. Only if the machine is much stiffer than the sample can the operation of shear bands be controlled.
In Figure 2.4.1 [COLD VS HOT] the sample and machine are schematically represented as two springs subject to the same load, *P*. In the picture k_m, x_m, k_s, x_s are respectively the stiffness of the machine, the deformation of the machine, the stiffness of the sample and the deformation of the sample.

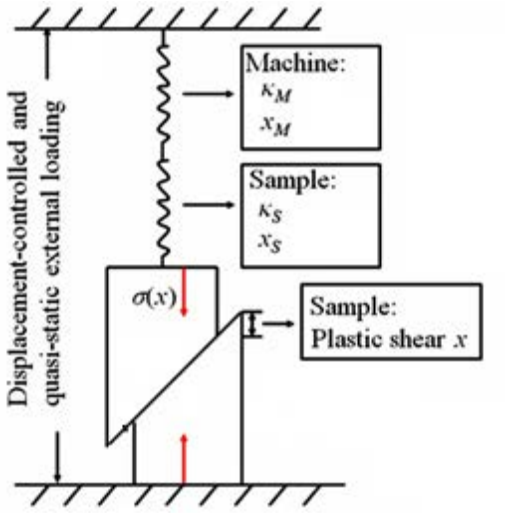

Figure2.4.1 A scheme of the machine-sample system [COLD VS HOT]

In order to get the actual compressive fracture strain of the sample it is essential to subtract the deformation of the machine system from the results of the compression test, which include both deformations of the sample and the machine.

The pure response of the machine to the deformation was measured by deforming the machine and the anvils without the sample, in order to determine their compression curve and stiffness, *km*. Subsequently, the sample has been tested in compression and the elastic deformation of the machine has been subtracted point by point to the obtained curve (machine + sample), as expressed by the equation: $x_s = x_{tot} - x_m = x_{tot} - k_m \cdot P$

The result of this procedure is the load-displacement curve of the sample only, from which it is possible to obtain, through the dimensions of the sample, the stress –strain curve.

Then it is possible to evaluate the strain at the fracture point that is the compressive fracture strain, ε_f.

The compression test was performed using silicon nitride anvils and a bench-top tester Tinius Olsen H25-S UTM, electrical dual column system, with a maximum capacity of 25 kN (5000lbf).

2.5 Differential Scanning Calorimetry

Differential scanning calorimetry (DSC) is a very sensitive technique that measures a material's thermal properties. In a DSC the difference in heat flow to the sample and a reference at the same temperature, is recorded as a function of temperature. The sample is sealed in an aluminum pan. The reference is an inert material such as alumina, or just an empty aluminum pan. The temperature of both the sample and reference are increased at a constant rate. A DSC setup of this type is presented in Figure 2.5.1

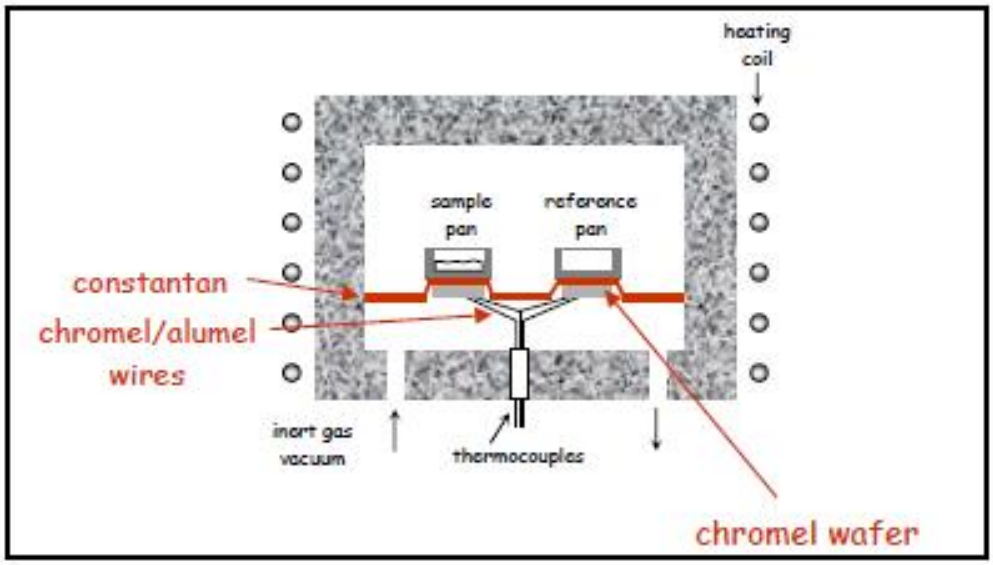

Figure 2.5.1: representative scheme of a heat-flux DSC setup

Since the DSC is at constant pressure, heat flow is equivalent to enthalpy changes: $dq/dt = dH/dt$. Here dH/dt is the heat flow measured in mW or equivalently mJ s-1.

The heat flow difference between the sample and the reference is what the machine measures:

$$\Delta(dH/dt) = (dH/dt)_{sample} - (dH/dt)_{reference}$$

This difference can be either positive or negative. In this experience DSC tests aim is to measure glass relaxation and glass transition, therefore Tg and the relaxation spectrum before Tg. The relaxation phenomenon brings the glass in a lower enthalpy, free-energy state. Therefore the sample releases heat in this process and an exothermic "peak" is realized. It has to be said that thermal properties measured with DSC technique are mass and heating rate dependent, indeed the material tested is in a glassy state.

In the present work TA Instruments Q2000 DSC machine has been used. Glass transition temperature, T_g, and relaxation spectrum have been measured and compared for different samples.

2.6 Optical microscope

The optical microscope is a type of optical instrument that employs visible light and a system of lenses to magnify images of small samples.

During the experimental activity optical microscopes have been used in order to evaluate the quality of polished surfaces and shear band features. The resolution can reach 1µm under 1000x magnification. Optical microscope used in this experience is the Olympus BHM.

2.7 Scanning electron microscope

A scanning electron microscope (SEM) is a particular kind of microscope solving the problem of wave length limit associated with traditional optical systems.

An SEM uses a focused electron beam, with much shorter wavelength than visible light, over a surface to create an image of the sample and allowing better resolutions.

The electrons in the beam interact with the sample, producing various signals that can be used to obtain information about the surface topography.

SEM pictures presented in this thesis have been obtained by utilizing a scanning electron microscope Philips XL30 SEM SFEG (Figure 2.7.1).

Figure 2.7.1 The SEM Philips XL30 SEM SFEG

The technique consists in focusing an X-ray beam into the sample. The incident beam can excite an electron in an inner shell, ejecting the particle from it. When an electron hole is created in the electron's former position, a second electron from an outer, higher-energy shell fills the hole and the difference in energy between the higher-energy shell and the lower energy shell is released in the form of X-ray. The number and energy of the X-rays emitted from a sample are measured by an energy-dispersive spectrometer and are characteristic of the atomic structure of the element they were emitted from. This permits chemical characterization of the sample surface within a depth of about 1 μm.

2.8 Atomic force microscope

An atomic force microscope (AFM) provides quantitative information about the variations in height across a surface. It is a very high resolution type of a scanning probe microscope and is not based on a focused beam as SEM and optical microscopes.

An AFM uses a miniscule, very sharp needle called tip to investigate the sample surface. The tip is mounted at the end of a small cantilever, which deflects as the force on the tip changes.

The simplest way to operate with an AFM is to scan the tip over the surface and to monitor the deflection of the cantilever as the tip is deformed by surface features. The cantilever

deflection is measured by reflecting a laser beam off the back of the cantilever, and monitoring the laser beam's motion on a detector.

The 1nm resolution of AFM is achieved by atomic force detection between the tip and the sample.

The structure of an atomic force microscope is presented in Figure 2.8.1

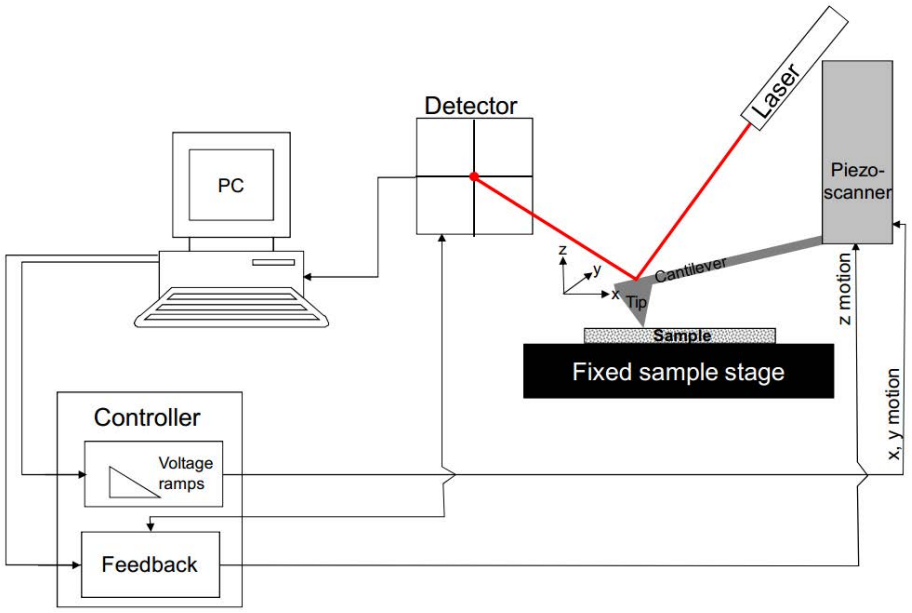

Figure 2.8.1 : Schematic representation of an atomic force microscope. It is possible to see the tip at the end of the cantilever. The relative motion is performed with a sub-Angstrom accuracy by a piezoelectric actuator. The beam is reflected towards a photodetector which monitors and amplifies the cantilever deflection. The system is connected with a pc through a controller that receives a feedback from the detector and moves the scanner.

In the research presented here a Veeco Dimension 3100 AFM atomic force microscope was used to evaluate sample surface, Vickers imprints pile up in particular.

3. RESULTS AND DISCUSSIONS

Structural modifications in metallic glasses after cryogenic treatment have not been studied thoroughly: only a few literatures are relevant. Chen, et al. [55] claimed that nanocrystals were nucleated of a Cu-based bulk MG after leaving the sample in liquid nitrogen for hours or days.

In Chapter 1 it has been explained that metallic glasses, for some composition at least, can show a certain structural inhomogeneity [30,31,32,33,56].
The hypothesis which is the base of this experimental work is considering metallic glasses structure composed of two different phases (for simplicity): one phase is supposed to be the matrix and is characterized by a more open structure, with more free-volume; the other phase is finely dispersed in the first one and is characterized by a denser structure (less free-volume). This hypothesis finds some approval from other works in the literature [30,31,32,33,56].
Being the two phases thermodynamically different, 'soft' one is more rapidly quenched, 'hard' more slowly quenched, they will present also different physical properties, such as Tg, density, elastic modulus, yield strength and coefficient of thermal expansion.

It is also known, Chapter 1, that metallic glasses in numerous cases present mechanical responses characterized by non-affine elastic deformation, for example the detection of plastic deformation under long-time constant loading in the elastic regime [44, 56, 57]. Non-affine elastic deformation, in which elastic strain is not uniformly distributed on each atom, has also been confirmed by simulations work [58].
It is plausible then that imposing an overall temperature change to an inhomogeneous metallic glass mechanical stresses may rise from the fact that the two phases have two different thermal expansion coefficients and that these stresses may likely induce a structural change. This would mean that also 'elastic' thermal deformation is non-affine.

With this aim, then, thermal cycling between room temperature and cryogenic temperature were imposed on various MG samples, in order to spot variations in some physical properties deeply correlated to material structure.

Thermal cycling imposed is presented in the following figure 3.1. The time spent at each temperature is usually 1 minute.

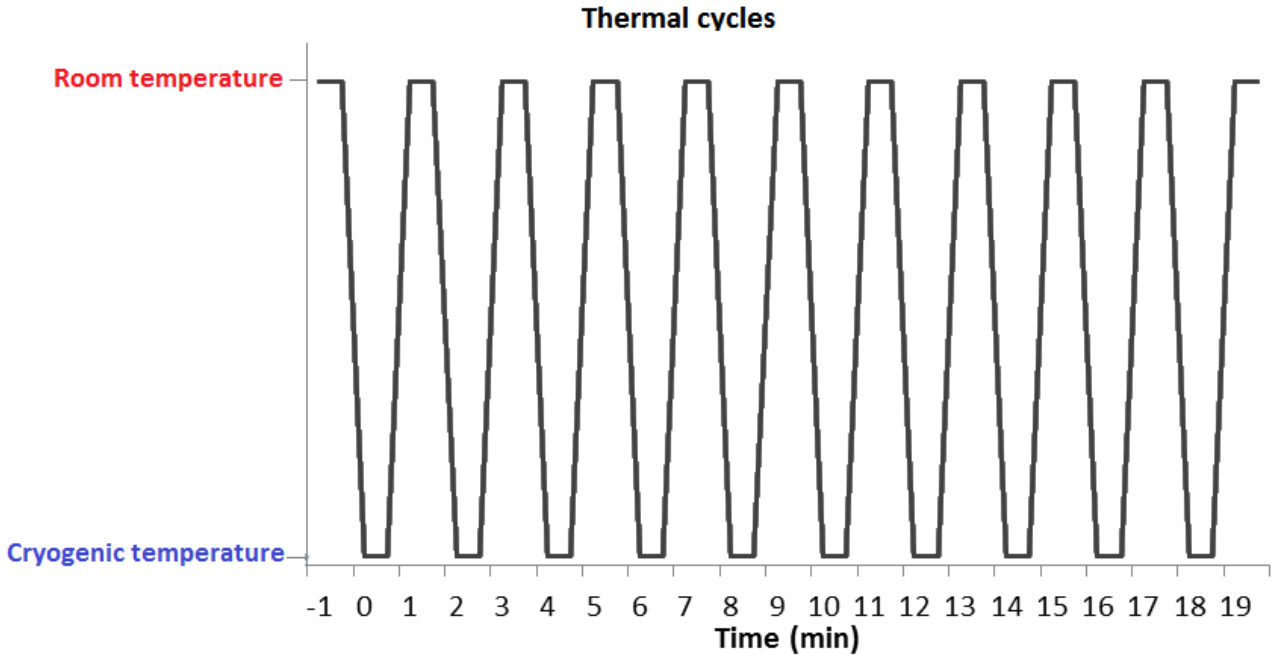

Figure 3.1: Plot representing thermal treatment. A single cycle is composed of 1 minute at cryogenic temperature and 1 minute at room temperature.

3.1 DSC Analysis

The melt-spun $La_{55}Al_{25}Ni_{20}$ metallic glass (MG) ribbons were used in cryogenic-temperature experiment using the device described in the previous section. These samples underwent repeatedly spatially-uniform temperature changes (thermal cycling) from room temperature to cryogenic temperature; three different cryogenic-temperatures were tested: boiling nitrogen temperature (77 K), boiling helium temperature (4 K) and CO_2 sublimation temperature (195 K). (In the case of liquid helium, the ribbon was attached to the holder for resistance-measurement of superconductors.)

This work explored the effect of different cryogenic treatments on several compositions of MGs. In the next section, differential scanning calorimetry (DSC) results are shown, focusing on the thermal changes induced by thermal cycling. The heat of relaxation has been taken

into account, which is released by MG when heating up to temperature around T_g, with a suitable heating rate.

3.1.1 The rejuvenation effect: at first glance

Graph 3.1.1 shows the DSC spectrums of an as-cast and another thermally cycled sample. The compositions are both $La_{55}Ni_{20}Al_{25}$ and thermal treatment is 21 cycles between room temperature and liquid nitrogen temperature. In the graph below, Graph 3.1.1 is showing the relaxation spectrum of the mentioned samples in the temperature range of interest, around 80°C-230°C. The DSC test was conducted using a 10 K/min heating rate, from 25 °C up to 300 °C.

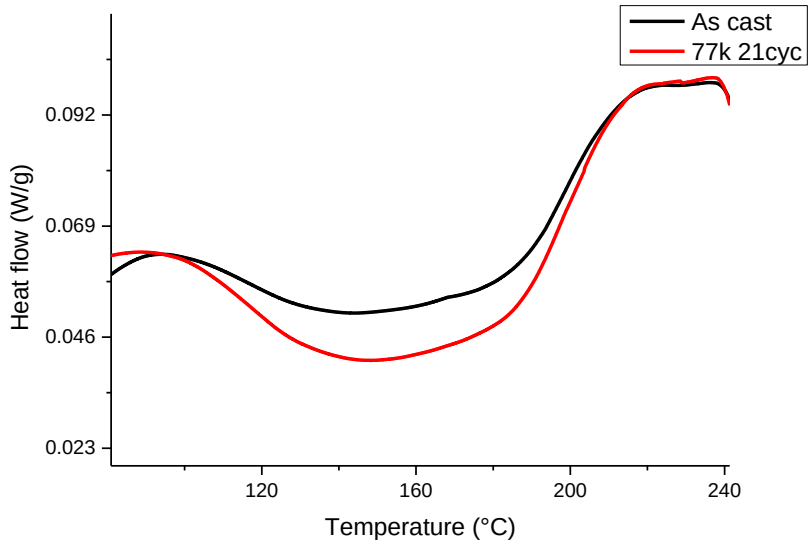

Graph 3.1.1: comparison heat of relaxation spectrum between as-cat sample and 21 RT-liquid N_2 cycles sample. Shaded area is proportional to the heat of relaxation.

The heat of relaxation is proportional to the shaded area in Graph 3.1.1. Relaxation starts when heat-flow is dropping and ends at T_g. The reason to choose T_g is because metallic glass becomes a supercooled liquid above T_g . The unit of heat of relaxation is J/g.

Initial observations suggest that heat of relaxation of the thermal cycled sample is larger respect to the as-cast sample. This increase is a sign of rejuvenation. However, more accurate calculation of the heat of relaxation is needed in order to compare different results.

3.1.2 Heat of relaxation and baseline issues

In most cases determining T_g (or T_f) accurately is difficult: errors, capable of making comparison useless, may arise from approximation. To dispel the uncertainty, the baseline was measured for further experiments. Given the same composition across the tested samples, in the temperature range before the structural relaxation the specific heat flow as well as the specific heat capacity should be the same for different samples; the same idea is valid also after T_g in the supercooled liquid region. A possibility to define a baseline then is to do a linear extrapolation of the data in the temperature range before relaxation, by doing this it should be possible to define also the relaxation onset temperature as well as the other temperature end of the relaxation interval. (For calculation of the relaxation area it is extremely important to define as good as possible the temperature interval, it is by far the most dominant parameter, since the relaxation curve is quite shallow.) A baseline defined in this way has two consistent issues:

1) the definition of the onset is quite problematic due to the fact that the DSC data signal in the temperature region before relaxation is noisy.
2) it is present an overall slope in the DSC signals which is different in different samples, sometimes also in the supercooled liquid region; this is probably due to defects in the DSC measurement machine.

These two issues tend to nullify the possibility to compare different heats of relaxation. The samples in Graph3.1.1, as cast and 21cycles treated ribbons, represent a good example to show these calculation issues.

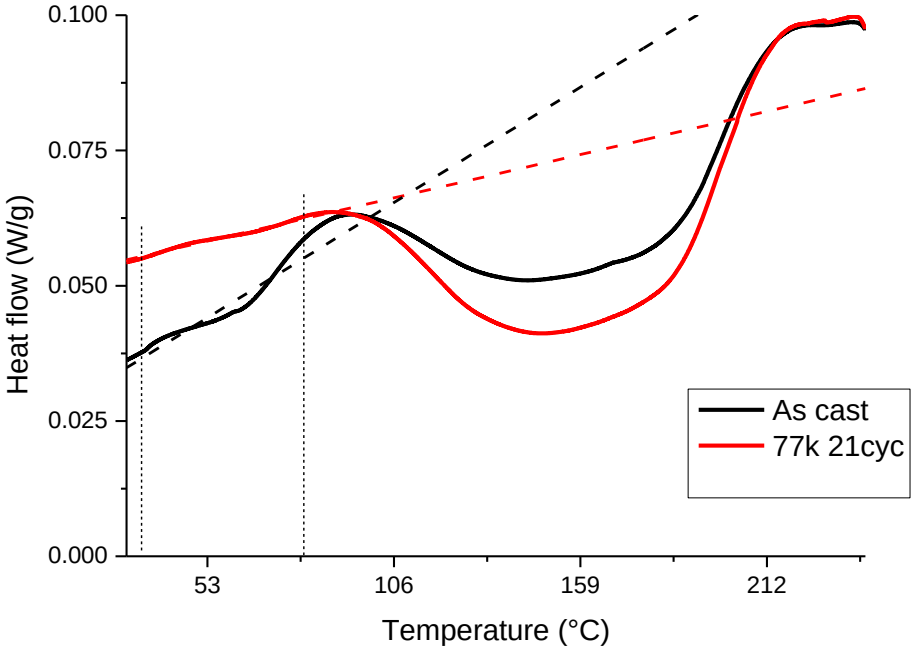

Graph 3.1.2.1: same comparison of Graph 1 is presented; dashed lines are the baselines for both samples extrapolated from their pre-relaxation temperature ranges.

In Graph 3.1.2.1 are reported the DSC data linear interpolations, in the range delimited by the black vertical lines, for the Graph 3.1.1 samples, as cast and 21 cycles treated ribbons. It is evident, considering the black curves that represent the as cast sample, that the slope in the temperature range considered make impossible to define a good baseline. In theory, same composition metallic glass ribbons should have the same behaviour when heated in the temperature range before relaxation, because C_p is the same, therefore using this range as a baseline for the area calculation should be possible. (The same concept is applicable also to the behaviour after T_g in the supercooled liquid region.) Unfortunately the DSC data differential slopes make impossible to use this method to create a useful baseline.

The differential slope issue is very problematic because even if the relaxation onset and offset can still be selected manually it is very difficult to achieve a decent comparability between heat of relaxation calculated with an unstable baseline.

Furthermore, measurement of the heat of relaxation needs some suitable reference, and that is usually a relaxed sample. Therefore it has been decided to take a second DSC spectrum after the first one, so every sample undergoes a measurement consisting in a first heating ramp, a subsequent cooling ramp and then a second heating ramp followed by

another cooling ramp. Every part of the measure must be executed at the same heating rate. Then subtracting the second heating scan from the first scan should give the relaxation spectrum only, also possibly eliminate or reduce the slope effect and the signal noise. This method has been used already before by F.O. Mear et al. [59]. At this point the baseline needed for the area calculation is no more an issue and can be set directly defining the relaxation interval temperatures, onset and offset, and imposing a signal value equal to zero at those temperature. For this work both annealed and crystalline references have been used, mostly annealed though.

All heat of relaxation calculation carried out in this chapter are made using the method described previously.

In the graph below, Graph 3.1.2.2, are reported as examples a first heating and a second heating DSC curves as well as a the DSC spectrum of the relaxation after subtraction, where also a baseline has been defined.

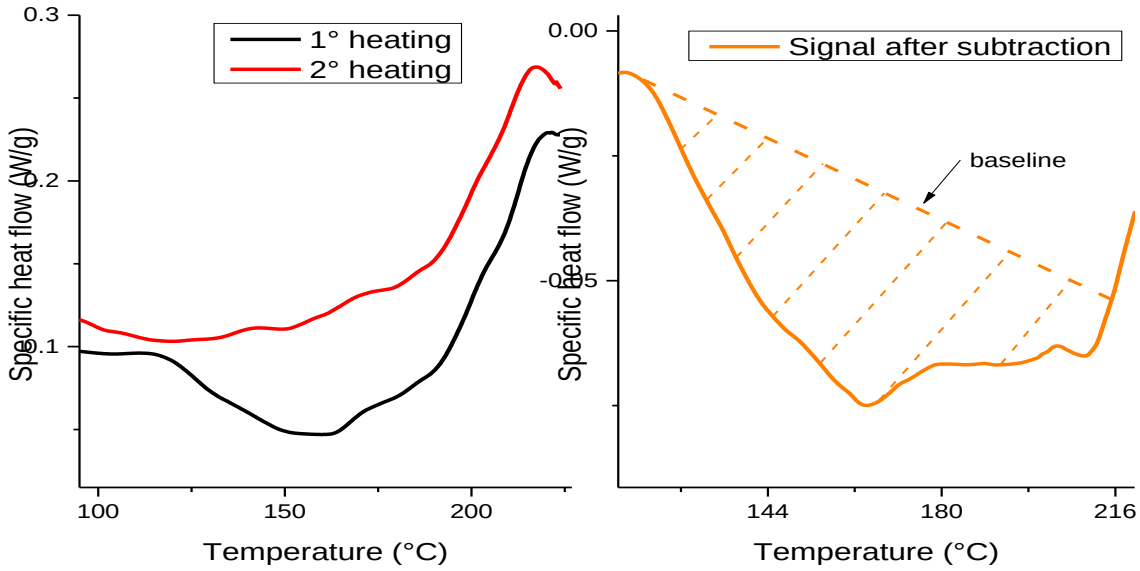

Graph 3.1.2.2: a first and a second heating scan DSC spectrum are shown (left); relaxation spectrum derived from first heating and second heating subtraction is shown (right). A baseline identifies the relaxation area.

Applying the calculation method explained above to the DSC spectrums in Graph 3.1.1 results in these values for the heat of relaxation: for the as cast sample ΔH_{rel}=1827.2 J/mol, considering 105 °C-205 °C as relaxation interval, and for the 21 cycles treated sample ΔH_{rel}=3100 J/mol, considering 97 °C-205 °C as relaxation interval. (The present DSC test is

conducted at 10 K/min.) For this case the first heating ramp brings the samples temperature around 300 °C, which allows crystallization to happen; the second heating ramp then is the DSC signal of a crystallized sample, and has a linear behaviour as expected. Since a crystallized sample does not undergo glass transition upon heating it is likely that heat of relaxation calculated with the subtraction method in this cases are overestimated because the relaxation interval is decided arbitrarily.

Regarding the sample that undergoes 21 cycles between room temperature and liquid nitrogen temperature it has also spent 84 hours at 77K during the treatment. So, it is not possible to affirm directly that the increase in the heat of relaxation is due to various temperature changes. Chen Zhen Hua et al. [55] claimed that hundreds of hours at 77K can induce nanocrystals formation in a Cu-based bulk metallic glass. Therefore another DSC experiment has been carried out to separate the effect of time spent at cryogenic temperature and the effect of temperature change. In the following graph are reported other DSC analysis that compare the two possible effect.

3.1.3 The rejuvenation effect of thermal cycling

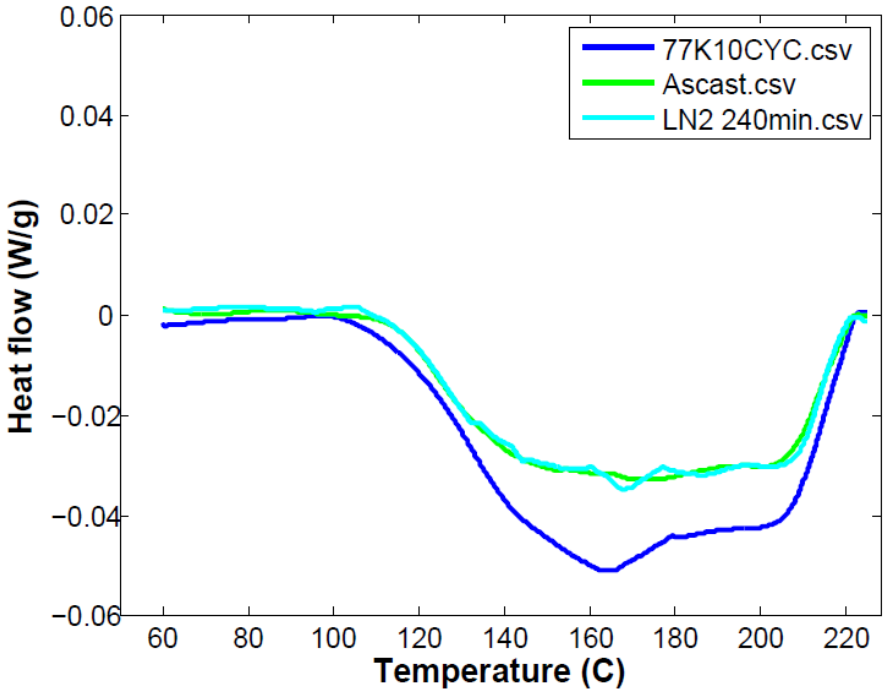

Graph 3.1.3.1: comparison of relaxation spectrum between cycled, as-cast and cryogenically annealed sample

The DSC spectrums reported in Graph 3.1.3.1 are the result of the subtraction of the second heating run from the first one; the measure was conducted at a heating rate of 20 K/min. It results that the sample immerged for 4 hours in liquid nitrogen shows no modification concerning the spectrum of relaxation, if compared with an as cast sample, green and lighter green curves; it is not needed longer time than 4 hours to explore this effect, because samples usually spend much less time at 77K during thermal cycling. It is also evident that the blue curve, corresponding to a sample that experienced 10 cycles in liquid N_2, shows a deeper spectrum of relaxation. Another sample, immerged in liquid N_2 for 10 min, was also prepared and measured in order to compare directly with the 10 cycles-sample, based on the fact that the first one would have experienced just one thermal change while the latter would have spent the same amount of time in liquid nitrogen but experiencing 10 cycles. Unfortunately DSC data of the 10 min sample are extremely noisy and have not been plotted in the graph above. Heat of relaxation is summarized in the following table, Table 3.1.3:

	As cast	240min at 77K	10cycles RT-77K	10min at 77K
Heat of relaxation (J/mol)	761.0	781.2	1110.2	613.0

Table 3.1.3: heat of relaxation for differently treated samples are shown

Again, it has to be pointed out that the heat of relaxation value for the 10 min at 77K sample is probably not true, since the DSC measure is extremely noisy: more likely this small value is due to the presence of organic compounds or dirt. The heat of relaxation values remark what could be observed from the graph above, i.e. room temperature-77K cycling appears to have a rejuvenation effect on the structure of La-based metallic glasses. The values of the heat of relaxation for the as cast sample and for the 4 hours immerged sample are practically identical, i.e. 2.63% variation if any; on the other hand an increase of around 44% is detected when the sample undergoes 10 cycles at 77K.

It is clear that long-time at cryogenic temperature does not affect the thermal proprieties, instead it is the thermal cycle (RT to liquid N_2 temperature) that induces a structural modification. It brings the metallic glass into a less relaxed state with higher enthalpy and higher free volume (rejuvenation effect). This is also the origin of the phenomenon of

relaxation, measurable with a higher heat. Therefore, regarding of the 21 cycles at 77 K sample, we can affirm that the change registered in the heat of relaxation is attribute exclusively to thermal cycling.

3.1.4 Effect of different cryogenic temperatures

So far DSC results show that applying a thermal cycle between room temperature and 77K to La-based ribbons may produce a structural change, leading to a higher energy-state, rejuvenation effect. As previously said in the introduction of this chapter and also in Chapter 1, the rejuvenation effect is probably due to metallic glass' intrinsic structural inhomogeneity; an overall temperature change produces mechanical stresses that induce a structural modification. In this picture mechanical stresses should be proportional to the difference in the thermal expansion coefficient and to the temperature interval imposed in by thermal cycling.

It can be hypothesized then that increasing the temperature excursion would have the same trend on the heat of relaxation.

In this light, we brought out other experiments analyzing the influence of the cycling's cryogenic temperature value on the heat of relaxation. We decided to test two more temperature, liquid helium temperature, 4 K, and dry-ice temperature, 200 K. In the following graphs, Graph 3.1.4.1 and Graph 3.1.4.2, are reported the DSC results. The sample treated in liquid helium undergoes 13 cycles between this temperature and room temperature, and it has been compared with as-cast and liquid nitrogen treated samples only, not with 195 K treated sample, because DSC test on 195 K treated samples were conducted at a different heating rate, 40 K/min, while for helium treated sample the heating rate is 10 K/min. (For each sample a second heating run has been made, so the calculation is performed using the method described above.) For the helium treated sample the second heating run is made after crystallization in order to be compared with as cast and liquid nitrogen treated samples shown in Graph 3.1.1; for the 195K treated the DSC signal which acts as reference is the sample's annealing state.

As it can be visualized in Graph 3.1.4.1 liquid helium-room temperature thermal cycling seems to have a rejuvenation effect on La-based metallic glass ribbons, bringing the material

into an higher energy state, so increasing the relaxation spectrum. However it appears to be less efficient in respect to liquid N_2-RT thermal cycling, disproving in first instance a direct relationship between cryogenic temperature and heat of relaxation. Though, helium treated sample undergoes 13 cycles while nitrogen treated sample undergoes 21 cycles; this could be a possible explanation of the phenomenon: rejuvenation effect is more related to the number of thermal cycles and in a less sensible measure to cryogenic temperature, but it does not seem to be thoroughly convincing. Another possible explanation, consistent with the direct relationship between heat of relaxation and cryogenic temperature, is the following: assuming that higher stresses arise from a larger thermal excursion, it could be possible then, that less cycles in number are required to obtain the same degree of rejuvenation; this implies that the material is capable of reaching more stable state, after a previous increase in its energy state, as consequence of the inducted stimulation, realizing a trend inversion in the heat of relaxation as the cycles number increases. Also in heavily cold-worked metallic glasses was noted an unexpected behaviour of heat of relaxation values [59]. Given this picture, we could say that 13 cycles of liquid He-RT treatment are too much in number, and it is not possible to detect the maximum effect because it was already occurred.

In the following table, Table 3.1.4.1, heat of relaxation values are reported:

	As cast	21 cycles liq. N2-RT	13 cycles liq. He-RT
Heat of relaxation (J/mol)	1827.2	3100.0	2398.6

Table 3.1.4.1: heat of relaxation values for 3 different samples; comparison of different cryogenic temperatures.

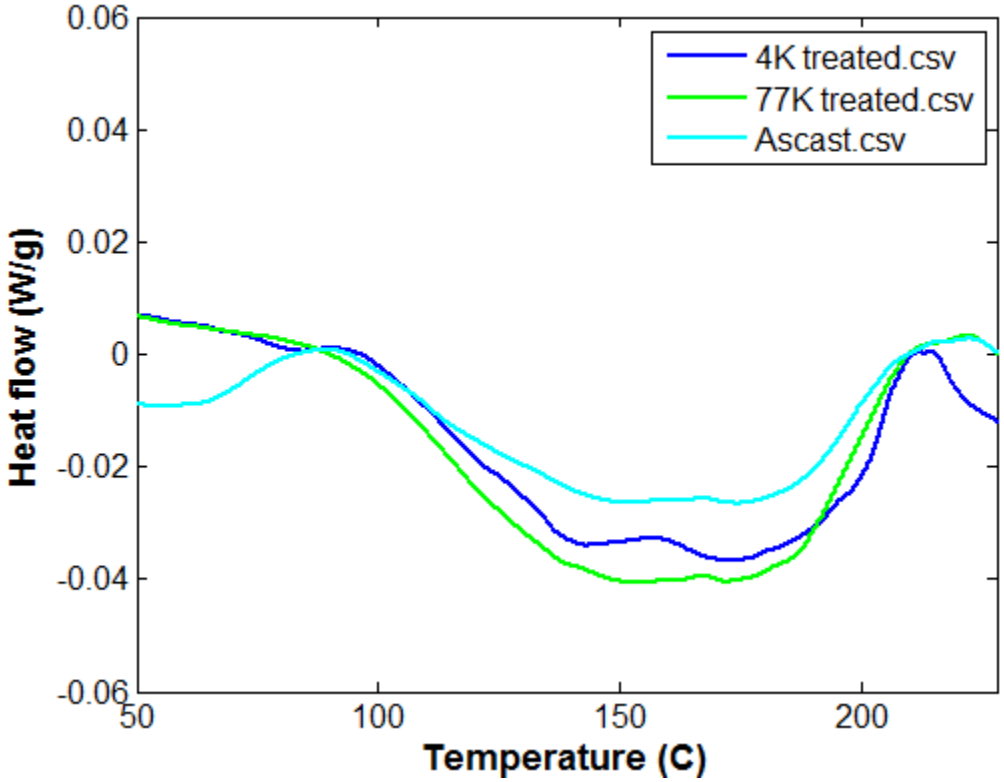

Graph 3.1.4.1: relaxation spectrum for 3 different samples; comparison of different cryogenic temperatures.

Relaxation temperature interval are the following: for helium treated sample 108 °C-205 °C, for liquid N_2 treated sample 97 °C-205 °C, and for as-cast sample 105 °C-205 °C. It has to be pointed out that the helium treated sample's relaxation interval was strangely smaller than the others, so this could provide a possible explanation for the smaller heat of relaxation value.

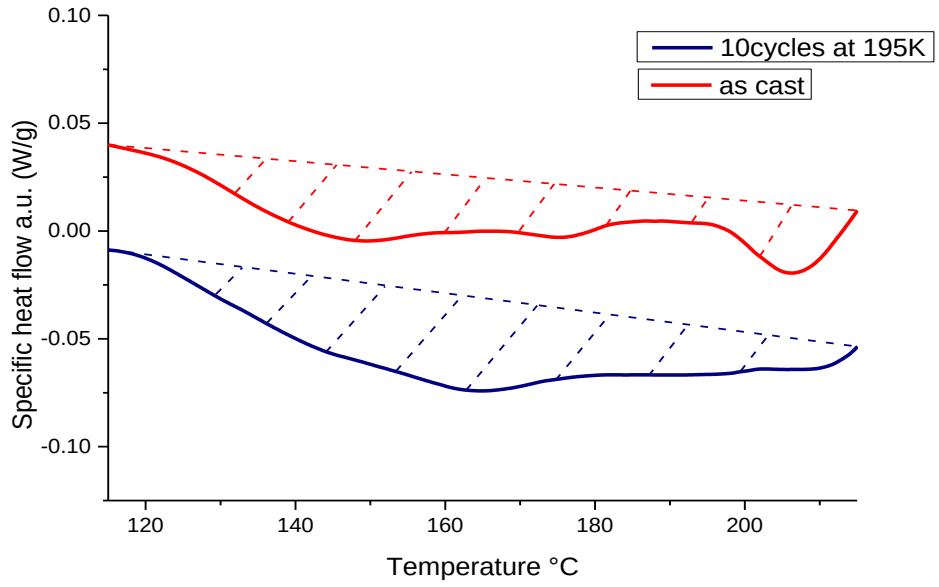

Graph 3.1.4.2: relaxation spectrum comparison between as-cast and liq. CO_2 cryogenic temperature.

Regarding of 195 K treated sample, it has undergone 10 cycles between room temperature and liquid CO_2 temperature. Graph 6 shows a comparison between the spectrum of relaxation of this sample and another as-cast sample. It appears that not a significant difference is present. Calculation of the heat of relaxation shows the following results: for as-cast sample ΔH_{rel}= 567.5 J/mol, while for 195 K treated sample ΔH_{rel}=690.3 J/mol. The relaxation interval considered for the calculation is 115°C-215°C. It appears that a small rejuvenation effect is present also when is applied a thermal cycling between 195 K and RT; an increase in the heat of relaxation of around 20% can be detected. This result seems to confirm the idea that exist a direct relationship between the increase in the heat of relaxation and the cryogenic temperature. Since the helium treated sample and the 195 K treated sample show different trends is not very clear yet if such a relationship is truthful. Unfortunately liquid helium-RT thermal cycling is neither easy nor quick to carry out, so no other tests were produced, also because liquid N_2-RT cycling gave better results regarding rejuvenation.

Despite having abandoned the He treatment more samples have been tested applying -78 °C-RT cycling; the aim is to understand better the effect of different cryogenic temperatures. Other four La-based ribbons have been thermally cycled and DSC measurements have been made. Another as cast ribbon was tested in DSC, a ribbon received a 10 cycles 195 K-RT treatment and two other ribbons underwent a 5 cycles 195 K-RT treatment. DSC relaxation

spectrum are not shown, instead in the following table, Table3.1.4.2, heat of relaxation calculation is reported. All DSC measures, in this case, have been taken using 40 K/min heating rate. The relaxation interval is 115-215 °C for every sample.

	Heat of relaxation (J/mol) with 115-215 °C relaxation interval
as cast (1)	479.7
as cast (2)	564.5
5 cycles 195K-RT (1)	936.8
5 cycles 195K-RT (2)	709.9
10 cycles 195K-RT (1)	690.3
10 cycles 195K-RT (2)	902.8

Table 3.1.4.2: heat of relaxation values for as-cast and liquid CO_2 cycled samples, for a particular relaxation range.

Again it can be observed that a rejuvenation effect is present, however it also shows a big variability in the heat of relaxation values. Furthermore, if a different relaxation temperature interval is considered, the result may change significantly. The onset temperature does not shift significantly for all these samples, so is kept constant at 115 °C, while the end interval temperature is for example set at 222 °C, which value corresponds to the beginning of the supercooled liquid region; this setup gives the following values for the heat of relaxation:

	Heat of relaxation (J/mol) with 115-222 °C relaxation interval
as cast (1)	1094.3
as cast (2)	1276.1
5 cycles 195K-RT (1)	1369.5
5 cycles 195K-RT (2)	1247.1
10 cycles 195K-RT (1)	1079.3
10 cycles 195K-RT (2)	1233.4

Table 3.1.4.2: heat of relaxation values for as-cast and liquid CO_2 cycled samples, for another relaxation range.

A relaxation interval extension of 7°C brings a huge difference in the heat of relaxation values; also, if we compare the results, in the second case, Table 3.1.4.2, rejuvenation is barely visible and only in the 5 cycles 195K-RT samples. This interval temperatures strong

dependence for the heat of relaxation is also due to the fact that the end interval temperature is always in the glass transition zone and mostly over T_g, which should be around 210 °C [54]. (As already mentioned before T_g is difficult to extract from DSC signal, mostly because of its noise.) In this scenario a small change in the end interval temperature may consist in a big change in the area value as the DSC signal in the transition zone possesses a significant slope; also choosing higher end interval temperature equals to counting areas not directly related to relaxation phenomena in the relaxation heat calculation, and that is particular relevant because a subtraction of a second heating run as reference has been performed. In fact, if samples before any heating have different state, more or less relaxed for example, and if the annealing time is not sufficient it is likely that they show different behaviours upon second heating. I think that is exactly the case; considering the second heating run DSC signal, an overshoot peak is present in every of these samples slightly after T_g, however they are not identical, as suspected. Overshoot peak area, calculated taken the supercooled liquid region as baseline, are shown in the following table, Table 3.1.4.3, and graph, Graph 3.1.4.3:

	Overshoot peak Area (W/g)
as cast (1)	0.1561
as cast (2)	0.1778
5 cycles 195K-RT (1)	0.0864
5 cycles 195K-RT (2)	0.1122
10 cycles 195K-RT (1)	0.0955
10 cycles 195K-RT (2)	0.0694

Table 3.1.4.3: overshoot peak area values for as-cast and liquid CO_2 cycled samples

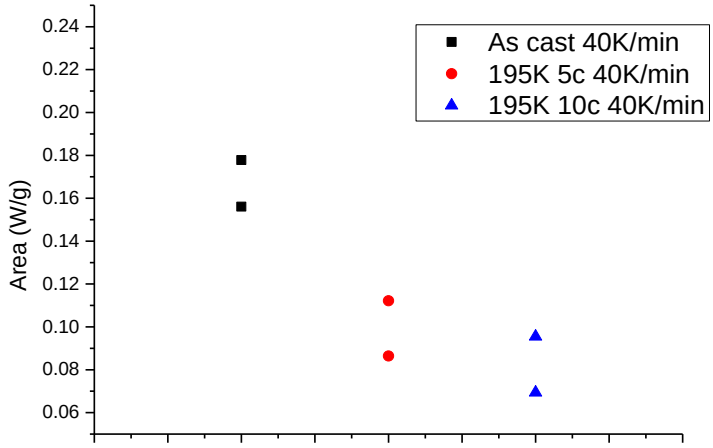

Graph 3.1.4.3: trend with the number of cycles for overshoot peak area values for as-cast and liquid CO_2 cycled samples

As cast samples show the largest overshoot peak, while their extension is decreasing with the number of thermal cycles. Therefore, assuming that the annealing time is not sufficient to achieve a well annealed state it can be deduced that a rejuvenation is present and that it scales with treatment number of cycles and cryogenic temperature.

It can be observed how the heat of relaxation is a time-temperature dependent proprieties, indeed the DSC measurement heating rate influences sensibly its value. In the table below, Table 3.1.4.4, is visualized this characteristic:

	as cast ribbon 10K/min	as cast ribbon 20K/min	as cast ribbon 40K/min
Heat of relaxation (J/mol)	1827	761.0	567.5

Table 3.1.4.4: heat of relaxation values dependence of measurement heating rate

So far it has been studied cryogenic temperature influence on the heat of relaxation, showing that liquid nitrogen-RT thermal cycling induces the maximum grade of rejuvenation for La-based MG ribbons. In the following section a study on how the number of thermal cycles, between liquid nitrogen and room temperature, influences the metallic glass energy state is proposed.

3.1.5 Effects of number of cycles and sample thickness

Number of cycles of 5, 10, 15, 20, 25 was explored. DSC measurements were conducted with heating rate of 20K/min, samples were heated in the supercooled liquid region, around 230°C, and an annealing time of 2 minutes at that temperature was imposed. The annealing time must be suitably long to allow good annealing and to avoid crystallization. A second heating run was also imposed, and again the annealed state has been taken as reference. In the graph, Graph 3.1.5.1, below sample's DSC spectrums are shown.

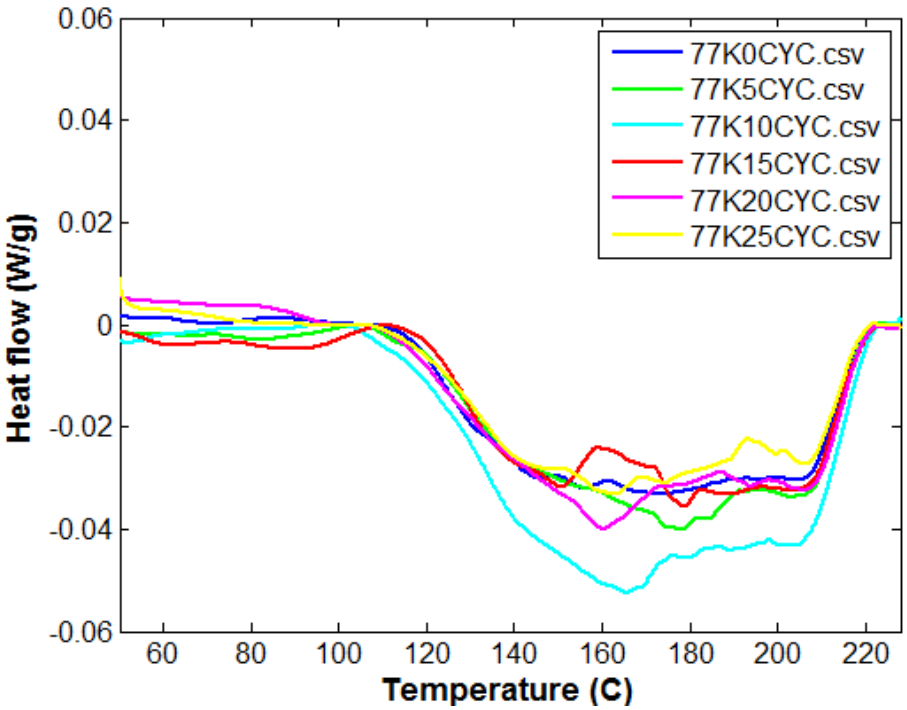

Graph 3.1.5.1: number of cycles effect on relaxation spectrum

Heat of relaxation values, calculated with the same method as above, are summarized in the following table, Table 3.1.5.1. 110°C-218°C has been selected as relaxation interval.

	Heat of relaxation (J/mol)
77K 0CYC (as cast)	750.3
77K 5CYC	809.7
77K 10CYC	1110.2
77K 15CYC	730.5
77K 20CYC	795.9
77K 25CYC	683.4

Table 3.1.5.1: heat of relaxation values for different number of cycles

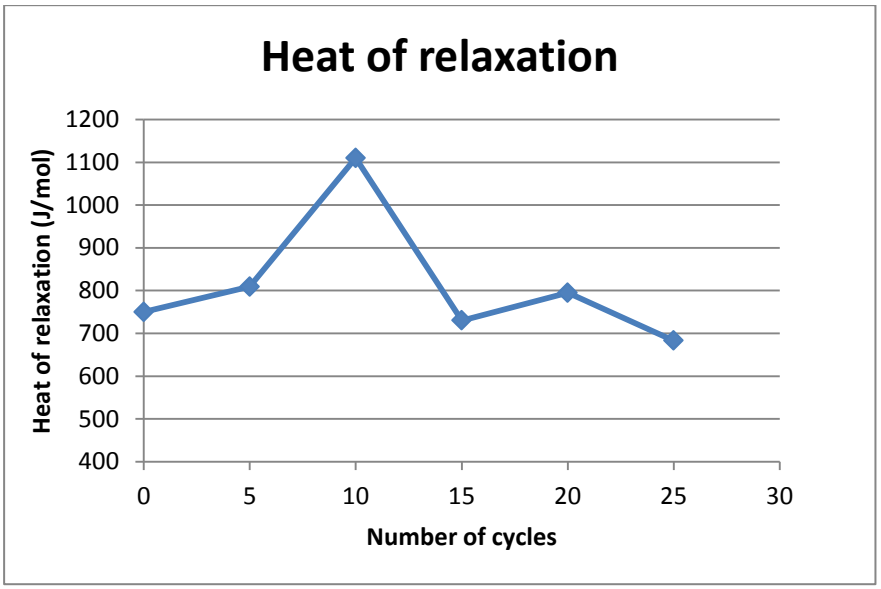

Graph 3.1.5.2: plot of number of cycles versus heat of relaxation relaxation values; clear rejuvenation effect for small number of cycles.

Heat of relaxation appears to increase for small numbers of cycles and reach a maximum at 10 cycles, then further cycles induce a decrease in the heat of relaxation. A possible interpretation of this trend is similar to the one given for the helium treated sample: thermal cycling brings the material into a higher energy state, introducing free volume and increasing atoms mobility; it is likely that, as the stimulation is kept up as cycles numbers increase, atoms may rearrange in more preferable positions, increasing system stability, which corresponds to minor heat of relaxation values. This idea is justified by studies on heavily cold-worked metallic glasses, by peening, in which either rejuvenation and relaxation are detected observing the relaxation spectrum [56,59].

It has been supposed that thermal cycling induces stresses in the material due to intrinsic inhomogeneity in the metallic glass itself, however thermal stresses generated by topological temperature gradients in the sample during the cycling treatment may have a role in the rejuvenation effect. $La_{55}Al_{35}Ni_{10}$ metallic glass ribbons used so far are 3 cm long, 30 µm thin ribbon, therefore temperature gradients that arise when sample was immerged into liquid nitrogen should not be an issue and should not play a significant role. However thermal shock stresses may be more important when considering bulk samples. So, in order to study also bulk samples a preliminary DSC test is needed to understand the role of thermal shock stresses. A La-based bulk rod has been selected and a 400 µm thin disc, were cut from a 3 mm long cylinder. These two samples experienced a 10-cycle liquid N_2-RT treatment. Before DSC analysis, from the cylinder two more thin discs have been cut, one from the cylinder's surface and the other one from the core part; because surface and core of a bulk experience different stresses when a thermal gradient is applied. Thin discs' DSC spectrums are shown in the following graph, Graph 3.1.5.3.

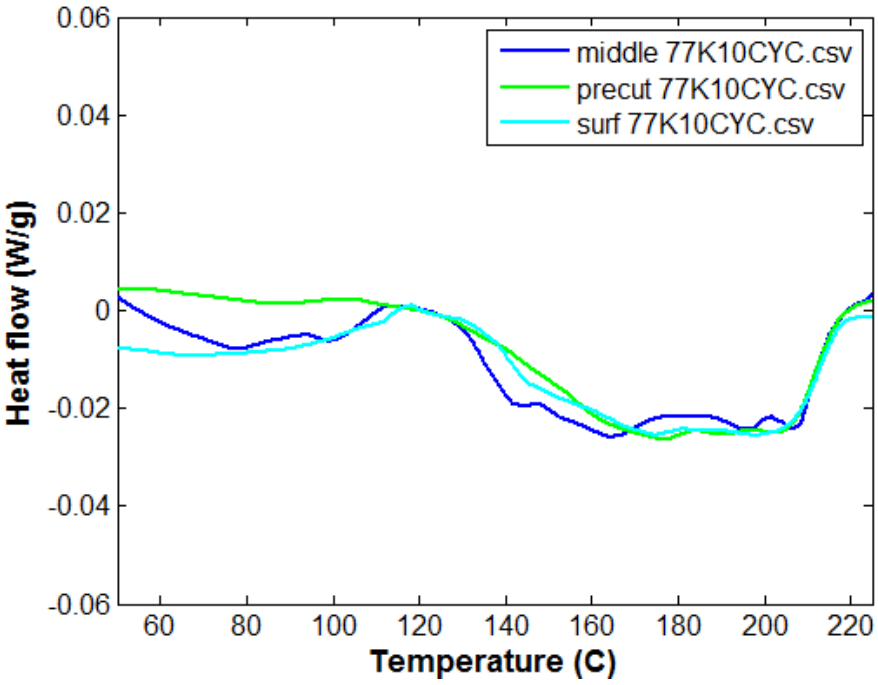

Graph 3.1.5.3: relaxation spectrum comparison of discs cut from bulk samples and thermally cycled 10 times: a pre-cut discs before the thermal cycling and two discs cut after thermal cycling.

DSC test was carried out following the same route as for Graph 3.1.5.1 samples; heating rate is 20K/min and 120°C-215°C is the relaxation interval considered. Relaxation spectrums appear similar. Heat of relaxation values are summarized as follow, Table 3.1.5.2:

	Heat of relaxation (J/mol)
pre-cut disc	461
middle cut disc	488
surface cut disc	436

Table 3.1.5.2: heat of relaxation values for Graph 3.1.5.3 samples

As DSC spectrum observation suggested it appears that thermal shock stresses does not play a significant role in heat of relaxation changes. Further studies then were carried out on bulk samples. Analogously to the cycles number's influence study accomplished for La-based ribbons a similar study, with the aim of verify cycles number effect also for bulk samples, was made. The same number of cycles were explored, 5, 10, 15, 20, 25 cycles, and both thin discs, 200-500 µm in thickness, and bulk cylinder were thermally treated and DSC tested. Heat of relaxation are summarized in the following graph, Graph 3.1.5.4:

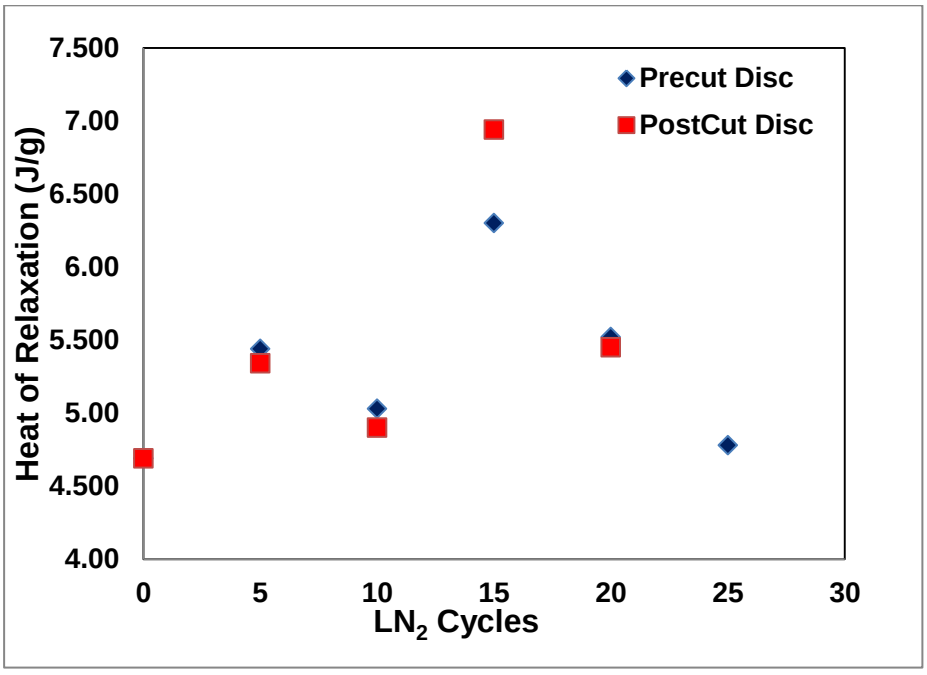

Graph 3.1.5.4: plot of number of cycles versus heat of relaxation relaxation; clear rejuvenation effect for small number of cycles, maximum at 15 cycles.

From Graph 3.1.5.4 it can be observed again that stresses derived from temperature gradient do not trigger any structural modification since there is great agreement between

pre-cut discs and post-cut discs heat of relaxation. It can also be noted, similarly to the previous ribbons study, Graph 3.1.5.2, the presence of a precise trend. For small number of cycles the heat of relaxation increases, even though not linearly (see 10 cycles) and reaches the maximum at 15 cycles; for more cycles it begins to decrease toward the as cast value. Differently from La-based ribbons that show the maximum at 10 cycles, bulk La-based samples display the maximum at 15 cycles. A possible explanation is that bulk samples require more stimulation in terms of stresses to reach an higher energy state.

3.1.6 Discussion and conclusions

In this paragraph discussions and conclusions about DSC results are presented.

1) Thermal cycling between room temperature and cryogenic cycling induce a clear rejuvenation effect, and this is mostly related to temperature change and number of cycles. Time spent at cryogenic temperature do not have any influence.

2) Rejuvenation effect magnitude, given the hypothesis of structural inhomogeneity, should be proportional to thermal cycling temperature excursion. Though, this aspect is still not clear, because of limited data regarding RT-liquid helium temperature. Moreover, it appears that temperature excursion and number of cycles cannot be evaluated separately. Analysis on the effect of number of cycles shows clearly this is a central parameter. Indeed if we consider the cycles number effect a reasonable explanation can be formulated to describe also the helium treated sample result. Liquid nitrogen treated ribbons show a heat of relaxation maximum at 10 cycles and then a decreasing behaviour, thus it is likely that for the 13 cycles liquid helium sample the maximum rejuvenation effect has been surpassed.

3) Thermal cycling on bulk samples demonstrates that stress gradient due to transitional temperature gradient do not play a significant role on heat of relaxation changes, as they are prevalently caused by stresses risen from internal inhomogeneity when an overall temperature change is applied. Bulk samples heat of relaxation variation with the number of cycles appears similar to the ribbons one. Heat of relaxation maximum is obtained for a higher number of cycles, 15; this is probably related to the fact that bulk samples are in a more relaxed state in respect to ribbons, since they are produced with a smaller cooling rate.

4) More difficult to explain is the presence of a maximum at some point in the heat of relaxation for increasing cycles number, and after that a decreasing trend for more thermal cycles. Small number of cycles (before the maximum) dependence suggests a similar effect to the one Schuh found [42], applying cycling elastic loading with a nanoindenter tip, but with opposite results. It appears that thermal cycling induces a certain structural modification that increases the free-volume; a simple explanation is that this modification regards formation or extension of the less dense phase. Another explanation, maybe more accurate, take into consideration free-volume generation when a shear bands initiation site is formed, for example STZs activation/flipping [44,46]. Both hypothesis though do not provide explanation for heat of relaxation decrease for higher number of cycles: activated STZs are retained to be a permanent modification and to be almost immobile [44], annihilation is therefore unlikely. However, it has to be said that heat of relaxation analysis may not be the best technique to spot this kind of modification, for example also in heavily deformed MGs heat of relaxation values did not imply a significant change in the heat of relaxation.

Considerations SBs initiation sites, STZs activation, suggest that cryogenic temperature-RT thermal cycling may be capable of enhancing mechanical properties like tenacity and plasticity [32,33].

3.2 Compression tests

From DSC results shown in the previous section room temperature-liquid nitrogen temperature thermal cycling has a rejuvenation effect also on bulk samples, with apparently no influences by temperature gradient's stresses. In this section it is discussed and analysed if cryogenic thermal cycling may bring beneficial improvements to metallic glass' mechanical properties. In favour of this statement a "rejuvenated" metallic glass, being in a higher energy state (characterised by larger free volume), should show better mechanical properties in terms of ability to deform plastically and resilience characteristics. Also evidence of enhanced plasticity derived from internal inhomogeneity in MG have been demonstrated [33,60].

3.2.1 Cryogenic thermal cycling and mechanical characteristics

For mechanical compression tests $Cu_{46}Zr_{46}Al_7Gd_1$ metallic glasses bulk samples were prepared. La-based samples were not used in this case because they are always brittle at room-temperature [53] and therefore it is impossible to detect any plasticity by a macroscopic compression test. $Cu_{46}Zr_{46}Al_7Gd_1$ samples for compression were prepared in a cuboid shape and each surface was polished down to a 0.3 μm finish with colloidal alumina suspension. Various sample conditions were considered to explore cryogenic cycling's range of applicability: two samples were in as-cast state and four samples were annealed. T_g for $Cu_{46}Zr_{46}Al_7Gd_1$ metallic glass is reported to be around 430°C [53]. Annealing procedure was carried out at 400-410°C: two samples were annealed for 1 hour and the other two for 1.5 hour. Later on it was found that one-hour-anneal results in partially annealed sample (show plastic strain) whereas adding another half an hour renders fully relaxation (no plastic strain). The comparison samples of each condition (as-cast, partially annealed and fully annealed) were thermally cycled (10 cycles in between RT and liquid nitrogen temperature). Mechanical compression test, till catastrophic failure, has been carried out with a position-controlled system/machine, at a constant deformation rate of $10^{-4}s^{-1}$. The force on the sample is measured by a dynamometer with a data acquisition frequency of 50Hz.
Samples' dimensions are summarized in the next table, Table 3.2.1.1:

	Base Area (mm^2)	**Height (mm)**	**λ**
as-cast	2.862	2.645	7.7966
as-cast (10cyc LN2)	3.019	2.936	8.3702
part. annealed	2.910	2.998	8.236
part. annealed (10cyc LN2)	3.243	2.923	8.7604
full annealed	2.447	3.065	7.4696
full annealed (10cyc LN2)	2.421	3.064	7.4218

Table 3.2.1: dimensions, base area and height, and λ factor are presented for compression test samples

Samples' dimensions were controlled accurately in order not to test samples with a high aspect ratio, e.g. aspect ratio = 2. Indeed, it has been reported in literature that, during

compression, failure with no plasticity occurs if metallic glass sample possess a value of λ>= 12, where $\lambda = h(1+\pi d^2 E/4hK_m)$ [61]. With E, metallic glass Young's modulus, d , sample diameter, h, sample height and K_m, machine stiffness. In our case using cuboid samples, as approximation $\pi d^2/4$ has been substituted with the base area.

In the following graphs, Graph 3.2.1.1-3.2.1.5 samples' engineering stress-strain curves are plotted.

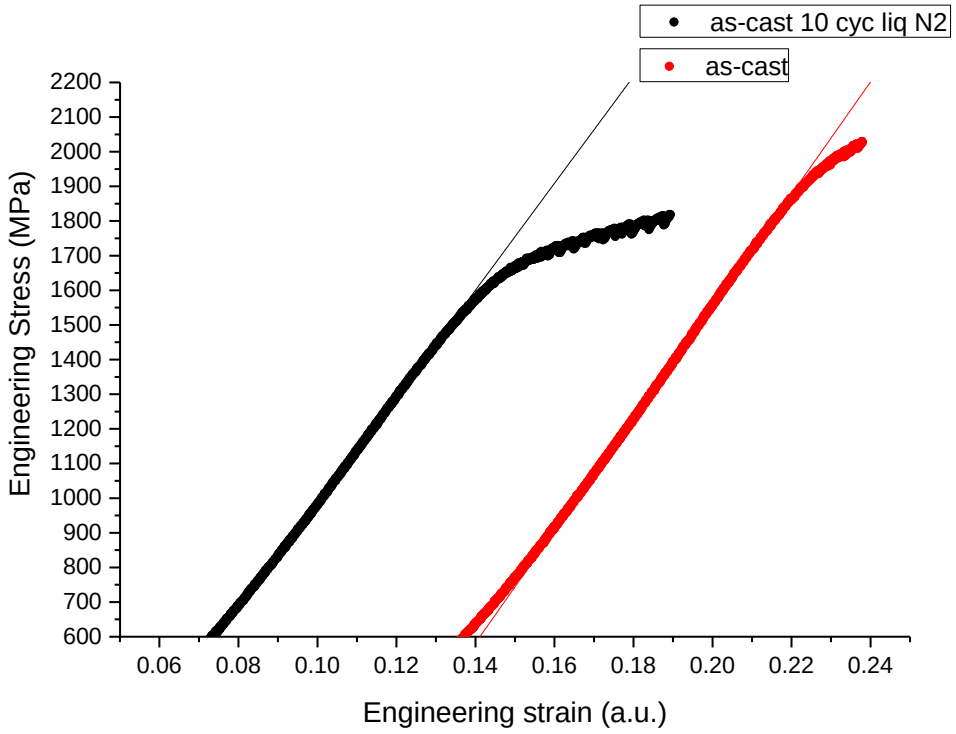

Graph 3.2.1: stress-strain curves for as-cast (red) and as-cast 10cycles treated (black) samples. Machine stiffness has not been subtracted.

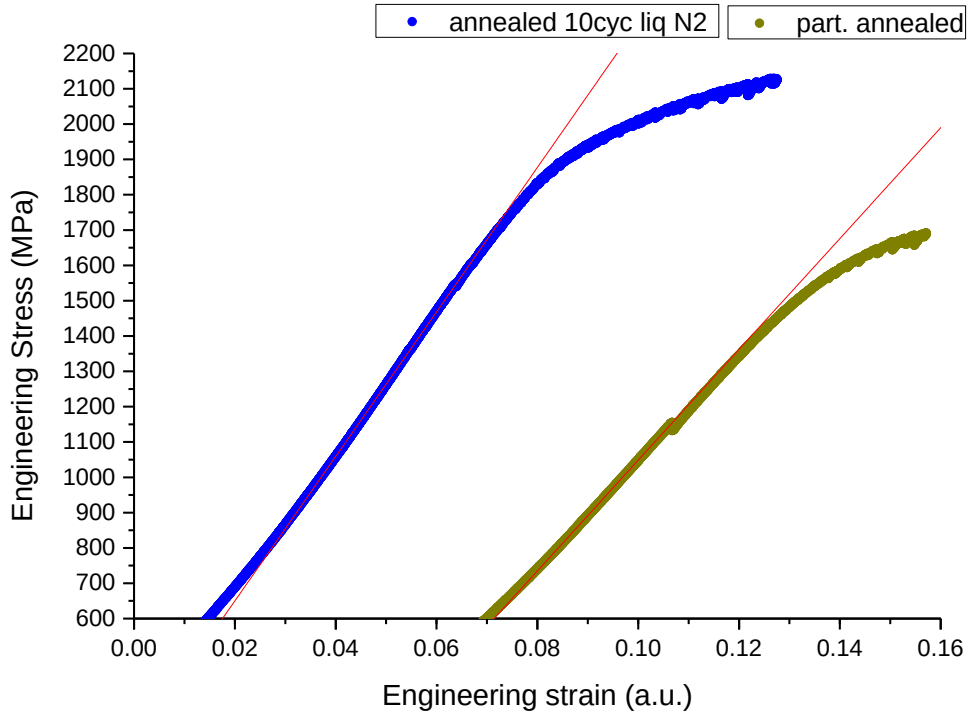

Graph 3.2.2: stress-strain curves for part. annealed (green) and part. annealed 10cycles treated (blue) samples. Machine stiffness has not been subtracted.

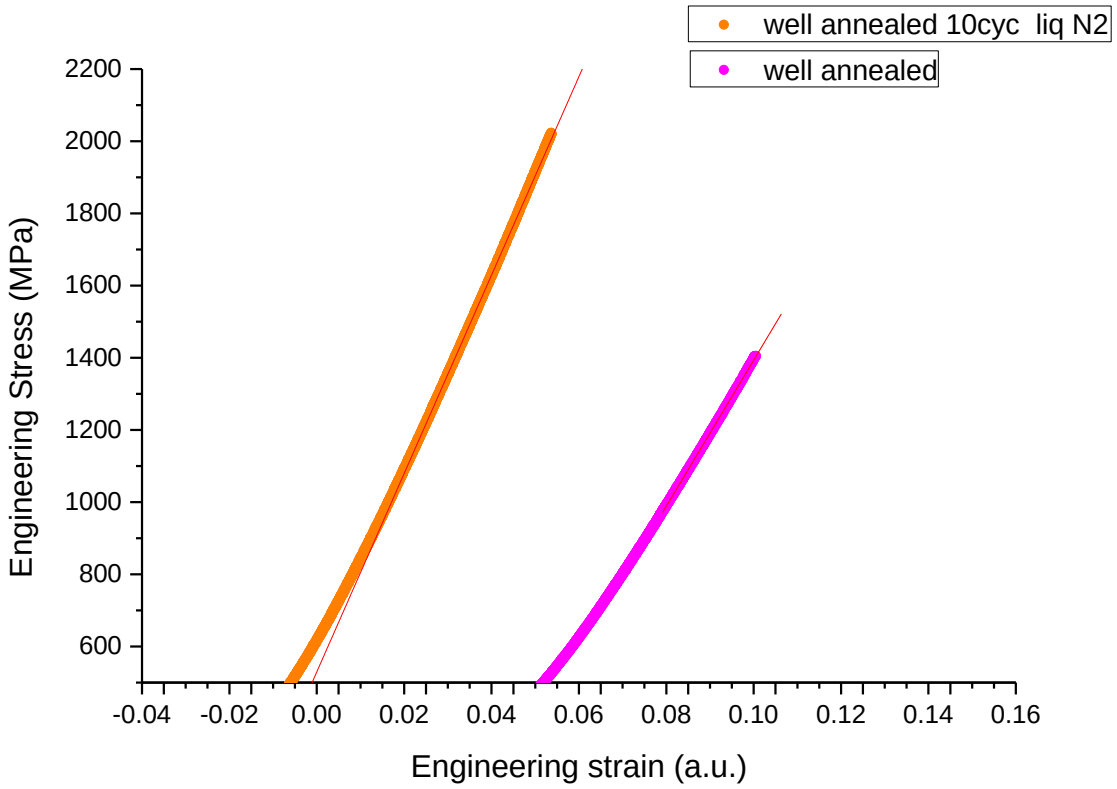

Graph 3.2.3: stress-strain curves for well annealed (pink) and well annealed 10cycles treated (orange) samples. Machine stiffness has not been subtracted.

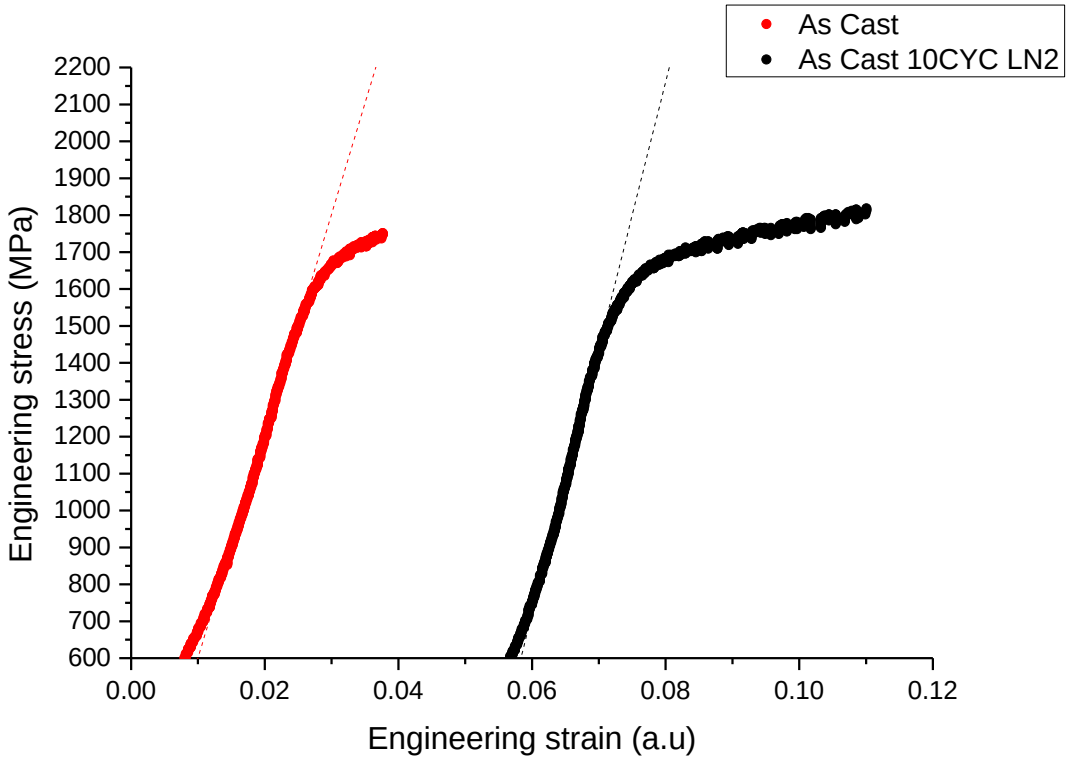

Graph 3.2.4: Machine subtracted stress-strain curves for as-cast (red) and as-cast 10cycles treated (black) samples.

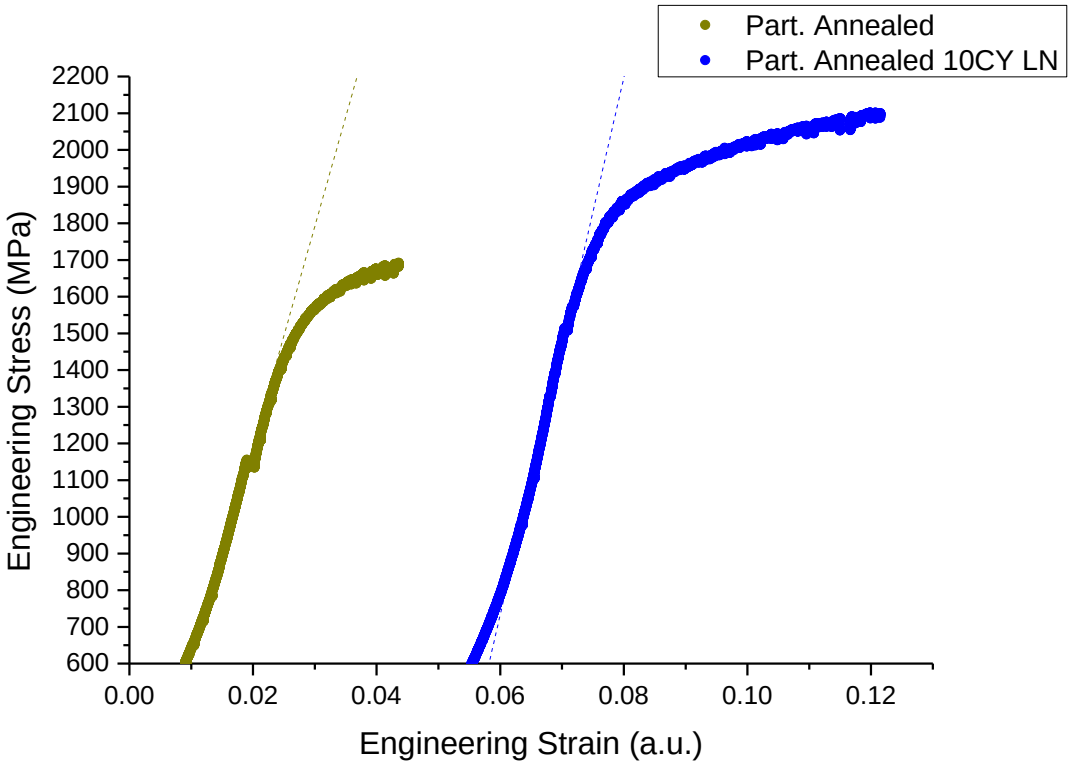

Graph 3.2.5: Machine subtracted stress-strain curves for part. annealed (green) and part. annealed 10cycles treated (blue) samples.

Graph 3.2.1-3.2.3 represent engineering stress-strain curves without any modification. Graph 3.2.4-3.2.5 show samples' engineering stress-strain curves after subtraction of the machine stiffness. The latter has been calculated from experimental tests from which a constant value for the stiffness has been extrapolated.

Main features of stress-strain curves above are summarized in the following table, Table 3.2.2:

	elastic limit (MPa)	**elastic strain limit (%)**	**plastic strain (%)**
as-cast	1560	15.1	2.2
as-cast 10cyc LN2	1430	12.9	6.1
part. annealed	1500	13.1	2.7
part. annealed 10cyc LN2	1358	12.9	7.9
full annealed	1405	10.1	0
full annealed 10cyc LN2	1620	10.8	0

Table 3.2.2: some fundamental mechanical properties of tested samples are reported. They are comprehensive of material and machine deformation.

Plastic deformation is calculated as subtraction of total strain and elastic strain.
Elastic limit, elastic strain and plastic strain are extrapolated from the engineering stress-strain curves, Graphs 3.2.1-3.2.3. It has to be mentioned that anvils and machine deformations are included in the previous curves, therefore all features in Table 3.2.2 are not from metallic glass only. Nonetheless comparisons are still possible and reasonable because a direct proportionality exists between them. The reason why I have not modified curves is that also calibrated curves have significant approximations, introduced by the subtraction itself. Furthermore, the aim of this analysis is not to capture precisely (Cu-Zr)-based metallic glass mechanical properties, rather is to make a comparative analysis to understand the efficiency and the field of work of the cryogenic thermal treatment.

It is clear, from Graph3.2.1, Graph3.2.2 and also from Table 3.2.2 that samples which have experienced 10 cryogenic thermal cycles show better behaviour regarding of toughness. Plastic deformation is significantly higher than its comparison initial state.

Machine stiffness subtraction, visible in Graph 3.2.4-3.2.5, has been carried out to estimate samples' stiffness and Young's modulus. However, strong approximation has been made and

a consistent discrepancy is present with literature data. In the following table, Table 3.2.3, are summarized E and K_S values:

	K_S (kN/mm)	E (GPa)
as-cast	63.5	61
as-cast (10cyc LN2)	72.1	70
part. annealed	60.7	60
part. annealed (10cyc LN2)	73.2	72

Table 3.2.3: stiffness and elastic modulus for as-cast, partially annealed and thermally treated counterparts.

In Graph3.2.2 and Graph3.2.5 partially annealed sample presents a stress-drop in the elastic regime that indicates an apparent plastic deformation; indeed also elastic limit appears to happen at relatively low stresses. This behaviour is probably explainable with the presence of extrinsic flaws, i.e. casting holes, but it was not possible to assess more details of the sample.

Elastic limit shows some variation across the samples but not a clear trend or relationship can be deduced from the data, and that is mainly because of approximations in data analysis explained before. On the other hand plastic deformation behaviour appears to have a relationship with the thermal cycling applied, in particular for as-cast and partially annealed samples. For as-cast samples thermal cycling have induced an increase in plasticity of three times compared to the untreated sample, a similar effect in magnitude is also present for partially annealed samples. Fully annealed samples instead show elastic behaviour until brittle failure, which then occurs without showing any plasticity.

Explanation for this evident enhanced plasticity can be found considering the metallic glass structure composed of two phases, a harder and denser phase embedded (homogeneously) in a softer and less dense matrix, as exposed in Chapter 1. Given this picture, thermal cycling generates mechanical stresses between the phases as they possess different physical properties, in this case the crucial difference is between their thermal expansion coefficients; also mechanical properties such as strength and elastic modulus has been found to be different [30,31,32]. When an external stress is applied, shear transformation zones are more incline to occur in the softer matrix, which has more free-volume and lower critical shear stress; hence numerous shear bands initiate and propagate at different sites to accommodate the applied strain, then the global deformation process occurs through multiple shear bands propagation and operation. The role of thermal cycling is then to

induce a structural modification either enlarging the volume fraction of softer phase or more likely increasing the population of shear bands initiation sites, STZs, mostly in the softer phase. Therefore, plasticity enhancement observed in thermally cycled samples is due to the presence of a significantly larger amount of shear bands, thus global deformation occurs through multiple shear bands; in this process each shear band carries a small amount of shear strain, strain concentration in few primary shear bands is then retarded and rechanneled. This consists then in an energy dissipation mechanism and allows plastic strain to be larger as it is spread throughout a larger sample volume fraction.

3.2.2 Cryogenic thermal cycling and serrated plastic flow features

Plastic flow of CuZr-based metallic glasses, when present, appears to be characterized by a serrated behaviour, Graph 3.2.6. Since cryogenic thermal cycling affects shear transformation zones, their size and distribution, it is possible then that in this serrated zone a different behaviour is detectable between treated and untreated samples. From previous analysis, and explained in previous paragraphs, a large number of STZs can be translated in a large number of operating shear bands. Propagation and nucleation of shear bands generally can be spotted in a stress-strain curve as a stress drop in time and a drastic strain increment in time. Based on what explained, thermally cycled samples should show more shear bands than their counterparts. Is it possible to detected a similar feature from the analysis of the serrated plastic flow?

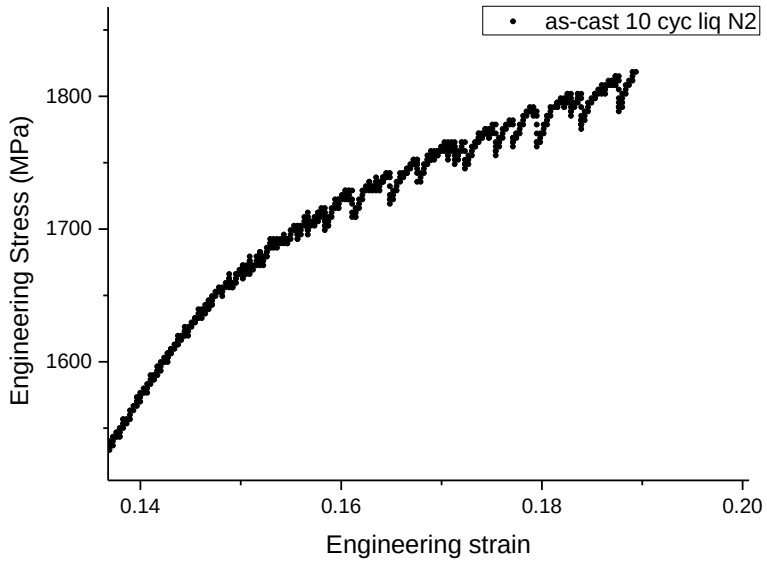

Graph 3.2.6: zoom in to highlight the serrated flow extension for as-cast 10 cycles treated sample

In the next analysis, stress-strain curve plastic zone has been considered. It appears that for both as-cast and partially annealed thermally cycled samples stress drops are more frequent and smaller in amplitude with respect to the untreated counterparts. Stress drops represent either shear bands formation and/or shear step. Larger amount in total number of shear bands and smaller shear offsets on each shear band means a more "homogeneous flow". Schuh et al. called multiple shear bands deformation process as *Homogeneous II type flow* [62].

Results deducted from stress-strain curves in Graph3.2.1, and Graph3.2.2 are presented in the following table, Table 3.2.4:

	N° stress drops	**N° stress drops/ plastic strain**	**Average stress drops Amplitude (MPa)**	**Average stress drops Amplitude / N° stress drops (MPa)**
as-cast	104	47	4.3	0.0410
as-cast (10cyc LN2)	360	60	3.52	0.0097
part. annealed	55	20	3.0	0.0540
part. annealed (10cyc LN2)4	207	27	2.6	0.0127

Table 3.2.4: analysis of serrated flow zone for different samples

All stress drops, after yielding, have been counted and an average value of their amplitude has been calculated.

Samples that experienced cryogenic thermal cycling appear to have a significantly higher stress drops number. Such a huge difference is also related to the extension of the serrated region, which for these two samples is quite larger. However, the same behaviour can be observed even when the specific stress drops number is considered. Specific stress drops number is the stress drops number normalized by the plastic strain. Thermally-cycled samples also show a smaller average stress drops amplitude and it represents a clear signal of a different plastic flow behaviour induced by the treatment. In the last column of Table 4 is presented the ratio between the average stress drops amplitude and the number of stress drops; this factor has been considered to give a representative measure of the shear strain (stress drop amplitude) carried by each shear bands (number of stress drops).

Observations made previously appears to be confirmed by the analysis of the serrated flow zone: thermal cycling induces a structural modification that allows propagation and operation of a larger number of shear bands, shear bands density is therefore increased:

thermally cycled samples present a significantly higher number of stress drops also when divided by the plastic strain. Plasticity in thermally cycled samples is indeed enhanced by higher density multiple shear bands deformation mechanism in which each shear band brings a smaller amount of strain and a higher plastic strain is achieved. This is roughly evaluated by the average stress drops amplitude and by the ratio between average stress drops amplitude and number of stress drops.

The latter two parameters are clearly a rough calculation of what they intend to represent, which is shear bands shear offset. However, the fact that it is still possible to observe a coherent effect produced by the thermal cycling it means that the structural modification is significant.

A clear confirmation of higher shear bands density can be found observing the following pictures, which are micrographs of samples' pieces analysed after failure.

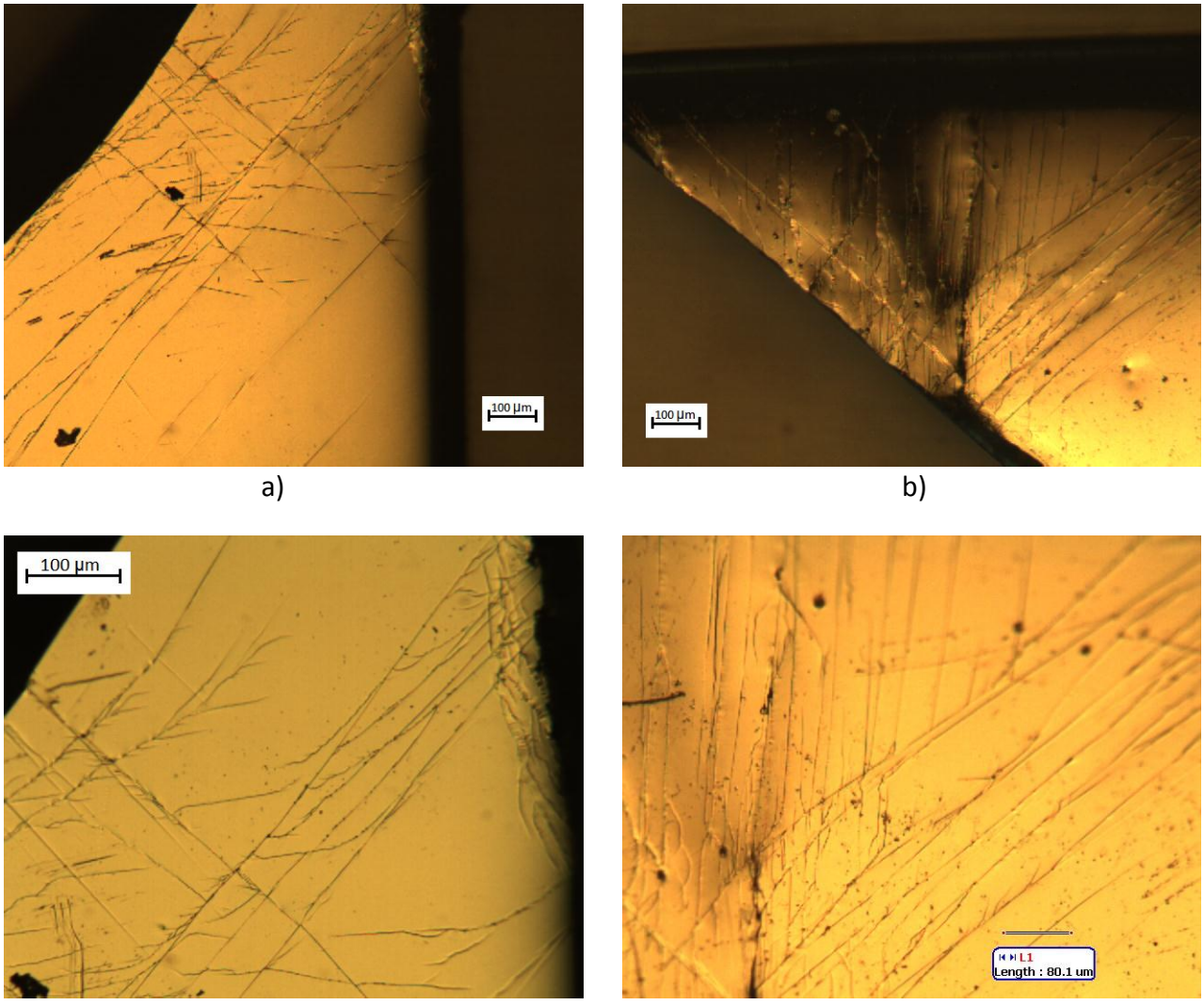

a) b)

c) d)

Picture 3.2.1: micrographs of shear bands patterns for a) and c) as-cast sample, and b) and d)as-cast 10 cryogenic cycles sample.

Picture 3.2.1, a) and c), show as-cast sample, while b) and d) show as-cast 10 cryogenic cycles. It is evident the different shear bands density, accordingly with what it has been observed from stress-strain curves.

3.2.3 Samples geometry, size effect and other factors

Despite clear trends in compressive plastic strain, there are still questions remained to be answered. First of all, it appears quite strange that plastic strain for the partially annealed 10 cryogenic temperature-room temperature sample is the largest, even larger than that of the thermally-cycled as-cast sample. As said before annealing is supposed to reduce free-volume in metallic glass, it is also likely that the degree of structural inhomogeneity, softer and harder phase fractions, is influenced by annealing procedure in the sense that structural differences between the two phases are diminished. In this case mechanical stresses generated by thermal cycling could be smaller as well as the consequent structural modifications, i.e. a less number of STZs is generated, in particular because the cycles number is kept constant. Hence, it is highly unlikely that cryogenic cycling may induce such a relevant change in the plastic strain.

However, applying cryogenic thermal cycling to as-cast samples may not be the best procedure to highlight the enhancement in ductility properties, since as-cast samples possess higher free-volume and STZs fraction, and therefore a saturation mechanism may occur. On this line, cryogenic thermal cycling should have a bigger impact on partially annealed sample, where an increase in STZs density, even though small, can underline a significant change in some properties, such as toughness.

To explain thoroughly the strange result probably some others parameters have to be taken into account, for example small misalignments in the sample geometry may play an important role when the first shear bands occur; another factor may have been structural defects in the sample, such as small bubbles.

Another explanation may lie in samples geometry: can aspect ratio and λ value have an influence on the overall plastic deformation? And can these factors be more important than the structural state? In the following table, Table 3.2.5, these two geometry properties are presented for the analysed samples.

	Aspect ratio	λ	Plastic strain (%)
as-cast	1.56	7.80	2.2
as-cast 10cyc LN2	1.69	8.37	6.1
part. annealed	1.76	8.24	2.7
part. annealed 10cyc LN2	1.62	8.76	8.0
full annealed	1.96	7.47	0
full annealed 10cyc LN2	1.97	7.42	0

Table 3.2.5: comparison between aspect ratio, λ factor and plastic strain for all tested samples

Aspect ratio is calculated as fraction between sample height and the square root of sample base area. λ is calculated as explained in the previous paragraph: as Young's modulus 90 GPa has been considered [53] and as machine stiffness 50 kN/mm has been considered. Relatively large plastic strain can be achieved avoiding the rise of "hot" dominant shear bands that can lead to catastrophic consequences; "cold" shear bands permit to sustain larger plastic strain by a stick-slip sliding process and can lead to multiple shear bands deformation mechanism and extended serrated flow.

It has been found that the serration shear step size is dependent on sample size and machine stiffness: smaller samples and stiffer machines lead to larger shear displacement and so larger plasticity [61]. λ values should give an idea of the tendency of the material to deform with serrated flow or without it (brittle failure). To avoid brittle failure, λ has to remain under the critical value of 12, which is verified for every sample. Higher λ values imply that material's deformation behaviour is moving toward "hot" shear bands and so toward brittle failure. In our case, though, λ is maximum for those samples that showed the largest plastic strain, thus λ values are not an important factor influencing samples' resilience.

Furthermore, from Table 3.2.5, it appears that a relationship between aspect ratio and plastic strain may be present, but it is not particularly clear. For fully annealed samples aspect ratio is maximum and plastic deformation did not occur. For as-cast samples to a crescent aspect ratio corresponds also a crescent plastic strain, which represents an opposite trend in respect to fully annealed samples. Moreover, partially annealed samples aspect ratio values do not offer a better interpretation to understand the kind of relationship present.

3.2.4 Discussion and Conclusions

Compression test results show that thermal cycling between room temperature and liquid nitrogen temperature enhances ductility properties, in particular plastic strain. From the analysis of stress-strain curve and from optical micrographs it has been confirmed that thermally cycled samples present higher shear bands density, and this characteristic is the main reason of improved toughness. The result is therefore coherent with what deducted from DSC analysis.

Higher shear bands density is the result of structural modification induced by thermal cycling. This is explained considering metallic glass composed of two phases, as previously exposed: mechanical stresses arise from difference in the thermal expansion coefficients and can induce “damage” , in the softer phase most likely, since it possesses larger free-volume. For “damage” it is intended activation of shear bands nucleation sites, such STZs. Activation (flipping) of STZs generates an increase in free-volume, as detected by DSC analysis. Shear bands are therefore prone to nucleate and propagate in the softer “damaged” matrix, because of work-softening, so a larger volume of shear bands contribute to plastic deformation. Furthermore, the softer phase is also the matrix of the (hypothesized) structural model so the strain is delocalized throughout the sample. In conclusion more plastic strain is accommodated through strain delocalization and energy dissipation mechanism, i.e. higher density multiple shear bands.

Effect of the number of cycles on toughness properties has not been tested so it is not possible to make a comparison. Thermal cycling, applying a small number of cycles, is retained to induce some form of “damage” to metallic glass structure. From DSC analysis instead heat of relaxation shows a maximum at 10, 15 cycles and then a falling behaviour with the number of cycles. It does not seem reasonable that structural damage is reversible. A possible explanation is reported: thermal cycling induced damage, even if local, initially brings the material in a higher energy level (free-volume generation by STZs activation/generation); subsequently thermal cycles give rise to more damage but also may stimulate some of the modified sites to rearrange their configuration in a more stable energy state. In this way structural “damage” is not healed but heat of relaxation may decrease.

3.3 Nanoindentation Study

In the previous section it has been shown that a correlation between mechanical properties and thermal cycling exists. In this section the aim is to get a better understanding of its nature. Nanoindentation measurements have been carried out for the purpose on both La-based MG ribbons (40 μm in thickness) and rods (3 mm in diameter).

Nanoindentation technique and other similar nano-scale analysis systems caught on in decades and are used to measure mechanical properties of both bulk and thin samples. They are useful techniques, efficient and reliable, capable of testing very small scale, from tens to thousands nm; on top of this they are also sensible and can capture very little change of mechanical properties. With nanoindentation it should be possible to highlight differences in mechanical properties induced by cryogenic thermal cycling more efficiently than with macroscopic/massive compression test. For example, in STZs generation and activation throughout the sample is a good explanation for both DSC and compression test results, it is then reasonable to expect a change also in properties such as hardness, yield pressure and elastic modulus. The tests so far indicate elasto-plastic flow properties are influenced by thermal cycling, therefore (nano)indentation should be able to capture these modifications.

3.3.1 Nanoindentation tests Settings

Nanoindentation technique is not a destructive test, thus it allows the same sample to experience different treatments, different number of cryogenic cycles or different time at cryogenic temperature. Also, since the volume tested by the indenter tip is extremely small, all nanoindentations can be carried out in a small region of the sample surface. These two features are important as they avoid the discrepancy of property among different samples or different area of the sample surface.

The samples, with a thickness of 3 cm, were glued on a cylinder block of aluminium. Nanoindentation technique requires high surface-finish, so bulk samples were polished until 0.3 μm colloidal alumina finish; also, it is very important to check the mounted sample is bent: the residual stress from the curvature deteriorate the experimental results.

Thin ribbons and bulk cylinders samples of La-based metallic glasses have been analysed with nanoindentation technique. The same test parameters has been used in both cases: spherical nanoindentation tip made of diamond with a tip radius of 8 μm; maximum load set at 40 mN; loading rate at 0.5mN/s; hold time of 60 s at maximum load. The machine is in control of force, consequent displacement is measured as distance travelled by the indenter tip. As explained in Chapter 2 the machine automatically calculates some mechanical parameters of interest: hardness, calculated as mean pressure at maximum load; elastic modulus from the reduced elastic modulus, derived from the unloading load-displacement curve; displacement at maximum load. Other important/useful parameters as P_y, yield pressure, reduced elastic modulus in the Hertzian regime and yield displacement have to be calculated manually. In the present study in particular elastic modulus, yield pressure and hardness have been considered as mechanical properties of interest, E and P_y take into account the elastic behaviour while H describes quite efficiently the plastic behaviour. Creep or inelastic deformation/recovery has not been considered since the loading rate is relatively small and a holding time has been imposed.

3.3.1 Nanoindentation on cryogenic treated ribbons

La-based metallic glass ribbons were tested with nanoindentation in order to confirm what DSC results have shown. Therefore, time spent at cryogenic temperature, cryogenic temperature influence and number of room temperature-cryogenic temperature cycles effects have been analysed.

3.3.1.1 Effect of thermal cycles and time spent at cryogenic temperature

Is cryogenic treatment a result of time or thermal cycles? 3.1. paragraph answers this question. Nanoindentation have been carried out to confirm if it was possible to obtain the same result with another technique. '10mins LN' represents the La-based ribbon that has been 'annealed' at liquid nitrogen for 10 minutes. The same sample, after nanoindentation, was thermally cycled for another 10 times. Each cycle contained a 1 minute 'anneal' at

liquid-nitrogen temperature and RT, thus the amount of time spent at cryogenic temperature is the same for the two treatments.

It has been tested at the Nanoindenter in the as-cast state and after each of the two cryogenic treatment. Cumulative distribution of nano-hardness, *H*, and yield pressure, P_y, are presented in the following graphs, Graph3.3.1 and Graph3.3.2.

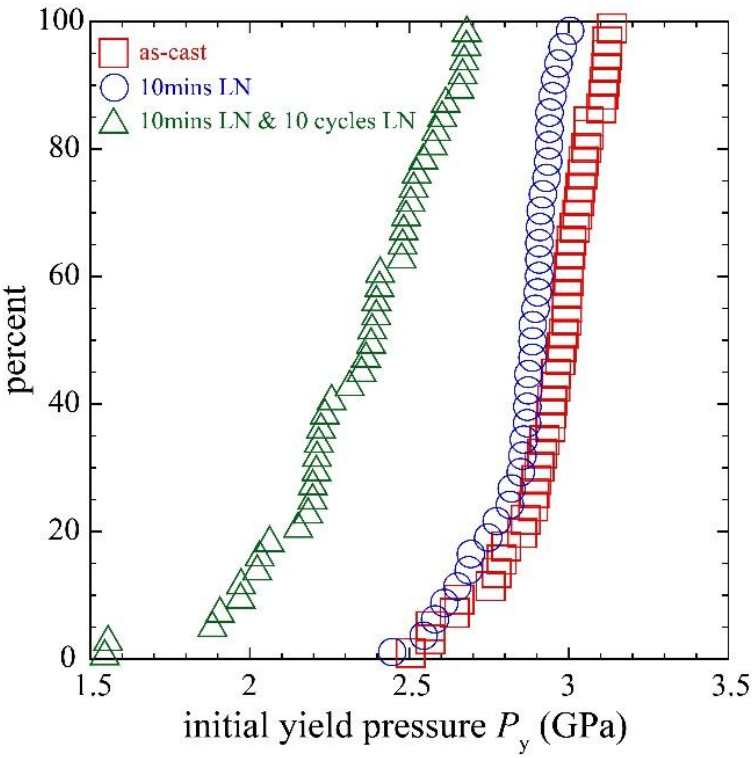

Graph 3.3.1: cumulative distribution of yield pressure calculated at the first pop-in for as-cast(red), 10 min liq. N_2 annealing (blue) and 10 cycles liq. N_2 samples (green). Decrease in P_y for the latter is believed to be a rejuvenation effect.

Yield pressure in this entire work is considered as the mean pressure when the first "pop-in" event occurs. It may be difficult to select it properly and manually, thus yield pressure is calculated with the aid of a Matlab script that is capable, given some input parameters, to identify correctly the first pop-in, based on the load-displacement slope and on the pop-in length.

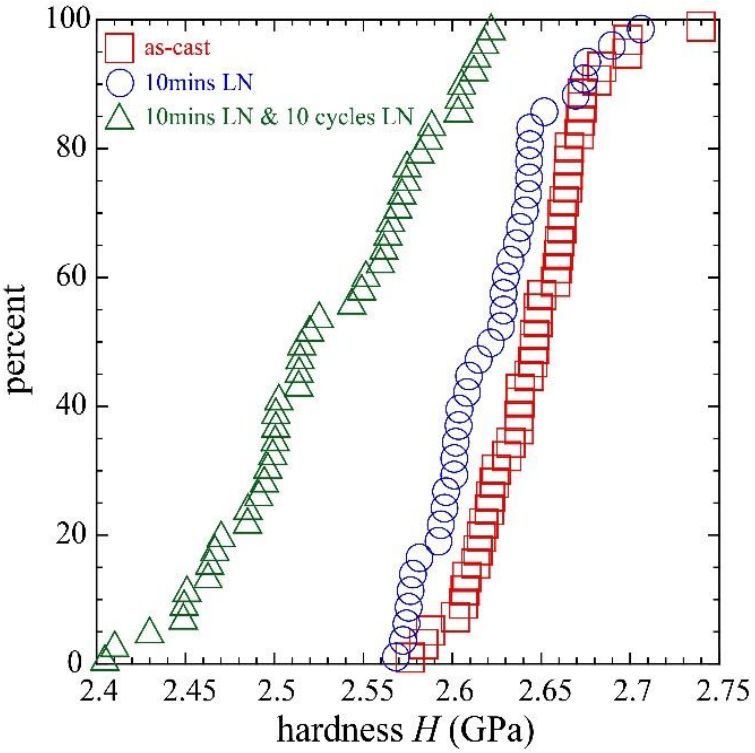

Graph 3.3.2 : cumulative distribution of Hardness calculated at maximum load for as-cast(red), 10 min liq. N_2 annealing (blue) and 10 cycles liq. N_2 samples (green). Decrease in H for the latter is believed to be a rejuvenation effect.

It is observable as the cryogenic annealing did not induce any significant changes in the mechanical properties considered. In both cases, as-cast and 10 minutes hold, the cumulative curves are quite close in position and very similar in shape, confirming the observation. It is also clear that the 10 cycles cryogenic treatment has a more significant influence on these properties, in both cases a softening is detected. Not only the cumulative curves are shifted to small values but also the shape is relative different, smaller slope, indicating a wider values distribution. These results are in good agreement with DSC results and compression test results. Cryogenic thermal cycling induce a modification in flow properties of metallic glass, generating and activating a larger amount of shear transformation; in principle then plastic flow should be easier, observable as a decrease in yield pressure, and also triggering multiple shear bands with an increased displacement, observable as a decrease in hardness values. Thermal cycling should be more effective toward the softer phase, as more STZs are activated there. STZs dimension is still not surely clear, but it is retained to vary from a few tens to a few hundreds of atoms [44], hence they are significantly smaller than the sample volume tested by the nanoindenter. Therefore,

considering the previous statement, an average effect between the two phases is what the nanoindenter tests.

From DSC measurements an increase of around 45% in the heat of relaxation was detected for 10 cycles treatment sample; from compression test the same treatment induced an increase of roughly three times of plastic strain. Nanoindentation detected a relatively smaller property change but still quite significant: considering the distribution median value it results that the *Py* decreases of around 20%, and *H* decreases of around 5%. Furthermore, as specified before, an average effect is surely present, therefore smaller properties changes is reasonably expected. However, despite the difference between the magnitude of property changes across different measurement techniques, nanoindentation result appears reliable and in perfect accord with our hypothesis and other results.

Another thing that can be deduced from nanoindentation is that cryogenic cycling is capable of affecting not only the plastic flow but also the elastic part, since it modifies yield pressure.

3.3.1.1 Cryogenic temperature influence

In the DSC results section, 3.1 paragraph, a comparison between different cryogenic temperatures, liquid helium, liquid nitrogen and liquid CO_2, have been shown. A similar analysis with nanoindentation technique was carried out, testing the two most effective temperatures, liquid helium and liquid nitrogen. Unfortunately liquid helium treated sample showed not really significant results, despite being analysed many times, and therefore a further comparison is not possible. In the next paragraphs attention has been focalised on room temperature-liquid nitrogen temperature cycling only.

Liquid CO_2 treated ribbons were not tested because DSC data showed that cryogenic temperature is not strongly effective.

3.3.1.2 Room temperature-liquid nitrogen cycles number effect

DSC results showed clearly that rejuvenation of metallic glass is related to repetitions of overall temperature changes, thermal cycling, and also that a trend with cyclic number exists: free volume appears to increase for small cycles number and to decrease as cycling is

continued. As regards this trend, if a structural modification, like local yielding, STZs activation, is induced by stresses arisen from thermal change, is still not clear which one between soft zones “generation” or soft zones “annihilation” is the main process as cycling continues. There are several proofs that mechanical stimulation has the potential to induce either relaxation or rejuvenation [42,44,57]. Since metallic glass structures are not stable it seems that a relatively small perturbation is more likely to generate/activate STZs or enlarge them, while a relatively massive perturbation, like massive deformation, cold-rolling, peening and nano-indentation [42,44,57] may have both the results.

To understand better the nature of cryogenic cycling induced flow properties modifications a La-based ribbon experienced 10 cryogenic cycles and after that other 10 cryogenic cycles. Nanoindentation were made on three different states of this sample, as-cast, 10 cycles and 20 cycles. Results of these tests are reported in the following graphs, Graph 3.3.3, Graph 3.3.4, and Graph 3.3.5. In this case, besides P_y and H, also Hertzian reduced elastic modulus has been evaluated.

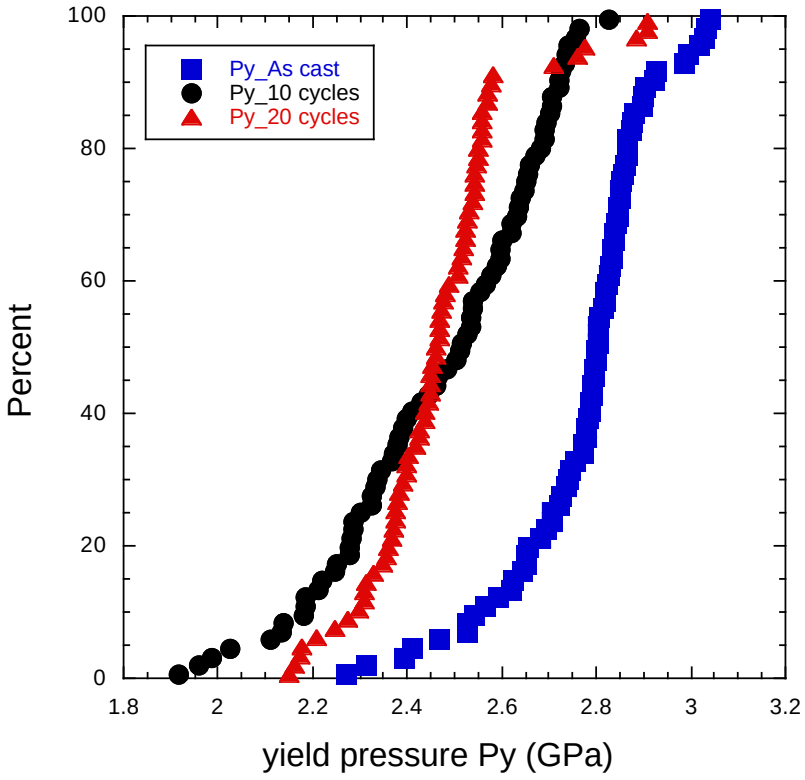

Graph 3.3.3: cumulative distribution of yield pressure calculated at the first pop-in for as-cast(blue), 10 cycles liq. N_2 samples (black) and 20 cycles liq. N_2 (red). Rejuvenation effect is still visible after 20 cycles and seems to be slightly improved.

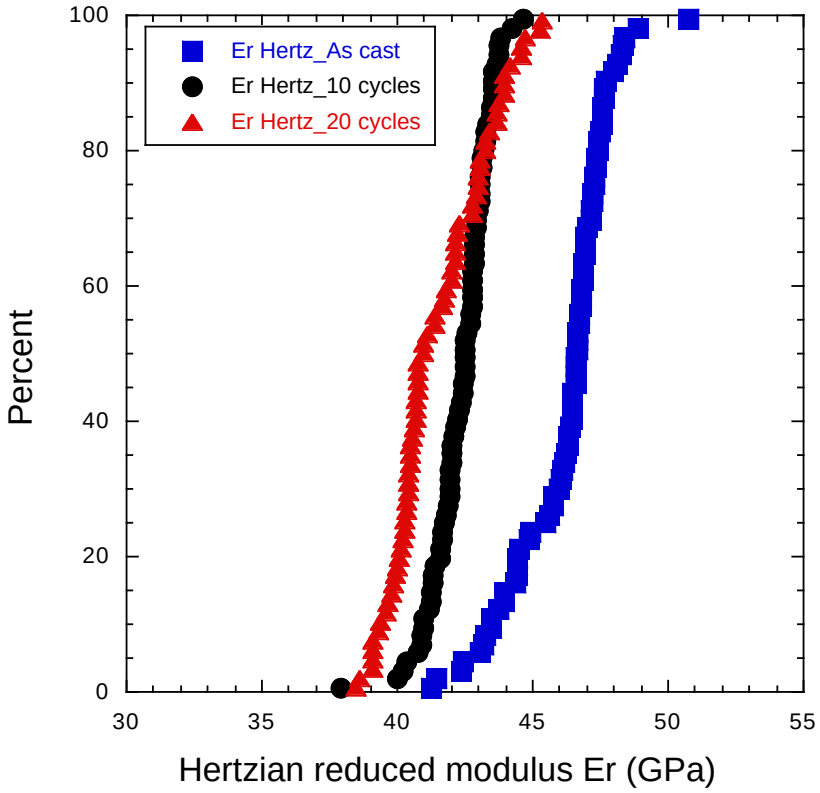

Graph 3.3.4: cumulative distribution of Hertianz reduced modulus for as-cast(blue), 10 cycles liq. N_2 samples (black) and 20 cycles liq. N_2 (red).

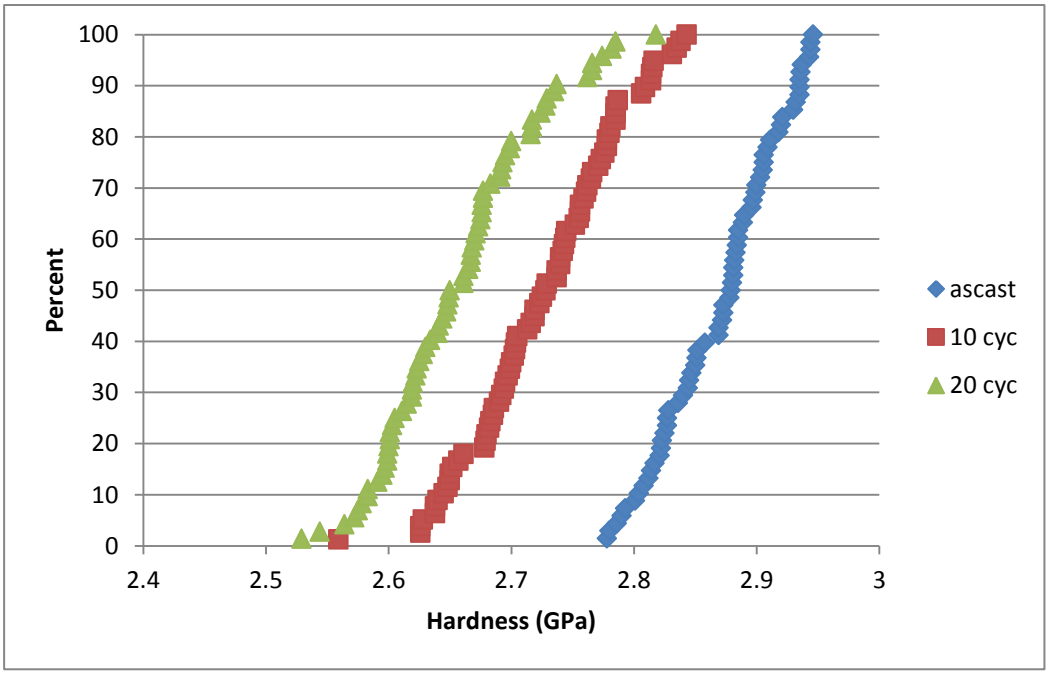

Graph 3.3.5: cumulative distribution of hardness calculated at maximum load for as-cast(blue), 10 cycles liq. N_2 samples (red) and 20 cycles liq. N_2 (green). Rejuvenation effect is still visible after 20 cycles and seems to be slightly improved.

Recalling DSC results, they showed that heat of relaxation decreases right after 10 cycles, which correspond indeed to the maximum. From nanoindentation we understand that modifications of mechanical properties are still possible after 10 cycles. As explained in compression tests discussion, thermal cycling rejuvenation effect consists in "damaging" the structure, through STZs activation, generation or enlargement; as result of these processes free-volume is increased. Though this increase seems not linear with the damage introduced.

Furthermore, we observe similar effects in respect to previous analysis, Graph3.3.1 and Graph3.3.2; thus, this consists in a proof of repeatability. In the following table are summarized the relatively properties change, calculated considering the median value Table3.3.1:

	P_y decrease in respect to the as-cast (%)	**H decrease in respect to the as-cast (%)**	**E_r decrease in respect to the as-cast (%)**
10 cycles	18	6	12
20 cycles	19	8	14

Table 3.3.1: percentage decrease in mechanical properties, yield pressure, hardness and elastic modulus, shown in Graph 3.3.3-3.3.5 with increasing the number of cycles.

Regarding P_y and H the decrease is quite comparable with the one observed previously. It is interesting to note that the 20 cycles treatment brings even further modification to all the three properties considered, deviating from what heat of relaxation DSC results showed. This is not necessarily in contradiction with DSC results: firstly, cryogenic thermal cycling may easily affect different properties in different ways; secondly, in nanoindentation results the 20 cycles treatment seems to reach a saturation, as the change is comparable with the 10 cycles treatment; also there is no strict relationship between heat of relaxation and mechanical properties evaluated by nanoindentation.

However, it has to be pointed out that a 20 cycles treatment may not be the same as a 10 cycles plus 10 cycles treatment. In this experience little studies have been made to comprehend if a temporal effect is present; any structural change that implies a free-volume increase, like STZs extension or flip, have in principle the possibility to be "relaxed", to reverse their condition to a more stable one, as this material's structure is amorphous; though, the time scale of this process is extremely important as relaxation at relatively low temperature could take easily a long time.

A saturation mechanism, in which STZs activation and annihilation/relaxation of high free-volume-highly unstable soft zones balance each other, seems still a better explanation, because even though heat of relaxation has a decreasing behaviour for a 20 cycles treatment in DSC tests, cryogenic cycling should induce mechanical damage in the sample structure and damage should be an almost permanent feature at room temperature. We have to think about what DSC is measuring with the heat of relaxation; for nanoindentation test has been pointed out that exists an average effect. DSC calculated heat of relaxation should in theory be proportional total volumetric amount of STZs, and this seems verified for the first 10 cycles. At some point there will be a saturation amount of STZs because the damage and relaxation rate should balance each other. But what happen to MGs after saturation? Likely STZs size will not remain constant, as damage is introduced by thermal cycling STZs could become smaller and more distributed. Given that, it is even not necessary to keep a saturated volume in the system so that ΔH_{relax} of DSC is reduced. However, more STZs site from which shear bands can nucleate, thus softening is still detected.

3.3.1.3 Repeatability issues

La-based ribbons as already said are melt-spun and that means that they are not perfectly flat since they bring signs of the process making. They also possess a slightly curvature, derived again from the process making. Glue mounting of cast aluminium blocks has some criticalities. It happened indeed that some data were simply impossible to use. To overcome this problem several ribbons were analysed, testing them after 10 cryogenic cycles, which should be the most effective treatment. In most of the cases we obtained a result quite similar to the ones previously shown; in the following graph, Graph 3.3.6 and Graph3.3.7, nanoindentation results regarding another La-based ribbon are presented.

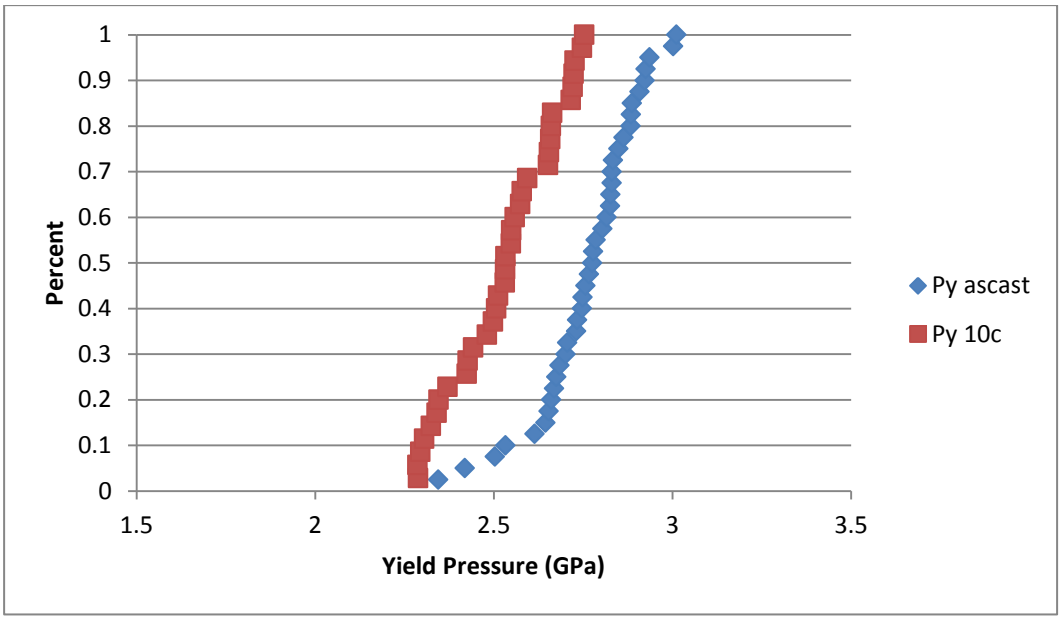

Graph 3.3.6: cumulative distribution of yield pressure calculated at the first pop-in for as-cast (blue) and 10 cycles liq. N_2 (red). Rejuvenation effect is still visible but reduce In magnitude respect to previous cases.

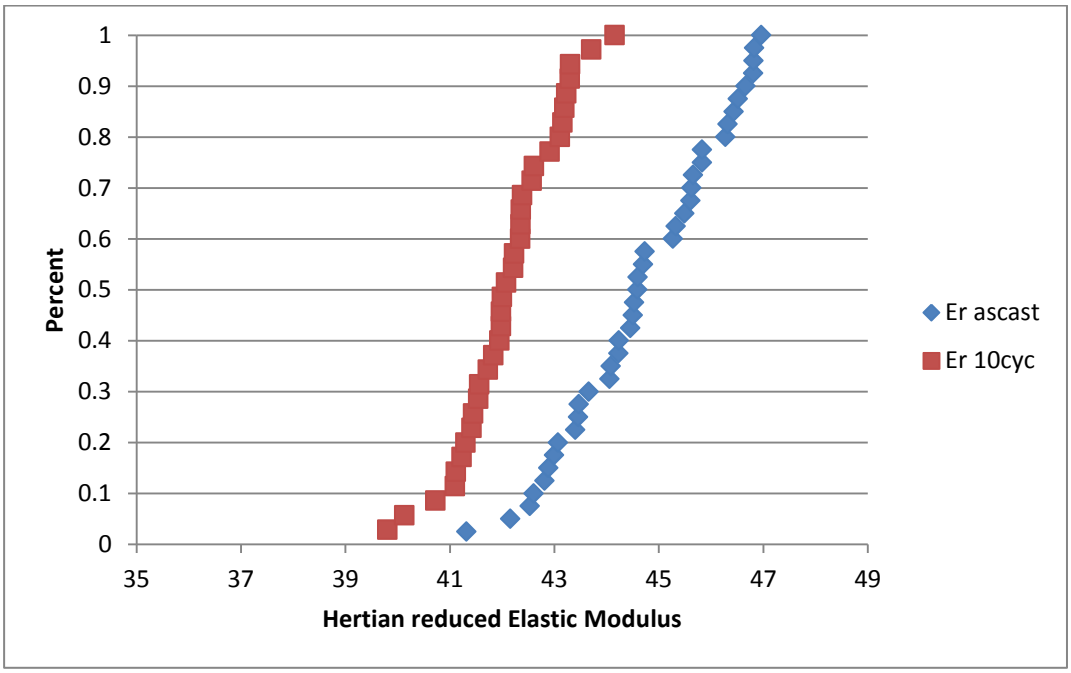

Graph 3.3.7: cumulative distribution of Hertzian reduce modulus for as-cast (blue) and 10 cycles liq. N_2 (red).

For this sample a rejuvenation effect on mechanical properties is still observable, as a shifting of cumulative distribution curve toward lower values is present for both yield pressure and Hertzian reduced elastic modulus. Though it appears that the distribution is not wider than the as-cast state and also the overall shifting is smaller in respect to previous

cases. Considering the median value for yield pressure a decrease of around 10% is detected and for Hertzian elastic modulus a decrease of 6% is calculated.

This result confirms again that nanoindentation detects cryogenic cycling induced relatively small changes in mechanical properties, which nonetheless are quite significant in particular because they give us more information about the nature of structural modification induced by the thermal cycling. However more nanoindentation studies have to be carried out since metallic glasses have an intrinsic degree of heterogeneity and also to analyse other aspects of cryogenic treatment modified elasto-plastic flow, considering inelastic deformation and creep. In particular, elastic modulus modifications may be correlated only to inhomogeneity in the metallic glass structure; topological heterogeneity features in the elastic regime have been studied in fact by several authors [31,32] and, using an atomic force microscope, wide values variations, even around 30%, have been recorded. Though, material's volume tested is significantly different between AFM and Nanoindentation therefore is not reasonable expecting to detect the same variation with Nanoindentation. In any case, strong doubts remain regarding the cause of the elastic modulus change.

3.3.2 Nanoindentation on cryogenic treated La-based bulk samples

From DSC measurements it has been observed that also bulk samples benefit from cryogenic thermal cycling and that they have a maximum increase in the heat of relaxation for 15 cycles. In order to confirm this result a La-based bulk cylinder was polished and prepared for nanoindentation.

It experienced three room temperature-cryogenic temperature treatments: 5 cycles, 15 cycles and 30 cycles. Nanoindentations were carried out in every of this states plus the as-cast state. Results obtained from this test are presented in the next graphs, Graph 3.3.8 and Graph 3.3.9.

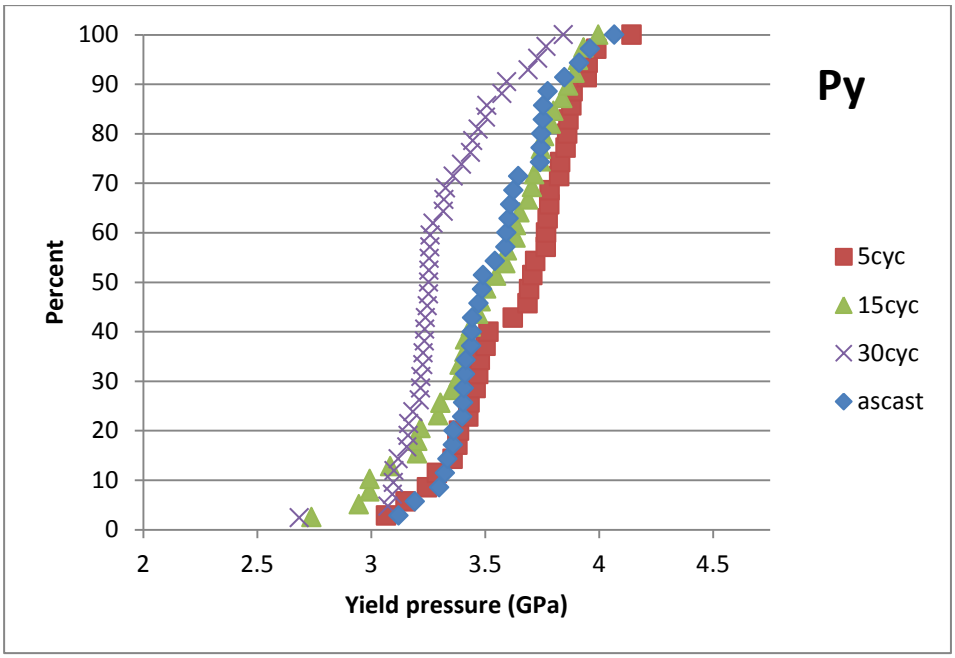

Graph 3.3.8: number of cycles effect on cumulative distribution of yield pressure at first pop-in, for La-based bulk samples. Rejuvenation appears for large number of cycles.

Surprisingly a different trend is observable for the yield pressure and for hardness, which appears to disagree with what DSC results shown. Bulk samples surely have less free-volume than ribbon samples, therefore smaller cryogenic cycling induced property changes are reasonably expected. However what is detected is an increase of both hardness and yield pressure after 5 cryogenic cycles.

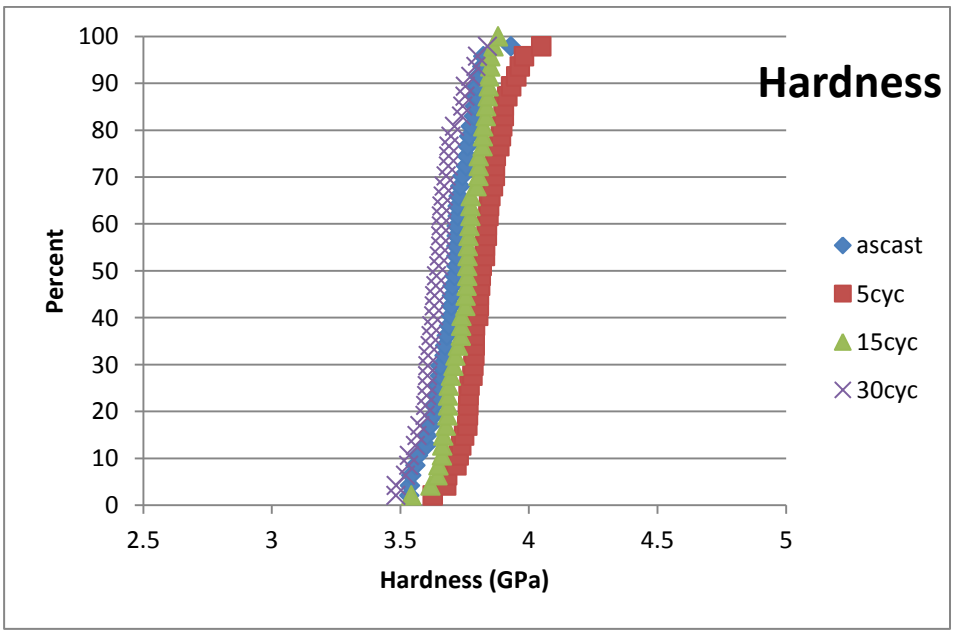

Graph 3.3.9: number of cycles effect on cumulative distribution of hardness at maximum load, for La-based bulk samples. Only a slight change is detectable.

After this increase subsequent thermal cycling induces a decrease in both mechanical properties, and they appear to reach a relative minimum value after 30 cycles. The increase and the overall difference between as-cast and 5 cycles cumulative curves is extremely small, thus doubts about material's heterogeneity and technique suitability are risen. Nanoindentation technique is rather good and reliable in theory, in practice though there are a lot of factors that may affect the measurement, for example external random vibrations, dirt on the surface, also oxide thin layers, and slope/edge effect derived from polishing [42,62]. All these factors together plus an intrinsic metallic glasses heterogeneity make deducing cryogenic treatment effect quite impossible. Graph 3.3.9, is a perfect example of this, as difference between cumulative curves are very small. On this line, a possible explanation for disagreement between DSC results and nanoindentation results is that nanoindentations are made in different zones, with slightly different properties.

Analysing more carefully first pop-in after cryogenic treatment I have noticed interesting features regarding of the first pop-in depth. Results are reported in the following table, Table 3.3.2:

	% pop-in				
	>1 nm	**1.5-2nm**	**2-3 nm**	**3-5 nm**	**>5 nm**
as-cast	78	**13**	**33**	20	11
5 cycles	81	**25**	0	**40**	0
15 cycles	94	7	**25**	**48**	2
30 cycles	94	4	**41**	2	**44**

Table 3.3.2: analysis of first pop-in size and relative events number for different number of cycles. A shift in the size population of pop-in observed.

Increasing the cycles number more pop-in are detectable, which means flow is more often serrated. Also with the number of cycles the pop-in mean size increases as well, in particular it is evident in the 30 cycles treated samples, which also shows smaller yield pressure. I believe that this feature may offer an explanation for the cryogenic cycling effect nature, it may represent the increase in STZs size, contrarily to what suggested before regarding of DSC and Nanoindentation discrepancy with higher number of cycles.

3.3.3 Discussions and conclusions

Nanoindentation analysis on La-based ribbons show rejuvenation effect induced by thermal cycling, consistent with the hypothesis described in previous paragraphs. Thermal cycling appears again to induce generation and/or activation of shear transformation zones which imply an increase in free-volume and changes in some mechanical properties: a 20% decrease in first yield pressure (first pop-in pressure) with a decrease in hardness is spotted by nanoindentation. Small property changes are reasonably expectable as STZs activation mainly should happen in the softer phase and, being STZs very small in respect to nanoindentation tested volume, an average effect is present. Thermal cycling then have a softening effect on metallic glass allowing easier yielding and easier plastic flow with generation of multiple shear bands.

The property change magnitude is however very small, for example in bulk materials, and some doubts exist regarding technique's reliability and influence of other factors such as surface finish and heterogeneity between different area in the samples.

Discrepancy exists between DSC and Nanoindentation results on number of cycles effect; while DSC shows a falling heat of relaxation for higher number of cycles, nanoindentation both on ribbon and bulk shows damage accumulation also for 20 and 30 cycles, therefore a saturation mechanism is probably a better explanation and that heat of relaxation is not completely reliable in describing thermal cycling rejuvenation effect.

3.4 Vickers and AFM analysis

Several analysis on cryogenically treated bulk samples have been carried out and some contradictions emerged in particular considering nanoindentation results. It is not very clear the kind of modification to flow properties induced by the treatment. Furthermore higher number of cycles on bulk samples has not been studied yet.
In this scenario Vickers hardness studies have been conducted on three La-based bulk samples: an as-cast sample, a partially-annealed one and a well-annealed sample.

All three samples have cylindrical shape and have been polished until optimum surface-finish of 0.3 μm colloidal alumina suspension. To avoid heat generation from the mounting resin, the preserve any possible rejuvenation effect resin mounting, which includes heat generation, has been avoided, instead samples have been glued on big steel blocks to obtain necessary parallelism and stiffness.

When the Vickers diamond tip indents the sample surface, various type of shear bands features appear near the indentation edges. They are the consequences of shear stresses induced by the indenter and are precisely shear bands reaching the free surface. Therefore studying these features may be important to understand the kind of modification induced by the cryogenic treatment.

3.4.1 Cryogenic cycling on as-cast sample

A bulk La-based sample experienced three subsequent treatments, consisting of 5 room temperature-liquid nitrogen temperature cycles. Vickers indents were made in the as-cast state and after each thermal cycling. To avoid any possible inhomogeneity along the cylinder axis all Vickers indentations were carried out on the same surface, therefore a suitable load of 500g was chosen. The following graph, Graph 3.4.1, and table, Table3.4.1, show hardness results obtained.

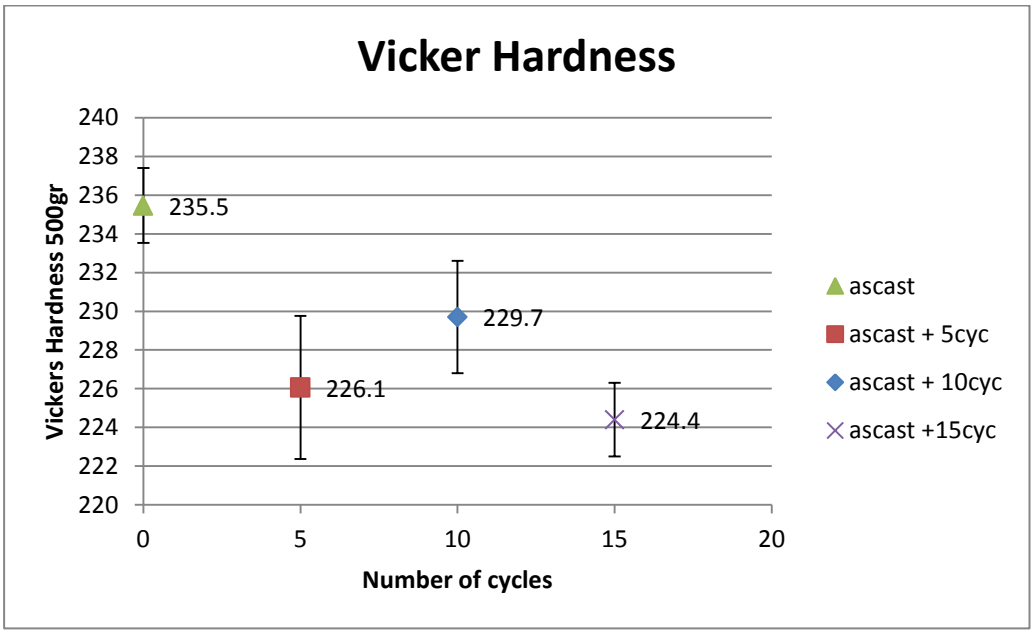

Graph 3.4.1: Vickers hardness comparison for small number of cycles on the same as-cast La-based sample. Rejuvenation effect can be observed.

	as-cast	5 cycles	10 cycles	15 cycles
Average HV (kg/mm^2)	235.5	226.1	229.7	224.4
Standard deviation	1.9	3.6	2.9	1.9
% decrease respect to as-cast	--	4%	3%	5%

Table 3.4.1: Vickers hardness comparison for 5, 10, 15 cycles on the same as-cast La-based sample. Average hardness, standard deviation and % decrease are considered. Rejuvenation effect, proportional to the number of cycles can be observed.

A clear trend can be observed accordingly to DSC heat of relaxation measurement, at 15 cycles cryogenic thermal cycling induces a maximum modification. La-based metallic glass appears to become softer as the number of cycles increases. However, if the percentage hardness change is considered this cryogenic cycling induced modification appears to be relatively small. However it appears quite consistent, it is observable indeed that 5 cycles, 10 cycles and 15 cycles error bars do not overlap with the as-cast value and only a little overlap is registered between each other. As already explained in previous paragraphs, bulk metallic glasses possess less free-volume than ribbon samples, therefore properties modifications range is expected to be smaller, as it is not reasonable to suppose that they are capable to sustain a large free-volume change.

Despite the relatively small change detected in the hardness, a much more interesting effect induced by the cryogenic thermal cycling has been observed: with the number of cycles more and more shear bands reaches the free surface, near the print edges. Unfortunately they are barely visible, and could be seen only with optical microscope; hence, the resolution is not high. In the following pictures, Picture 3.4.1-3.4.8 micrographs of some Vickers indentation belonging to each state measured are reported.

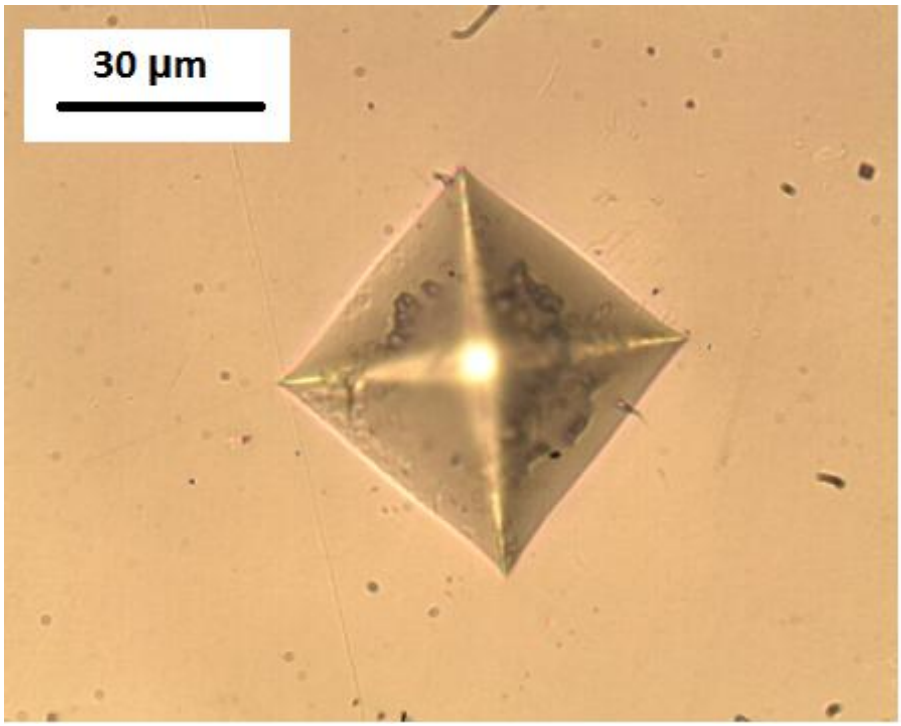

a)

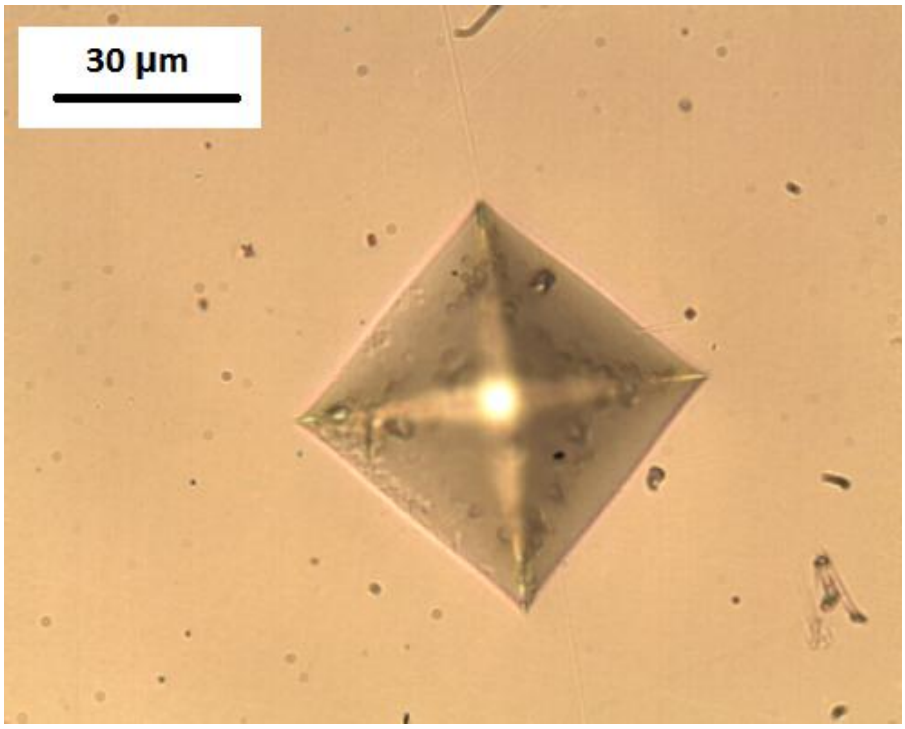

b)

Picture 3.4.1: Both a) and b) micrographs, 500x magnification, show Vickers imprint of MGs in the as-cast state. No particular features can be noted

As-cast Vickers imprints appear as normal vickers with straight edges and no particular features can be noted.

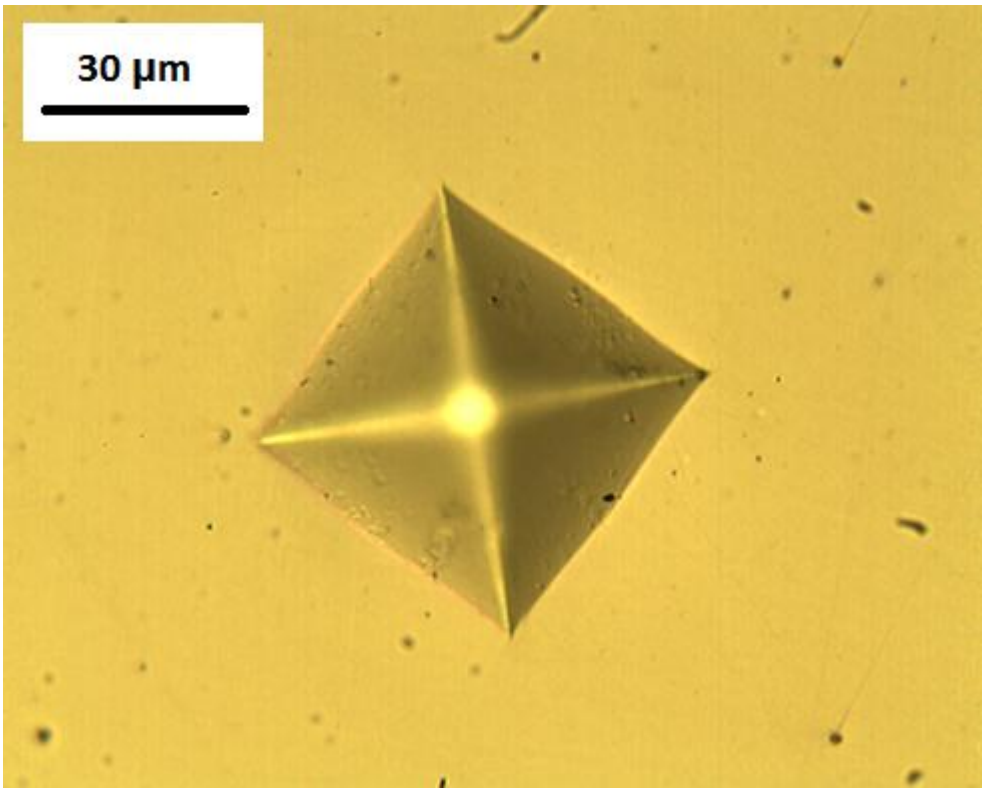

a)

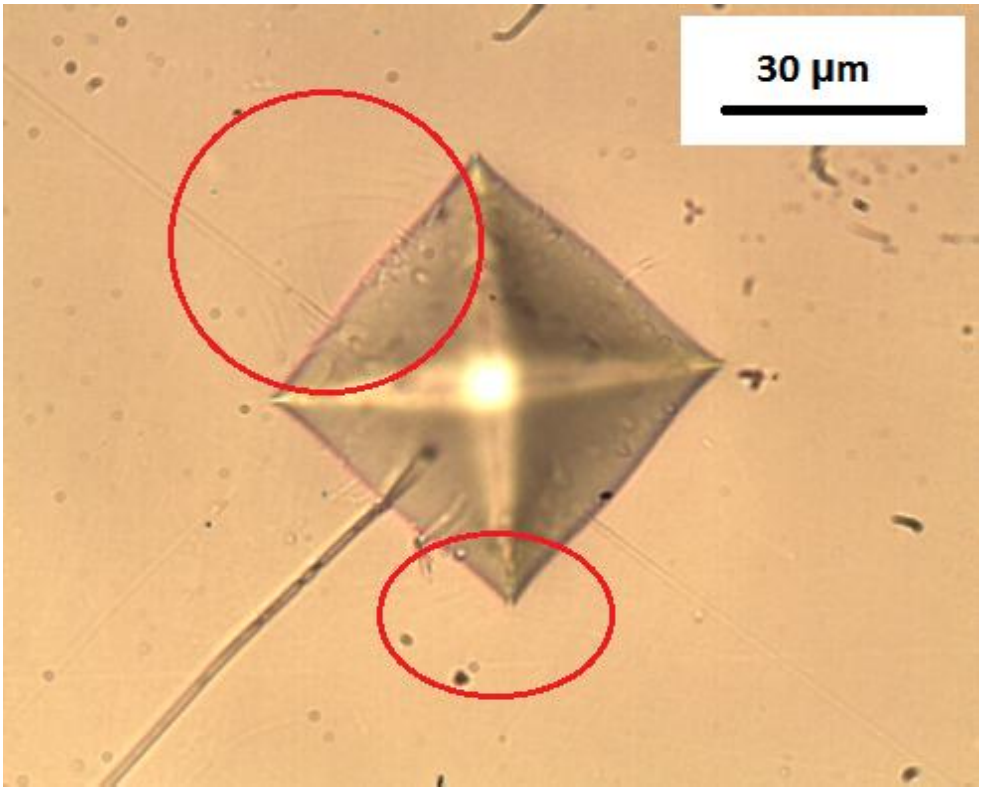

b)

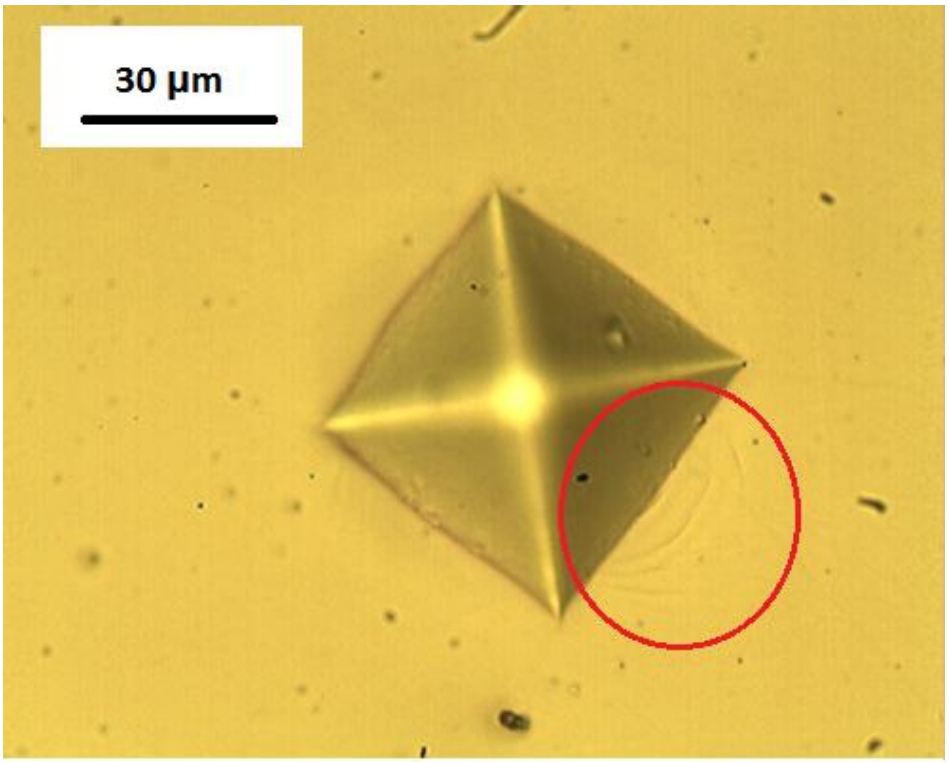

c)

Picture 3.4.2: pictures a), b) and c) are micrographs, 500x magnification, of Vickers imprints made after 5 cycles. In the reds circles shear bands have reached the surface.

Differently from the as-cast state some Vickers indents after 5 RT-liq. N_2 cycles clearly show some hemispherical and radial shear bands near imprint's edges. Not every indent has these pile-up features, see Picture 3.4.2 a). Also the edges shape in some case appears more convex.

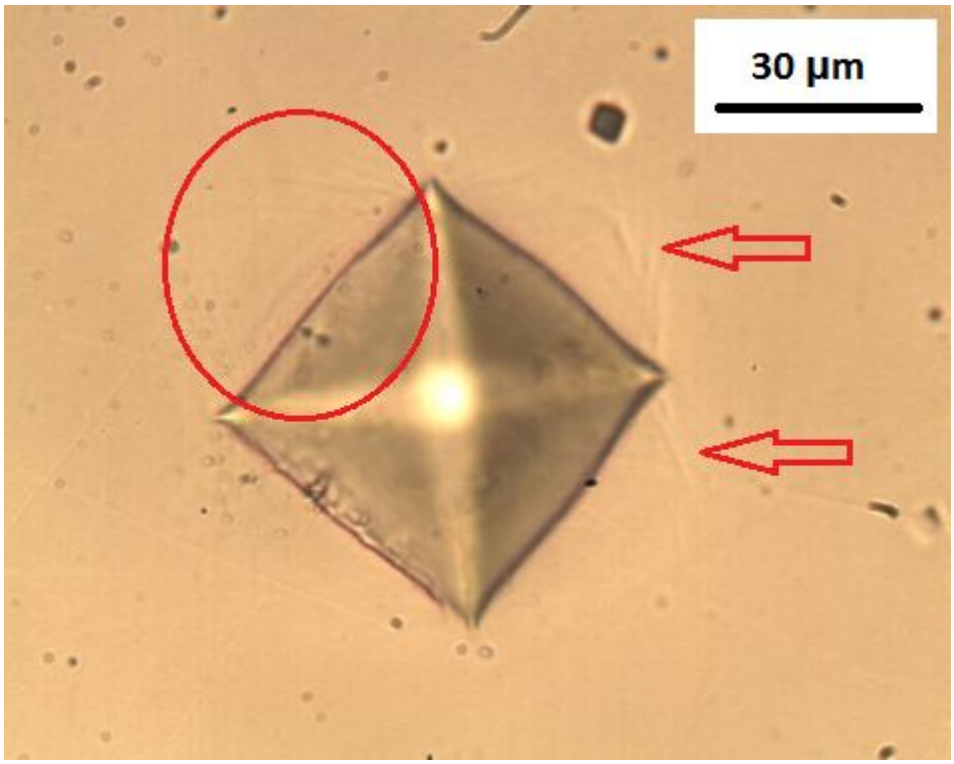

a)

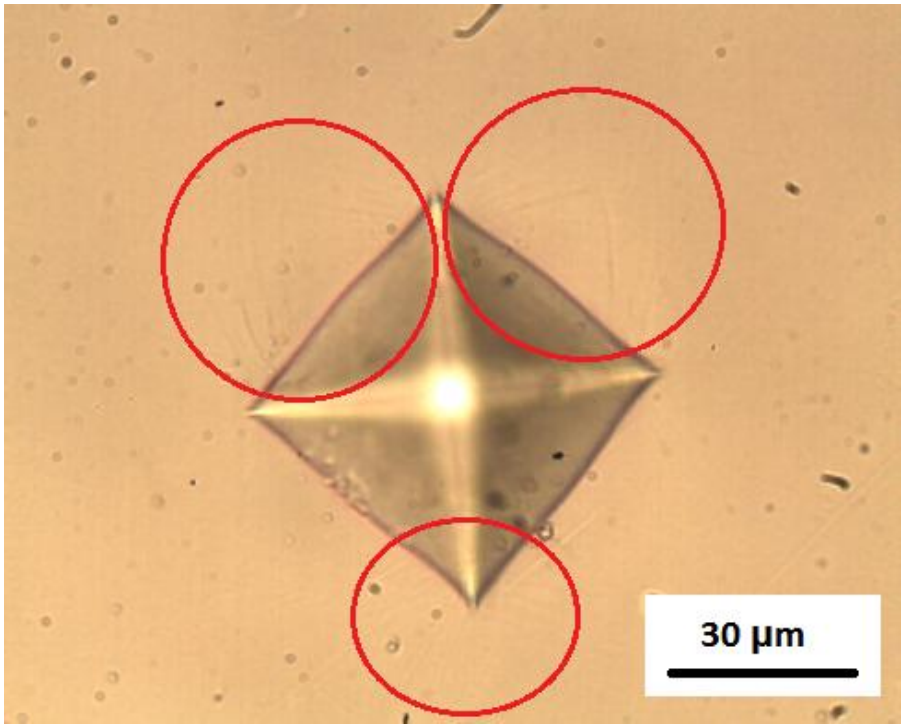

b)

Picture 3.4.3: pictures a), b) and c) are micrographs, 500x magnification, of Vickers imprints made after 10 cycles. In the reds circles shear bands have reached the surface.

Vickers indentations after 10 cycles show constantly pile-up, for every indents; index that a rejuvenation process is going on incrementing the number of cycles. Shear bands are still

radial and semi-circular, but mostly radial, and they also seem to be distributed more homogeneously around the four imprint edges.

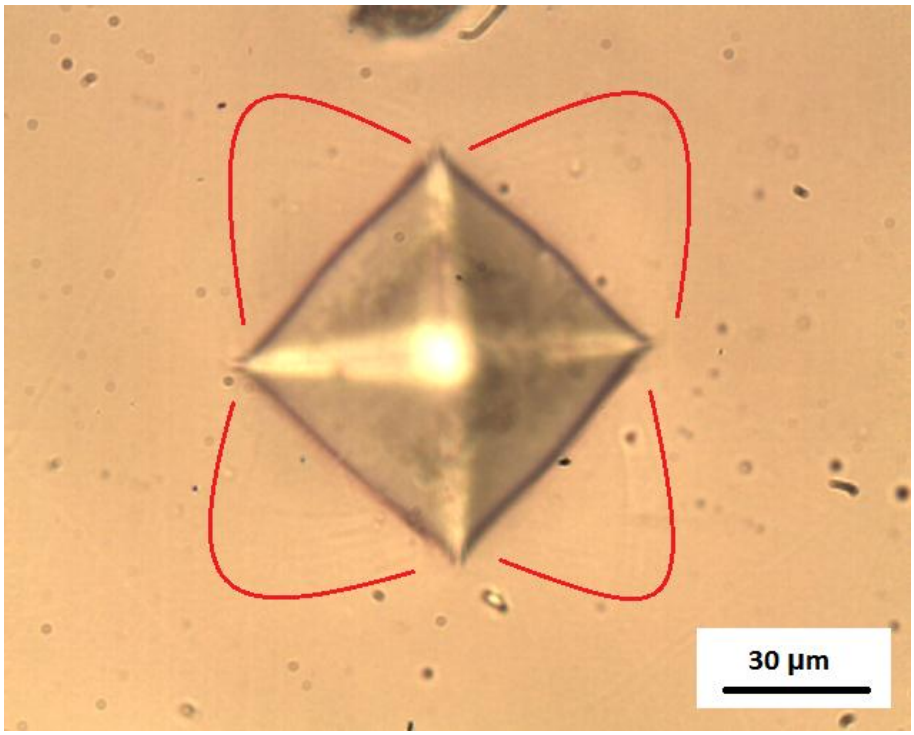

Picture 3.4.4: the present micrograph, 500x magnification, is of Vickers imprints series after 15 cycles. Barely visible there are thin and multiple shear bands on each edge.

After 15 RT-liq. N_2 cycles all the features noted in the previous series are still present, also shear bands appear in increased number and are also thinner. Furthermore, as highlighted in Picture 3.4.4, the deformed zone around the imprints is extended. Indeed, as expected from a more plastic material, the stress and strain field is delocalized or a larger area.

It is also interesting to note that Vickers indentations after 5, 10 and 15 cycles possess a different shape, the edges are indeed convex. Similar shape are usually connected to more ductile materials, thus it is suggesting that, once again, rejuvenation effect induced by cryogenic thermal cycling consists in increased ductile behaviour, as plastic flow results facilitate and governed by generation and slide of multiple shear bands.

As outlined before, it can be noted that with the number of cycles also the number of shear bands near the print edges increases. Furthermore, the pile-up zone around the indentations seems to enlarge with increasing the cycles number. A measure of ductility for metallic glasses derived from Vickers measures is the ratio between the size of pile up, δ,

(distance from the edge of the indenter imprint to the most outer shear band) and the total deformation zone, Δ, (distance from the centre of the indent to the most outer shear band in the pile-up) [63]. Unfortunately in this case is not possible to measure with a reasonable sensitivity both of these two parameters; however from optical observation the total deformation zone appears larger so it is highly probable that indentation made after cryogenic treatment present a minor δ/Δ ratio, which in fact means a more ductile material.

The total absence of pile-up in the as-cast indentation is rather interesting and an interpretation key could put in correlation the presence of shear bands near print edges not directly with hardness values but with the kind of deformation regime [64]. Pd-based metallic glasses always show pile-up in almost every indentation condition (load and indenter shape), and that is likely because they easily enter the plastic regime as they possess an high value of the ratio $E/\sigma_{y,c}$, around 70. Crystalline metals, which have $E/\sigma_y >$ 100 also enter easily the plastic regime. In other words their elastic regime is quite narrow. Other metallic glasses, like the La-based in this study, have a much smaller $E/\sigma_{y,c}$ ratio, around 40-50, therefore the fully plastic zone is not always reached. Decrease in yield pressure is observed in nanoindentation study clearly. And from previous micrographs shear bands at print edges become more and more visible as damage is accumulated through thermal cycling. This means that thermal cycling has shrunk the elastic and elasto-plastic regime and enlarged the plastic regime. The material is then easier to enter the plastic regime, lower stresses, and the flow appears to be characterized by larger serration. This results completely agree with what has been deduced by DSC, compression tests and nanoindentation analysis.

3.4.2 Cryogenic cycling on partially annealed sampleù

Annealed and partially annealed bulk samples were tested only with compression tests after a cryogenic treatment of 10 cycles. In this section higher cryogenic cycles number effect is explored. In particular it is very interesting to verify the possibility to increase ductile properties in partially relaxed samples, similarly to what observed for as-cast samples, increasing the number of cycles. In general, annealing in metallic glasses, when is conducting at temperature below T_g, should induce structural modifications toward the most stable

state (crystalline state), that implies less free-volume, and a more rigid structure with minor resilience and less ductile properties. This more fragile behaviour has been clearly observed in compression tests on well annealed samples. The idea that a partially annealed metallic glass would require higher cycles number to show plasticity improvement is sustained by the fact that the beginning structure possesses less free-volume and also less inhomogeneity.
With this aim a La-based bulk cylindrical sample was prepared. It received a 3 hours heat treatment at 100 °C to obtain a partially annealed structure. After that it experienced three subsequent treatments consisting of 25 room temperature-liquid nitrogen temperature cycles. Vickers indentations were made after each of thermal treatment. Results obtain from this measurement are shown in the following graph, Graph 3.4.2.

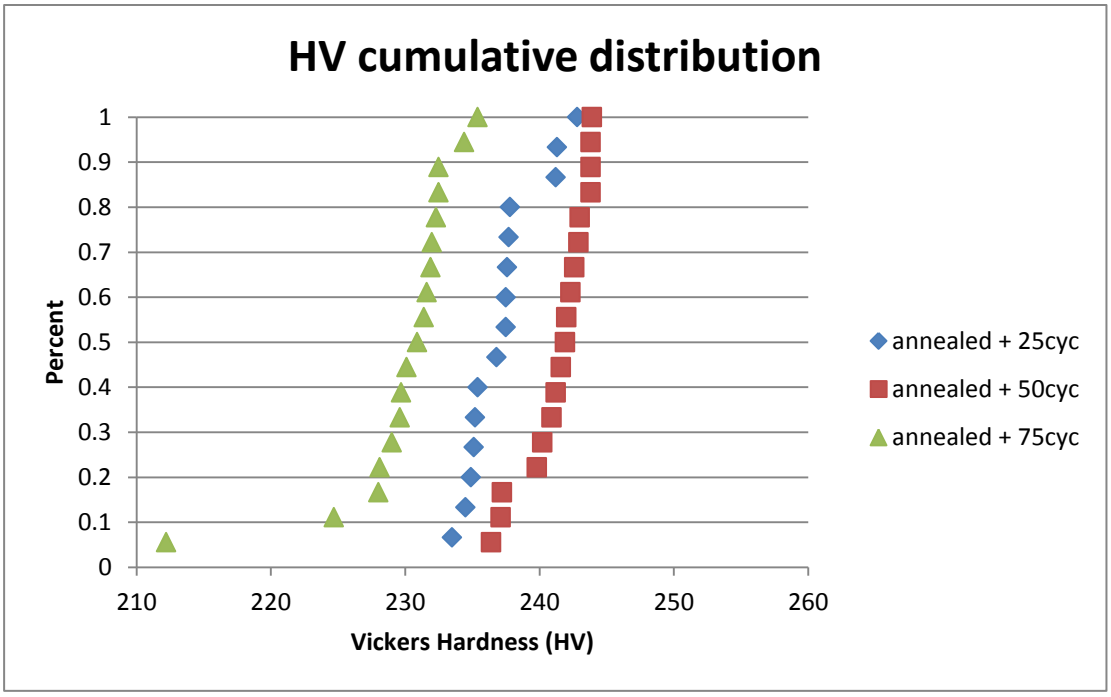

Graph 3.4.2: Vickers Hardness cumulative distribution of same surface imprints for 3 different cycles of thermal cycling treatment.

Hardness values do not show relatively big changes related to the number of cycles, an increase in hardness of a few percentage is registered after 50 cycles, in respect to 25 cycles treatment; a more significant drop (but still quite relatively small) in hardness happens after the third set of 25 cryogenic cycles.

It is peculiar to notice that after 25 cycles and 50 cycles no imprints reported pile up, any type of shear bands around the indentation were not detected. However after the last 25 cycles treatment pile up became visible. Thus, growth of total deformation zone, that implies

plasticity enhancement, is possible also for partially annealed structure and is realized by an increase in the number of cycles, in this case 75 cycles. Growth of deformed zone is easily detectable with a microscope; in the following micrographs, Picture 3.4.5 a)-c), Vickers after 25 and 50 cycles are presented.

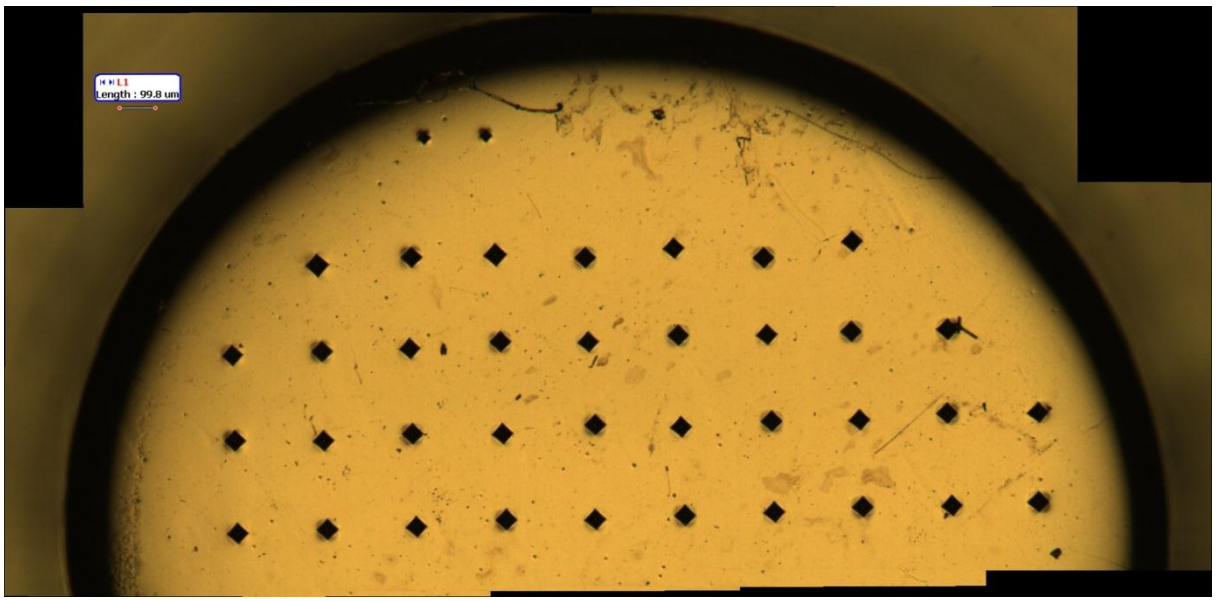

a)

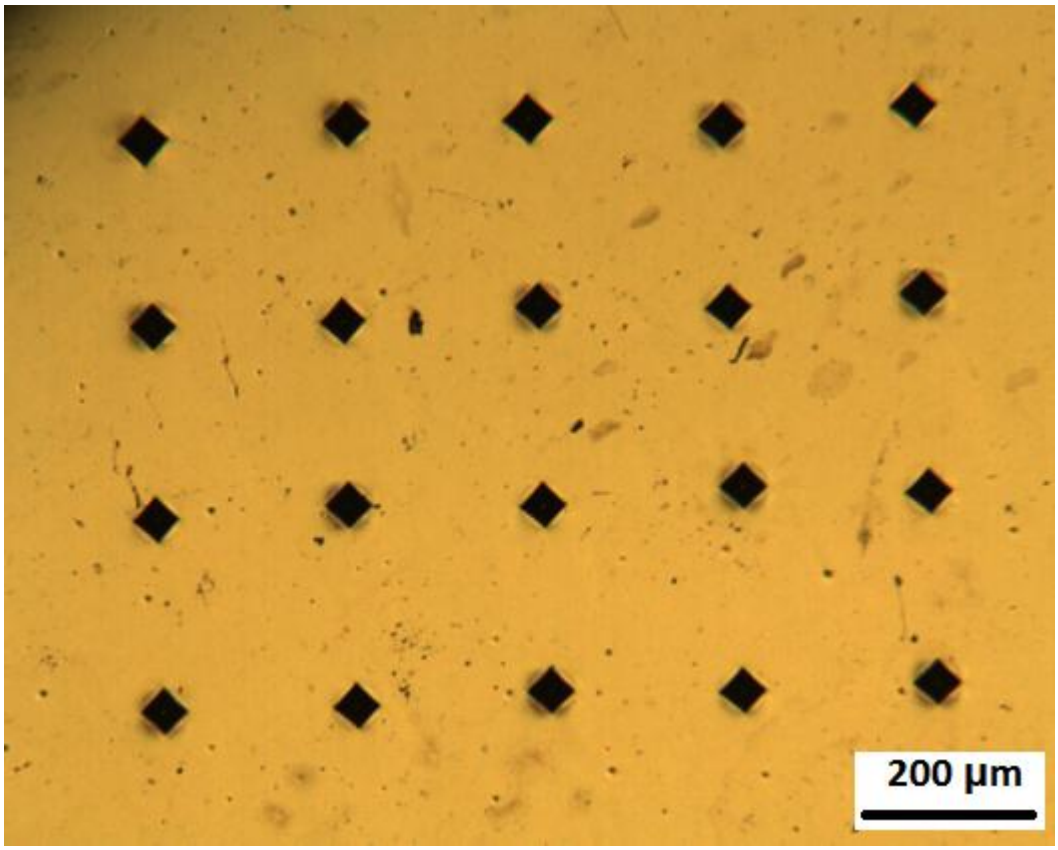

b)

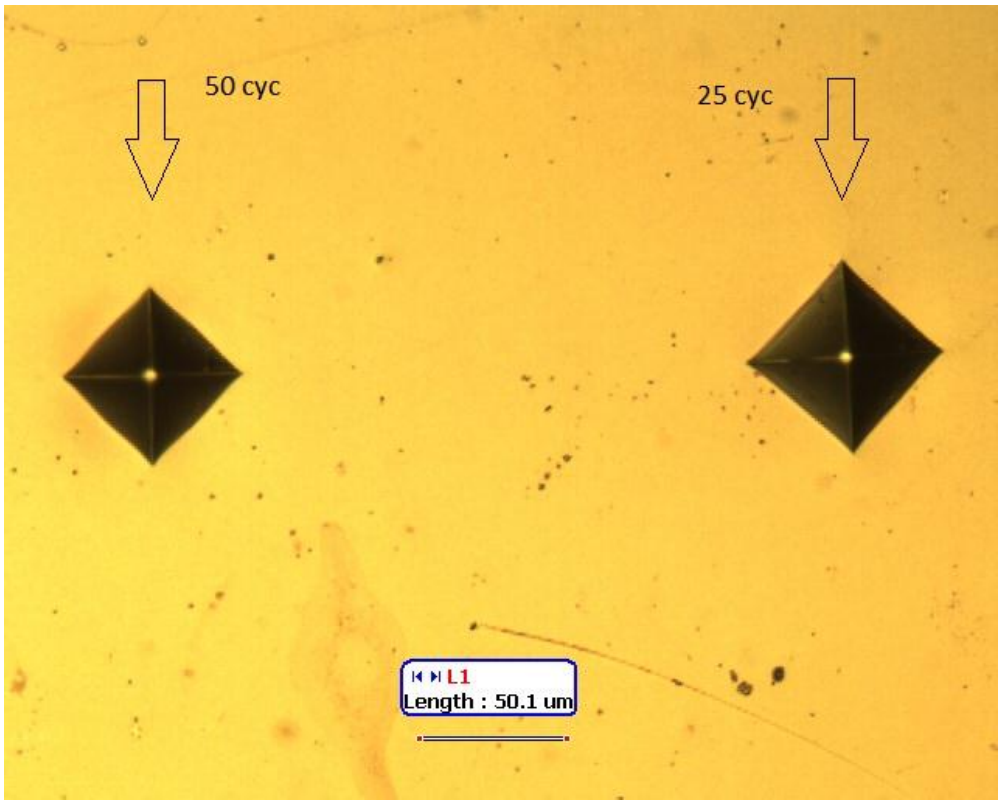

c)

Picture 3.4.5: micrograph a) is an ensemble of 50x magnification micrographs, micrograph b) 50x magnification and micrograph c) 200x magnification. a), b) and c) present micrographs of Vickers indentations made after 25 and 50 RT-liq. N_2 cycles; it is evident in particular in a) and b) constant optical difference between the two imprints series.

Direct observation, also with different magnification, highlights clear differences between Vickers imprints. From Picture3.4.5a) and Picture3.4.5b) two type of indentation can be distinguished, imprints with a bigger shadow halo around them are made after 50 cycles, while the other type, with very little shadow are Vickers indents made after 25 cycles. Deformed material by the indenter tip is distributed around the imprints, thus shadow halos represent surface curvature due to material redistribution, in other words represent the size of pile-up. From Picture3.4.5c) is also possible to note a clear shape difference between the two imprint types; 25 cycles indentations have more concave edges, which recalls sink-in mechanism, typical of fragile materials, while 50 cycles indentations have more convex edges, which are typical of more plastic materials that can distribute stresses across a larger amount of area.

To verify these optical observations AFM analysis were carried out to quantify, or at least to compare, the height and the extension of pile up zones. A 90µm x 90µm area scan was effectuated on several indents belonging to both types. 3D indentation images and

perpendicular to imprint edges height profile of pile up zones are shown in the following pictures, Picture3.4.6 and Picture3.4.7.

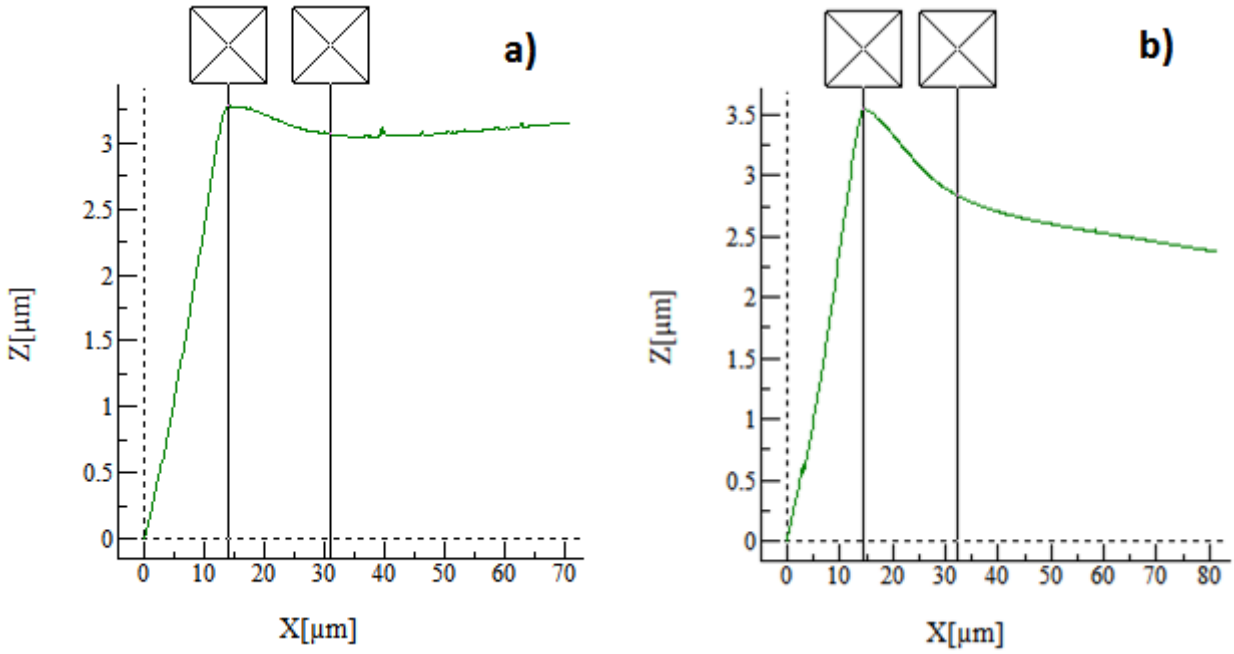

Picture 3.4.6: AFM profiles of 25 cycles and 50 cycles imprints; a) 25 cycles; b) 50 cycles. The profile analysis begins inside the imprints as the profile is crescent; when the tip reaches the surface a shoulder can be noted, between the two vertical lines; the overall profile's slope for increasing distance from the imprint is an interpolation error and not a surface true feature.

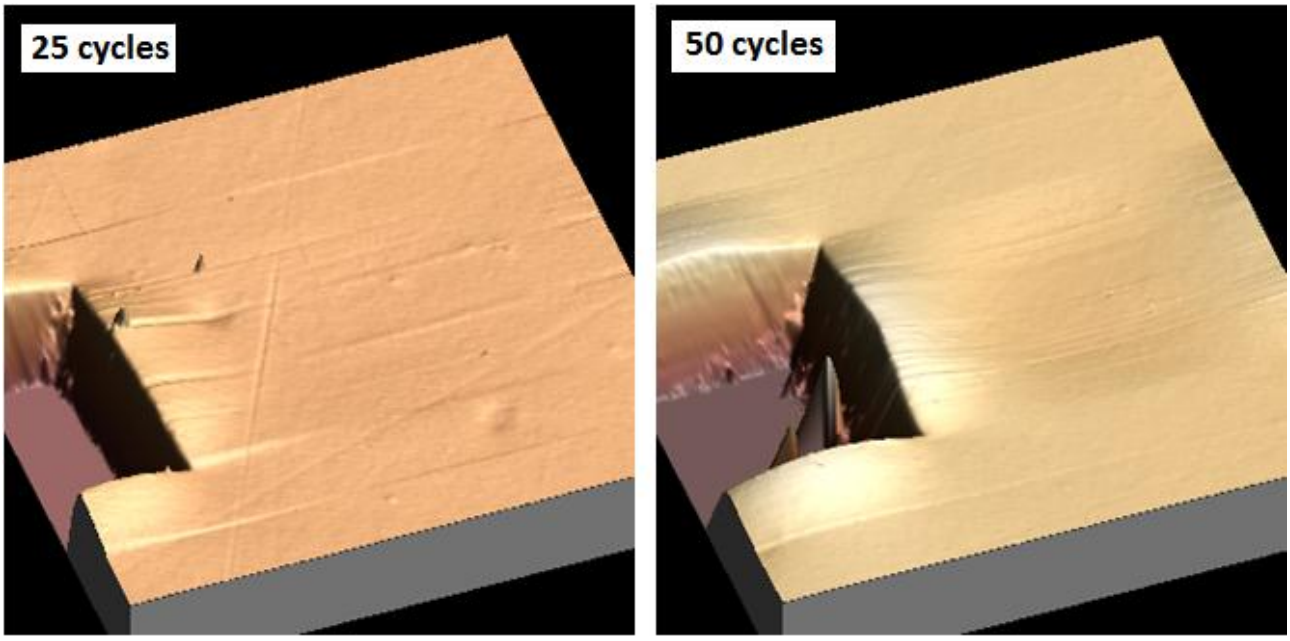

Picture 3.4.7: 3D reconstructed images of analysed imprints; left 25 cycles imprint; right 50 cycles imprint. Difference in pile-up characteristic, extension and height, are observable.

AFM is not capable of giving true values of pile-up characteristics, height and extension, because of heavy data manipulation that introduces a relatively high degree of approximation. However comparison are still possible in particular when properties difference are significant.

In the following table, Table3.4.2, are summarized AFM calculated height and extension of pile up zone:

	Height difference	**Extension lenght**
25 cyc (1)	246 nm	15.424 um
25 cyc (2)	210 nm	15.746 um
50 cyc (1)	410 nm	17.160 um
50 cyc (2)	790 nm	18.433 um

Table 3.4.2: height difference and extension length, calculated selecting significant points represented by vertical lines in Picture 3.4.6a),b), for two indents of each group.

As optical observation suggested, a clear difference emerges between 25 cycles and 50 cycles Vickers indentations; the former possess smaller pile up zone e smaller total deformation zone in respect to the latter, despite hardness values suggested opposite behaviour. Therefore the hypothesis suggesting that for a relaxed sample more thermal cycles are necessary to induce rejuvenation appears to be right. Furthermore, Vickers indentations after the last 25 cycles treatment, for an overall treatment of 75 cycles, appeared very similar to 50 cycles imprints regarding pile up and total deformation area,

interestingly they also showed shear bands pile up and a 5% decrease in hardness values. In the following pictures, Picture3.4.8 a), b), radial and semi-circular shear bands and pile-up zones are shown.

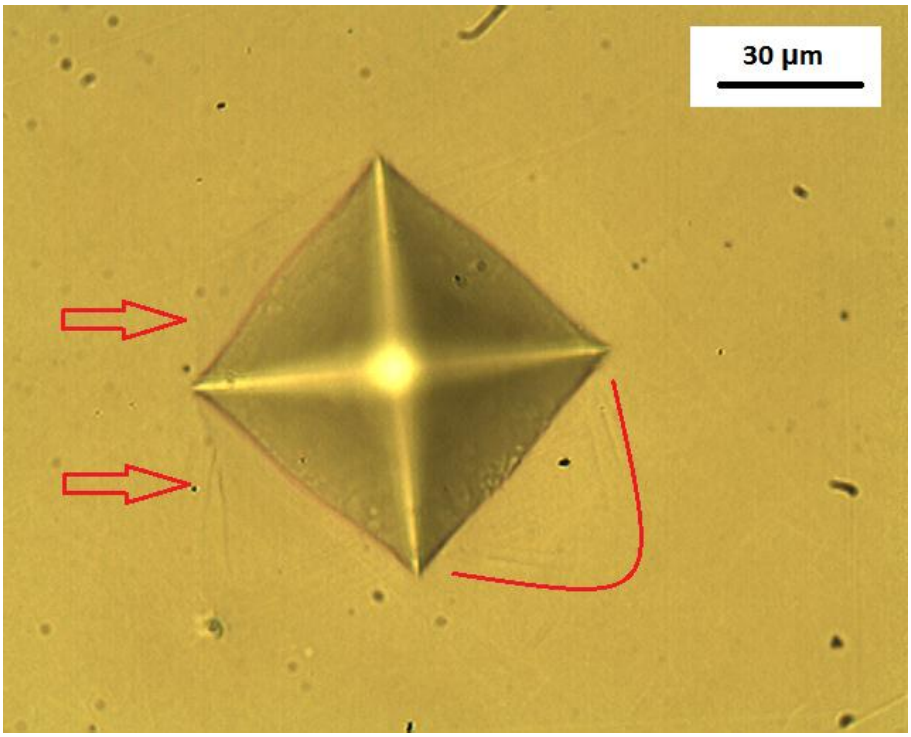

a)

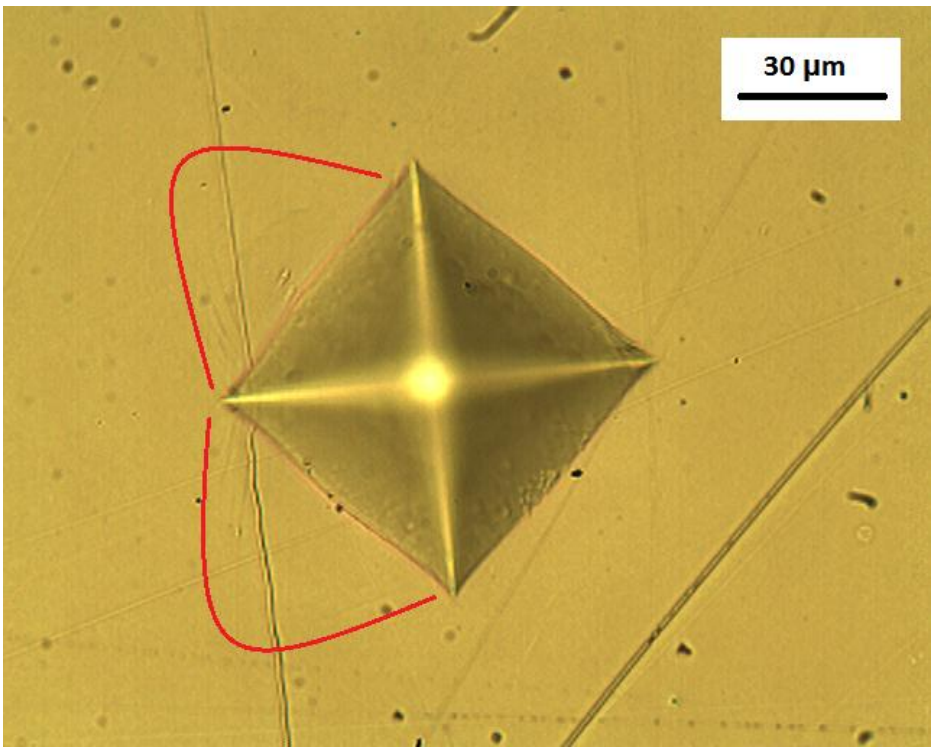

b)

Picture3.4.8: for both a) and b) magnification is 500x. Both represent Vickers imprints after 75 cycles of a partially annealed MG. Shear bands are visible; pile-up zones are highlighted with red curve lines and pointers.

3.4.3 Discussion and conclusions

From Vickers Hardness analysis a better comprehension of the cryogenic thermal cycling effect on metallic glass structure is achieved, but still some doubts and inconsistencies between tests remain, as further study is indeed needed.

1) It appears clear from this type of analysis that thermal cycling on bulk samples requires probably more cycles to be as effective as for ribbons. Moreover, it is in general not particularly effective on bulk hardness, compared to plasticity results or nanoindentation, and this could be explained considering that thermal cycling affects, introduces damage, more in the softer phase, being more disordered. Also, considering the tested volume in this case, an average effect is surely existent.

2) La-based BMG sits at the border between elastic and plastic behaviour regarding what literature reports. Appearance of shear bands is not likely in this regime. Shear bands presence near imprints edges and enlarged deformed zone is a clearly effect of the damage introduced in the structure by thermal cycling, which favour yielding of material and consequent plastic flow. Multiple shear bands are indeed nucleated reaches the surface in larger numbers as cycles number is increased. Hence, it is another proof of the rejuvenation effect of the treatment.

3) Properties modification, in particular pile-up features and shear bands density, evolves constantly with the number of cycles, proving that deductions made on nanoindentation analysis were correct. The maximum in the heat of relaxation seen in DSC results is probably unable to describe appropriately all the phenomenon features. In particular it appears notable the rejuvenation effect that is realizable in a partially annealed samples, regarding mostly its plastic flow behaviour.

4. CONCLUSIONS

In this work a study on the effect of an overall change in temperature may induce in the metallic glass structure has been carried out. This chapter wants to summarized the main points that have been explored and the conclusions that have been drawn.

First of all, it has been proved that thermal cycling between room temperature and cryogenic temperature, mostly liquid N_2 temperature, has a rejuvenation effect on the structure of La-based and Cu-Zr-based metallic glass. For rejuvenation is intended that free-volume has been introduced in the material structure and material's physical properties are more similar to the one of a more rapidly quenched glass. This appears clear from DSC heat of relaxation results.

The same analysis shows also that the rejuvenation effect is proportional to the number of cycles, at least for a small amount of cycles, and this feature is present both for ribbon samples and bulk samples. A maximum in the heat of relaxation is present at 10 cycles for ribbons and at 15 cycles for bulk. Instead, for further cycles there disagreement between DSC and other analysis.

The nature of the rejuvenation effect by thermal cycling is correlated with non-affine thermal strain. Metallic glasses are in fact believed to possess a sort of "microstructure", recent theories presented a two phases model, a softer, more free-volume phase, and a harder more ordered one. Applying a thermal change in this kind of material mechanical stresses arises at the phases interfaces. This on top of the well-known metallic glass inclination to non-affine transformations is the reason why inelastic and plastic events are expected to arise. In particular STZs activation are likely the best target for mechanical stresses.

Compression tests were conducted to study this idea. It appears that a larger plasticity and improved ductile properties derive from the thermal cycling treatment. More homogeneous plastic flow, correlated to an increase in free-volume, and an enhanced multiple shear bands deformation mechanism have been found through the analysis of samples pieces after fracture and stress-strain serrated plastic flow regime. This results seem to fit perfectly with the idea of STZs activation by thermal cycling, which would allow easier plastic onset, reducing yield pressure, and also would realize a strain delocalization, crucial for MGs, via

nucleation and propagation of a large amount of shear bands, each carrying small shear strain.

Nanoindentation and also Vickers indentation results however show some discrepancies between analysis. Both from DSC and compression test the magnitude order of property change induced by thermal cycling appears significant but, only from DSC, it shows a falling behaviour for further number of cycles. Indentation results instead show a much smaller change, in significant properties such as yield pressure and hardness, but still rejuvenation was detected. This is probably due to some averaging effect or simply to less technique sensitivity.

Moreover, indentation proved that rejuvenation proceeding with the number of cycles. In fact thermal cycling induces damage in the structure, STZs activation and free-volume generation; possibly relaxation mechanism happens for further stimulation but structure modifications remain. This rejuvenation feature has been clearly captured by nanoindentation and Vickers hardness measurements.

Nanoindentation also spotted a key characteristic regarding number of cycles and rejuvenation: increment of first pop-in size with a decrease in the first yield pressure. This behaviour likely describe the nature of the thermal cycling effect, i.e. STZs activation and generation.

5. REFERENCES

[1] Y. Shao, F. Spaepen, and D. Turnbull, “An analysis of the formation of bulk amorphous silicon from the melt,” Metall. Mater. Trans. A, 29, 7, 1825–1828, 1998

[2] K. F. Kelton, and A. L. Greer, Nucleation in condensed matter, Oxford: Elsevier, 532-537, 2010

[3] A.L. Greer, Metallic glasses, Physical Metallurgy, 5th Edition, 2014

[4] S. Singh, M. D. Ediger, and J. J. de Pablo, “Ultrastable glasses from in silico vapour deposition.,” Nat. Mater., 12, 2, 139–44, 2013

[5] C. A. Angell, “Formation of glasses from liquids and biopolymers.,” Science, 267, 5206, 1924–35, 1995

[6] R. Busch, J. Schroers, and W. H. Wang, “Thermodynamics and Kinetics of Bulk Metallic Glass,” MRS Bull., 32, 08, 620–623, 2007

[7] W. Kauzmann, “The Nature of the Glassy State and the Behavior of Liquids at Low Temperatures.,” Chem. Rev., 43, 2, 219–256, 1948

[8] C. Suryanarayana and A. Inoue, Bulk Metallic Glasses. London: CRC Press., 2011

[9] D. Turnbull, “under what conditions can a glass be formed?” Contemp. Phys. 10, 473-488, 1969

[10] Y.Q. Cheng, E. Ma, “Atomic-level structure and structure–property relationship in metallic glasses”, Progress in Materials Science, 56, 379–473, 2011

[11] A. Inoue, “Stabilization of metallic supercooled liquid and bulk amorphous alloy” Acta Mater. 48, 279-306, 2000

[12] A. J. Drehman, “Bulk formation of a metallic glass: Pd40Ni40P20,” Appl. Phys. Lett., 41, 8,716, 1982

[13] A. Inoue, Y. Shinohara, Y. Yokoyama, and T. Masumoto, “Solidification analyses of bulky Zr60Al10Cu15Pd5 glass produced by casting into wedge-shape copper mold,” Mater. Trans. - JIM,36,10, 1276–1281, 1995

[14] A. Inoue and T. Zhang, “Fabrication of bulky Zr-based glassy alloys by suction casting into copper mold,” Mater. Trans., 1995

[15] R. Lynch, R. Olley, and P. Gallagher, “Squeeze Casting of Brass and Bronze,” TRANS AFS, 1975

[16] A. I. Taub and F. Spaepen, “Isoconfigurational flow of amorphous Pd82Si18,” Scr. Metall., vol. 13, no. 3, pp. 195–198, Mar. 1979

[17] T. Egami, S.J.L. Billinge, “Underneath the Bragg peaks: Structural analysis of complex materials”, Amsterdam, 2012

[18] T. Egami, “Structural study by energy dispersive X-ray diffreaction”, Glassy Metals I., Springer, Berlin, 1981

[19] C.N.J. Wagner, “Experimental determination of atomic scale strcture of amorphous alloys by scattering experiments”, Amorphous metallic alloys, Butterworths, London, 1983

[20] J.F. Sadoc, J. Dixmier, “Structural investigation of amorphous CoP and NiP alloys by combined X-ray and neutron scattering” Mater. Sci. Eng. , 1976

[21] P. Lamparter, W. Sperl, “Atomic structure of amorphous metallic $Ni_{81}P_{19}$” , Z. Naturforsch, 1982

[22] L. C. Chen and F. Spaepen, “Analysis of calorimetric measurements of grain growth,” J. Appl. Phys., vol. 69, no. 2, p. 679, Jan. 1991.

[23] J. Bernal, “The Bakerian lecture, 1962. The structure of liquids,” Proc. R. Soc. London. Ser. A, 1964.

[24] L.-L. Shi, J. Xu, and E. Ma, “Alloy compositions of metallic glasses and eutectics from an idealized structural model,” Acta Mater., vol. 56, no. 14, pp. 3613–3621, Aug. 2008.

[25] D. B. Miracle, W. S. Sanders, and O. N. Senkov, “The influence of efficient atomic packing on the constitution of metallic glasses,” Philos. Mag., vol. 83, no. 20, pp. 2409–2428, Jul. 2003.

[26] D. Miracle, “A structural model for metallic glasses.,” Nat. Mater., vol. 3, no. 10, pp. 697–702, Oct. 2004.

[27] F. C. Frank, “Supercooling of liquids,” Proc. R. Soc. Lond. A. Math. Phys. Sci., pp. 43–46, 1952.

[28] Y. Q. Cheng, E. Ma, and H. W. Sheng, “Alloying strongly influences the structure, dynamics, and glass forming ability of metallic supercooled liquids,” Appl. Phys. Lett., vol. 93, no. 11, p. 111913, Sep. 2008.

[29] H.W. Sheng, W.K. Luo, F.M. Alamgir, F.M. Bai, E. Ma, “Atomic packing and short-to-medium range order in metallic glasses”, Nature, 2006.

[30] T. Ichitsubo, S. Hosokawa, K. Matsuda, E. Matsubara, N. Nishiyama, S. Tsutsui, and A. Q. R. Baron, “Nanoscale elastic inhomogeneity of a Pd-based metallic glass: Sound velocity from ultrasonic and inelastic x-ray scattering experiments,” Phys. Rev. B, vol. 76, no. 14, p. 140201, 2007.

[31] H. Wagner, D. Bedorf, S. Küchemann, M. Schwabe, B. Zhang, W. Arnold, and K. Samwer, “Local elastic properties of a metallic glass,” Nat. Mater., vol. 10, no. 6, pp. 439–442, Jun. 2011.

[32] T. Ichitsubo, H. Kato, E. Matsubara, S. Biwa, S. Hosokawa, K. Matsuda, H. Uchiyama, A.Q.R. Baron “Static heterogeneity in metallic glasses and its correlation to physical properties”, Journal of Non-Crystalline Solids 357, 494–500, 2011

[33] J. G. Wang, D. Q. Zhao,M. X. Pan, C. H. Shek, W. H. Wang “Mechanical heterogeneity and mechanism of plasticity in metallic glasses”, Applied Physics Letters 94, 2009

[34] W. Dmowski, C. Fana, M.L. Morrison, P.K. Liaw, T. Egami, “Structural changes in bulk metallic glass after annealing below the glass transition temperature”, Mater. Sci. Eng. 2007

[35] E. H. Chason and T. Mizoguchi, “Structural Relaxation and Interdiffusion in Amorphous Fe-Ti Compositionally Modulated Films,” in MRS Proceedings, 1986, vol. 80, p. 61.

[37] A. L. Greer and J. A. Leake, “Structural relaxation and crossover effect in a metallic glass,” J. Non. Cryst. Solids, vol. 33, no. 2, pp. 291–297, Jun. 1979

[38] M. F. Ashby, “Materials selection in mechanical design,” MRS Bull., vol. 30, p. 995, 2005.

[39] M. Ashby and A. L. Greer, “Metallic glasses as structural materials,” Scr. Mater., vol. 54, no. 3, pp. 321–326, Feb. 2006.

[40] Thomas H.C., “Mechanical Behavior of Materials” (2nd edition), 2000, McGraw-Hill, New York.

[41] Langer, J.S., “Shear-transformation-zone theory of viscosity, diffusion, and stretched exponential relaxation in amorphous solids”, Physical Review E, 2012, 85: 051507.

[42] Packard, C.E., Homer, E.R., Al-Aqeeli, N. and Schuh, C.A., “Cyclic hardening of metallic glasses under Hertzian contacts: Experiments and STZ dynamics simulations”, Philosophical Magazine, 2010, 90: p.1373-1390.

[43] A. S. Argon, “Plastic deformation in metallic glasses” , Acta Metall., vol. 27, no. 1, pp. 47–58, Jan. 1979.

[44] A.L. Greer, Y.Q. Cheng, E. Ma “Shear bands in metallic glasses” , Materials Science and Engineering 74 71-132, 2013

[45] D. Pan, A. Inoue, T. Sakurai, and M. W. Chen, “Experimental characterization of shear transformation
zones for plastic flow of bulk metallic glasses” , PNAS September 30, 2008 vol. 105 no. 39 14769–14772

[46] F. Spaepen, “A microscopic mechanism for steady state inhomogeneous flow in metallic glasses”, Acta Metallurgica, 1977, 25, 407–415.

[47] D. Klaumu¨nzer, R. Maaß, F. H. D. Torre, and J. F. Loffler, “Temperature-dependent shear band dynamics in a Zr-based bulk metallic glass,” Appl. Phys. Lett., vol. 96, no. 6, p. 061901, Feb. 2010.

[48] Wright, W.J., R. Saha, and W.D. Nix (2001). Deformation mechanisms of the Zr40Ti14Ni10Cu12Be24 bulk metallic glass. *Mater. Trans*. 42: 642–649.

[49] S. F. Pugh, “XCII. Relations between the elastic moduli and the plastic properties of polycrystalline pure metals,” Philos. Mag., vol. 45, no. 367, pp. 823–843, 1954.

[50] J. J. Lewandowski, W. H. Wang, and a. L. Greer, “Intrinsic plasticity or brittleness of metallic glasses,” Philos. Mag. Lett., vol. 85, no. 2, pp. 77–87, Feb. 2005.

[51] K. Geels, “Metallographic and Materialographic Specimen Preparation, Light Microscopy, Image Analysis and Hardness Testing”, ASTM International, 2007.

[52] W. C. Oliver and G. M. Pharr, “An improved technique for determining hardness and elastic modulus using load and displacement sensing indentation experiments,” J. Mater. Res., vol. 7, no. 06, pp. 1564–1583, 1992.

[53] W. H. Wang: “The elastic properties, elastic models and elastic perspectives of metallic glasses”, Prog. Mater. Sci., 2012, 57, 487−656.7

[54] H. Kato, H.-S. Chen, A. Inoue, “Relationship between thermal expansion coefficient and glass transition temperature in metallic glass” , Scrip. Mat. 58 1106-1109, 2008

[55] Chen ZhenHua, Zhang LiKe, Liu JiZi, Chen Ding, “Cryogenic treatment induced hardening for Cu-Zr-Ag-Al bulk metallic glasses”, Science China Technological Sciences, 2013

[56] A. Concustell, N. Mattern, H. Wendrock, A.L Greer, Scripta Materialia 56, 85 2007

[57] K. M. Flores, Biraja P. Kanungo, Stephen C. Glade, Palakkal Asoka-Kumar, “Characterization of plasticity-induced structural changes in a Zr-based bulk metallic glass using positron annihilation spectroscopy”, Journal of Non-Crystalline Solids 353 (2007) 1201–1207

[58] Vempati U., Valavala P., Falk M., Almer J. and Hufnagel T. “Length-scale dependence of elastic strain from scattering measurements in metallic glasses. Phys. rev. b 85, 214201 (2012)

[59] F.O. Méar , B. Lenk, Y. Zhang, A.L. Greer “Structural relaxation in a heavily cold-worked metallic glass” Scripta Materialia Volume 59, Issue 12, December 2008, 1243–1246.

[60] Y. H. Liu, G. Wang, R. J. Wang, D. Q. Zhao, M. X. Pan and W. H. Wang: ‘Super plastic bulk metallic glasses at room temperature’, *Science,* 2007, **315**, 1385–1388

[61] Y. Q. Cheng, Z. Han, Y. Li and E. Ma: 'Cold versus hot shear banding in bulk metallic glass', *Phys. Rev. B*, 2009, **80**, 134115.

[62] C. A. Schuh, A. C. Lund and T. G. Nieh: 'New regime of homogeneous flow in the deformation map of metallic glasses: elevated temperature nanoindentation experiments and mechanistic modelling', *Acta Mater.*, 2004, **52**, 5879–5891.

[63] S. Jana, U. Ramamurty, K. Chattopadhyay, Y. Kawamura "Subsurface deformation during vickers indentation of bulk metallic glasses", Materials Science and Engineering: Volumes 375–377, July 2004, Pages 1191–1195

[64] V. Keryvin ," Indentation of bulk metallic glasses: relationships between shear bands observed around the prints and hardness" Acta Materialia Volume 55, Issue 8, May 2007, Pages 2565–2578

6. RIASSUNTO

6.1 Introduzione

6.1.1 Fondamenti dello stato vetroso

Dal 1950, grazie allo sviluppo di tecniche di raffreddamento rapido, è emersa una nuova classe di leghe, i vetri metallici, con la caratteristica distintiva della mancanza di un ordine atomico a lungo raggio, cosa invece presente nei materiali cristallini.

Un vetro metallico presenta la struttura di un liquido, in combinazione con la resistenza alla deformazione tipica di un solido. È possibile ottenerlo grazie ad un raffreddamento sufficientemente elevato ad evitare la cristallizzazione.

Figura 6.1.1. [3] mostra schematicamente la dipendenza dalla temperatura del volume specifico del liquido, *v*, e dell'entalpia, *h*, a pressione costante. T_m rappresenta la temperatura di fusione, mentre T_{gb} e T_{ga} sono rispettivamente due diverse temperature di transizione vetrosa, rispettivamente per velocità di raffreddamento più o meno elevate.

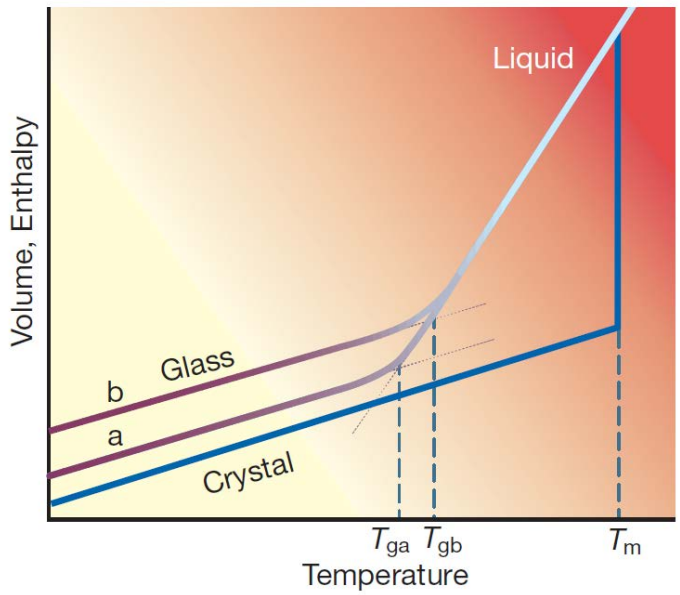

Figura 6.1.1 : Rappresentazione del volume specifico, *v*, ed entalpia specifica, *H*, in funzione della temperatura, per due diversi stati vetrosi e il corrispettivo stato cristallino, a pressione costante.

La temperatura di transizione vetrosa, T_g, è la temperatura che segna il passaggio dal liquido sottoraffreddato sotto T_m ad il vetro. Evidenze sperimentali per diversi materiali hanno

dimostrato che tale transizione avviene alla temperatura alla quale la viscosità, η, raggiunge il valore di 10^(12)*Pa*s*. Questo valore di viscosità rappresenta un limite cinetico sotto il quale il moto atomico è così lento che non vi sono ulteriori modifiche configurazionali con il procedere del raffreddamento.
È importante rilevare che T_g non è una temperatura termodinamicamente definita ed è determinata esclusivamente dalla cinetica. Per la medesima composizione vetrosa sono possibili diverse T_g e conseguentemente diversi stati vetrosi.

6.1.2 Struttura dei vetri metallici

In un vetro metallico non esiste un reticolo cristallino relativamente al quale difetti, come bordi grano o dislocazioni, possono essere definiti. Quindi una struttura vetrosa manca di periodicità e ordine a lungo raggio. Tuttavia ciò non implica che non vi sia alcun ordine e che un vetro metallico sia semplicemente un insieme casuale di atomi.
La presenza di un certo grado di ordine è coerente con lo stato di bassa entropia che può caratterizzare un vetro metallico e *short-range order* e *medium-range order* sono termini tipicamente usati per descrivere il livello di ordine che esiste in tali materiali.
Diversi modelli strutturali sono stati elaborati al fine di prevedere e spiegare l'ordine atomico di un vetro metallico.
Recentemente è diventato sempre più evidente che i vetri metallici presentano delle inomogeneità su scale differenti, a livello nanometrico e micrometrico, probabilmente ereditate dal liquido. Ichitsubo et al. [30] hanno proposto un modello strutturale rappresentante i vetri metallici come un mix di due diverse regioni: regioni fortemente legate e regioni debolmente legate, caratterizzate da proprietà meccaniche differenti.

6.1.3 Proprietà dei vetri metallici e meccanismo di deformazione

Meccanicamente i vetri metallici presentano proprietà interessanti, alta tensione di snervamento e basso modulo elastico, rispetto alle loro controparti cristalline. Questo è dovuto alla mancanza di difetti strutturali mobili come le dislocazioni. Queste caratteristiche

suggeriscono applicazioni per tali materiali che sfruttano la loro capacità di accumulare energia elastica.

Altri aspetti interessanti che hanno permesso la diffusione dei vetri metallici sono le loro interessanti proprietà magnetiche, alta permeabilità e bassa coercitività magnetica.

Un aspetto critico è rappresentato dalle caratteristiche di duttilità dei vetri metallici, poiché fondamentali nella applicazioni strutturali. Sebbene alcune composizioni presentino dei valori di tenacità a frattura, K_c , comparabili a quelle dei metalli, e quindi non sono certamente fragili, i vetri metallici non sono generalmente considerati adatti ad applicazioni meccaniche. Ciò è generalmente dovuto all'instaurarsi di una instabilità nella deformazione che porta a rottura prematura e fragile. Al contrario dei metalli che posseggono la capacità di incrudirsi i vetri metallici non dispongono di mezzi simili e al contrario la loro deformazione massiva è caratterizzata da *work-softening* , per cui la deformazione si localizza e porta velocemente a frattura. Il motivo di questo comportamento è da ricercarsi principalmente nella struttura atomica.

Come suggerito da Argon [44], la deformazione plastica nei vetri metallici al di sotto della loro temperatura di transizione vetrosa, avviene per ri-arrangiamenti locali di atomi in regioni che possono variare da decine a centinaia di atomi. Queste aree sferoidali sono chiamate *shear transformation zones* (STZ). In contrasto con dislocazioni, che sono difetti mobili, tali *shear transformation zones* non sono così chiaramente definite e osservabili al microscopio, e operano come entità immobili che non migrano.
Nel modello proposto, quando, ad una *shear transformation zone* è applicata una tensione, essa si "attiva", il volume in eccesso in essa condensa, ma questo cambiamento impone un nuovo campo di deformazione al materiale circostante che ha come conseguenza la formazione di nuove STZs, di nuovi difetti, cioè un indebolimento maggiore della zona circostante, Figura 6.1.2.
Da un punto di vista macroscopico, le *shear transformation zones* vicine fra loro possono collegarsi fino a formare una *shear band* lungo la quale il materiale è più debole e dove in effetti si concentra la successiva deformazione di taglio.
Lungo la direzione di massima sollecitazione di taglio, una *shear band* dominante può apparire e spesso portare ad instabilità e al rapido cedimento del materiale.
Questo processo è rappresentato nella Figura 6.1.2.

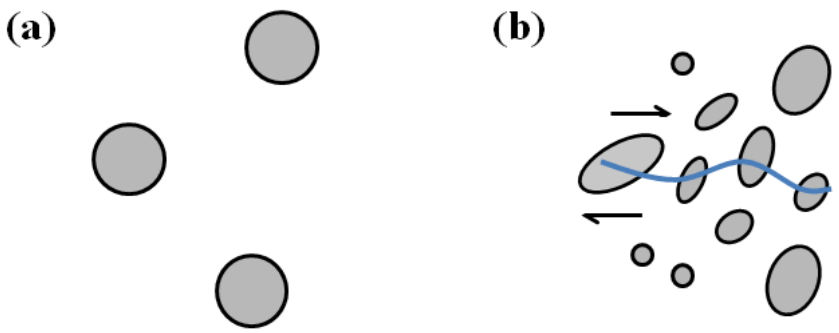

Figura 6.1.2: I cerchi grigi rappresentano le s*hear transformation zones*.Figura (a) mostra la condizione senza stress, mentre figura (b) mostra la struttura delle *shear transformation zones* sotto sforzo di taglio (frecce nere). L'applicazione di uno sforzo di taglio su una *shear transformation zone* ne modifica la configurazione atomica. Le *shear transformation zones* esistenti tendono a capovolgersi e formano nuove *shear transformation zones*. Il collegamento delle *shear transformation zones* forma una *shear band* (linea blu)

Possiamo definire lo *shear banding* come una forma di instabilità plastica basata sulla localizzazione delle deformazioni di taglio in una banda relativamente sottile (*shear band*).
In tensione, il *work-softening* dovuto all'aumento volume libero che caratterizza la *shear band*, porta generalmente ad un cedimento catastrofico del materiale, con zero duttilità. In compressione il meccanismo opera differentemente attraverso tre stadi: nucleazione delle *shear bands,* propagazione delle *shear bands,* scorrimento delle *shear bands* e deformazioni plastiche anche significative sono state osservate.

6.2 Tecniche Sperimentali

I dati sperimentali presentati sono il risultato dell'attività di ricerca condotta presso il dipartimento di Scienza dei Materiali e Metallurgia dell'Università di Cambridge.

6.2.1 Microscopi

Durante l'attività sperimentale ci si è avvalsi di differenti microscopi, tra cui quello ottico, utilizzato per valutare la qualità delle superfici lucidate e le caratteristiche delle shear bands.
In diverse occasioni è stato utilizzato anche un microscopio elettronico a scansione Philips XL30 SFEG SEM. Un microscopio elettronico a scansione è un particolare tipo di microscopio che utilizza un fascio elettronico focalizzato, con lunghezze d'onda molto più corte rispetto

alla luce visibile, così da avere un'immagine del campione con risoluzione più elevata rispetto ai sistemi ottici.
È stato anche utilizzato un microscopio a forza atomica Veeco Dimension 3100 AFM per valutare la superficie di alcuni campioni.
Il microscopio a forza atomica è costituito da una microleva (cantilever) alla cui estremità è montata una punta acuminata (tip), che presenta un raggio di curvatura dell'ordine dei nanometri.
La punta investigatrice viene collocata sulla superficie del campione da scansionare. Le forze di van der Waals che agiscono tra la punta ed il campione provocano una deflessione della microleva che viene misurata utilizzando un punto laser riflesso dalla sommità di essa.

6.2.2 Prove di indentazione

Test di microdurezza Vickers sono stati utilizzati per valutare le proprietà meccaniche di alcuni campioni. La durezza Vickers (HV) del materiale, è definita attraverso la pressione di contatto di un carico applicato, *P,* su un'area di contatto, A_c: $H=P/A_c$
In base alle caratteristiche geometriche del penetratore Vickers, l'area di contatto può essere calcolata attraverso il valore medio delle lunghezze delle diagonali dell'impronta lasciata dalla punta sulla superficie del campione.
I risultati qui presentati sono stati ottenuti con una macchina per prove di durezza Vickers Mitutoyo MVK-H2.

I test di nanoindentazione sono stati utilizzati per valutare il cambiamento delle proprietà meccaniche dei campioni prima e dopo particolari trattamenti.
In tali prove si utilizzano piccoli carichi con punte di dimensioni ridotte, registrando il carico e la profondità di penetrazione istante per istante durante ogni test. Il risultato è la curva carico-penetrazione.
Dalla profondità di penetrazione e dalla geometria della punta è possibile ottenere una misura indiretta della superficie di contatto in ogni istante.
Da ciò segue una stima dell'area di contatto e conseguentemente della durezza, *H*, del materiale.

È possibile inoltre calcolare il modulo del materiale tramite la pendenza della curva nella fase di scarico. La forma della curva carico-penetrazione è una ricca fonte di informazioni aggiuntive oltre al modulo e alla durezza del campione: essa permette anche l'identificazione di eventi non lineari come trasformazioni di fase, cricche e *shear bands*.

Per i vetri metallici la transizione da regime elastico a quello plastico è definita da una discontinuità di tale curva, detta *pop-in event*. Questa transizione è associata al punto in cui una *shear band* nuclea e si propaga ed è caratteristica del materiale e del suo stato.

È possibile quindi andare a calcolare la tensione di snervamento in corrispondenza del primo pop-in individuato nella curva carico-penetrazione per ciascun test effettuato.

Tutti i dati relativi ai test di nanoindentazione presentati sono stati ottenuti con un indentatore MTS XP con punta sferica di diamante di 8.074μm di diametro.

6.2.3 Prova di compressione

Nel lavoro sperimentale qui presentato alcuni campioni sono stati testati a compressione al fine di valutarne la duttilità, tramite la deformazione ingegneristica al punto di rottura, ε_f.

Le prove di compressione sono state eseguite utilizzando un tester Tinius Olsen H25-S UTM, con capacità massima di 25 kN (5000lbf).

6.3 Risultati Sperimentali

Vetri metallici di tre composizioni diverse sono stati studiati: $La_{55}Al_{25}Ni_{20}$, $La_{55}Al_{35}Ni_{10}$, $Cu_{46}Zr_{46}Al_7Gd_1$. Il primo è stato fornito solo sotto forma di nastri sottili (*ribbon*), gli altri due invece sono stati analizzati in forma massiva (*bulk*). Cicli termici in vario numero tra temperatura ambiente e temperature criogeniche sono stati condotti su questi campioni, in Figura 6.3.1 si riporta un esempio schematico del trattamento termico applicato. I campioni sono stati lasciati a ciascuna temperatura per 1 minuto. Lo scopo di questi trattamenti è osservare se in relazione alle inomogeneità presenti nella struttura dei vetri metallici è possibile indurre un aumento del volume libero e perciò un ringiovanimento della struttura.

Per tale motivo è stato analizzato lo spettro di rilassamento con tecnica DSC e il calore di rilassamento rilasciato è stato misurato.

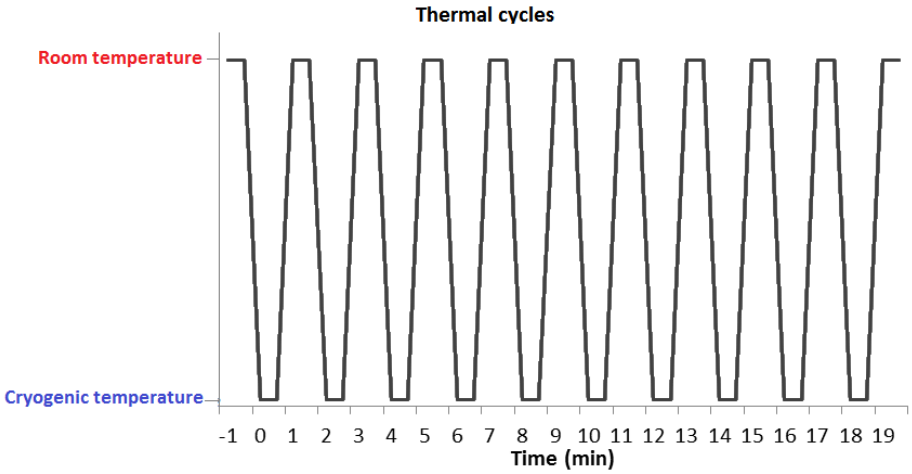

Figura 6.3.1: rappresentazione schematica di 10 cicli termici.

6.3.1 Analisi DSC

Misure di calorimetria differenziale sono state condotte su nastri di vetro metallico di $La_{55}Al_{25}Ni_{20}$ e su dischi sottili tagliati da barre di $La_{55}Al_{35}Ni_{10}$. Sono state studiate l'effetto della temperatura criogenica del ciclo termico, il tempo di permanenza alla temperatura criogenica e il numero di cicli tra le due temperature.

6.3.1.1 Effetto della temperatura criogenica

Tre temperature criogeniche sono state valutate, 4K (elio liquido), 77K (azoto liquido) e 195K (ghiaccio secco). Nella misura calorimetrica è stata condotta imponendo una rampa di riscaldamento a velocità costante, pari a 10 K/min . A raffreddamento completato una seconda rampa è eseguita, in questo caso è fatta a cristallizzazione avvenuta, che viene successivamente sottratta alla prima scansione e che funge quindi da riferimento per il calcolo del calore di rilassamento. Tutte le analisi eseguite in questa esperienza sono state effettuate seguendo questo procedura.

Nel Grafico 6.3.1.1 sono riportati gli spettri DSC relativi a campioni as-cast, trattati con azoto liquido e trattati con elio liquido:

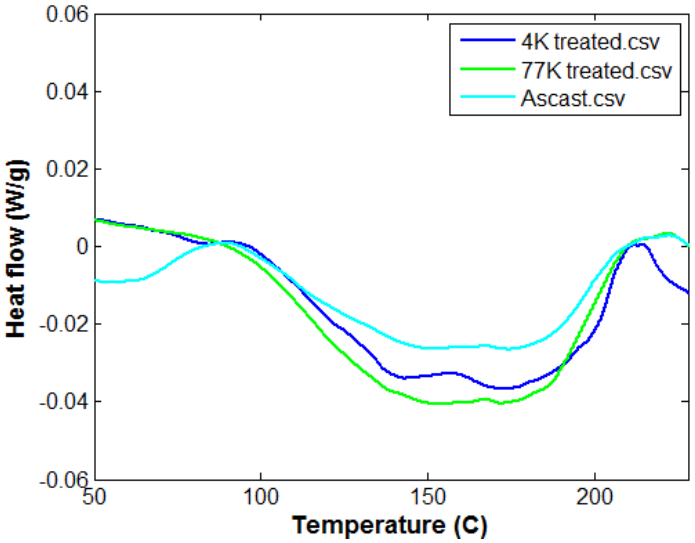

Grafico 6.3.1.1: spettri di rilassamento di tre campioni: as-cast (nessun trattamento), sottoposto a ciclo termico con azoto liquido e sottoposto a ciclo termico con elio liquido. Per questi ultimi due si evidenzia un aumento del calore di rilassamento.

Nella tabella seguente, Tabella 6.3.1.1, i valori del calore di rilassamento sono riportati:

	As-cast	21 cicli termici in azoto liquido	13 cicli termici in elio liquido
Calore di rilassamento (J/mol)	1827.2	3100.0	2398.6

Tabella 6.3.1.1: calore di rilassamento di tre campioni: as-cast (nessun trattamento), sottoposto a ciclo termico con azoto liquido e sottoposto a ciclo termico con elio liquido.

Si può notare che il calore rilasciato per rilassamento termico è sensibilmente superiore per i campioni che hanno subito il trattamento termico. Un effetto di ringiovanimento si è perciò realizzato. Nonostante gli stress meccanici che dovrebbero generarsi per effetto della presenza di una microstruttura nel vetro metallico dovrebbero essere proporzionali alla differenza di temperatura imposta dal ciclo termico, si constata che la temperature dell'azoto liquido risulta più efficace di quella dell'elio. Cicli termici tra temperatura ambiente e 195K non hanno determinato un significativo cambiamento del calore di rilassamento rispetto allo stato non trattato termicamente e perciò non vengono mostrati in questo riassunto.

6.3.1.2 Effetto del numero di cicli su ribbon e bulk

Data la differenza del numero di cicli tra campioni trattati con elio e azoto, questo parametro è stato studiato più approfonditamente, sia su campioni *ribbon* che *bulk*.

I cicli termici sono stati effettuati tra temperatura ambiente e 77K, e l'effetto di 5, 10, 15, 20 e 25 è stato studiato sia per i nastri che per i dischi. In questo caso le misure calorimetriche sono state eseguite con un riscaldamento a 20K/min. Nei Grafici 6.3.1.2 e 6.3.1.3 vengono riportati rispettivamente gli spettri di rilassamento dei *ribbon* per i diversi numeri di cicli termici e il valore del calore di rilassamento in funzione del numero di cicli.

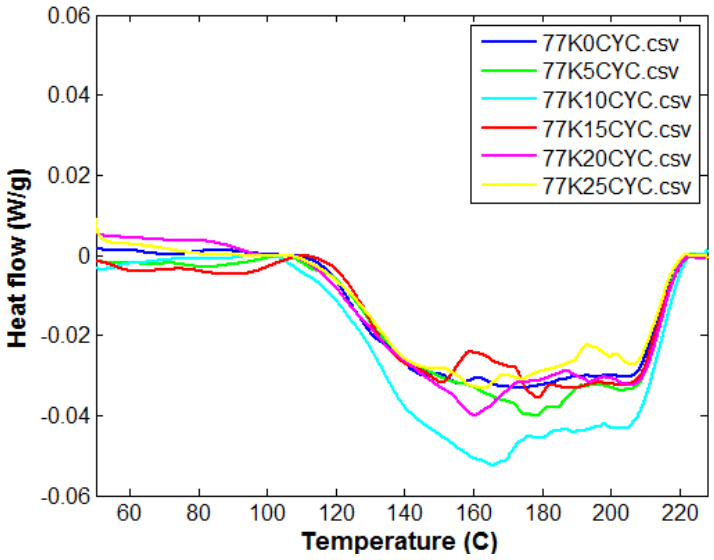

Grafico 5.3.1.2: spettri di rilassamento per diversi numeri di cicli termici.

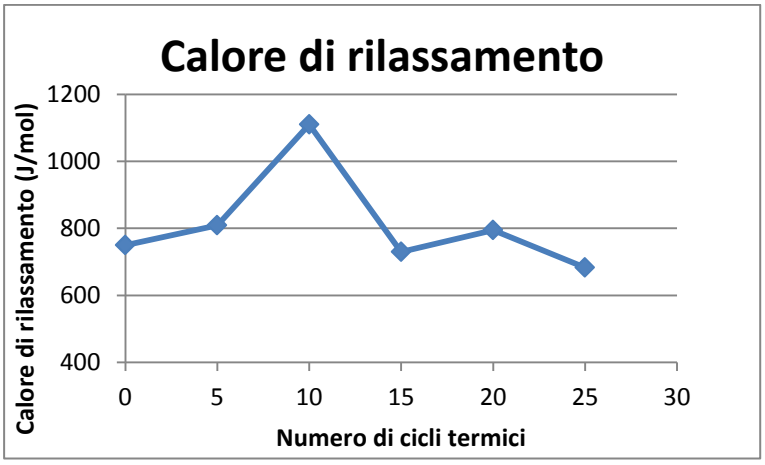

Grafico 6.3.1.3: variazione del calore di rilassamento in funzione del numero di cicli termici

Per questa tipologia di vetro metallico si evidenzia la presenza di un andamento crescente per pochi cicli termici, culminante con un massimo a 10 cicli, e un successivo andamento decrescente per ulteriori cicli.

Nel Grafico 6.3.1.4 viene invece riportato l'andamento del calore di rilassamento dei dischi di vetro metallico tagliati da barre massive. Poiché per campioni massivi la discesa repentina della temperatura può dare luogo a stress da shock termico, ovvero stress derivanti da gradienti di temperatura interni, i dischi tagliati e poi trattati con vari cicli termici sono stati messi a confronto con dischi tagliati da barre che hanno subito il trattamento di ciclo termico precedentemente. In questo modo si è voluto verificare anche l'effettiva natura dello stress, ovvero derivante dalla presenza di una microstruttura interna.

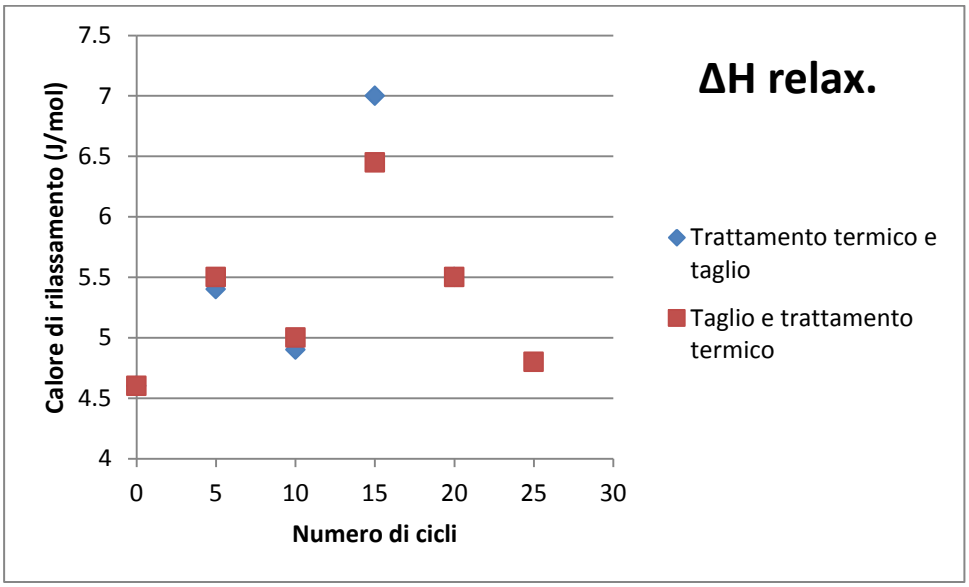

Grafico 6.3.1.4: valori del calore di rilassamento per campioni trattati termicamente e poi tagliati (blu) e campioni tagliati e trattati termicamente (rosso).

Si nota un andamento simile a quello riscontrato per i nastri, inoltre appare che gli stress termici derivanti da eventuali gradienti di temperatura non influiscono significativamente sul calore di rilassamento. In questo caso il massimo del calore di rilassamento si verifica a 15 cicli; questo è probabilmente da imputarsi al fatto che i campioni *bulk* hanno meno volume libero essendo prodotti con minori velocità di raffreddamento ed è necessaria una maggiore stimolazione per indurre un effetto di ringiovanimento.

6.3.1.3 Effetto di "ricottura" alla temperatura criogenica

In letteratura Chen et al. riportano che è possibile indurre la nucleazione di nanocristalli nella struttura di un vetro metallico "ricuocendo" il materiale per centinaia di ore a 77K (azoto liquido).

Nel seguente grafico, Grafico 6.3.1.5 si evidenzia che l'effetto di ringiovanimento è dovuto esclusivamente al cambiamento omogeneo della temperatura del campione ripetuto per un relativamente piccolo numero di volte. È stata infatti svolta una comparazione tra nastri di vetro metallico che rispettivamente hanno subito 10 cicli termici e una ricottura a 77K di 240 minuti. Entrambi poi sono stati comparati con un campione as-cast.

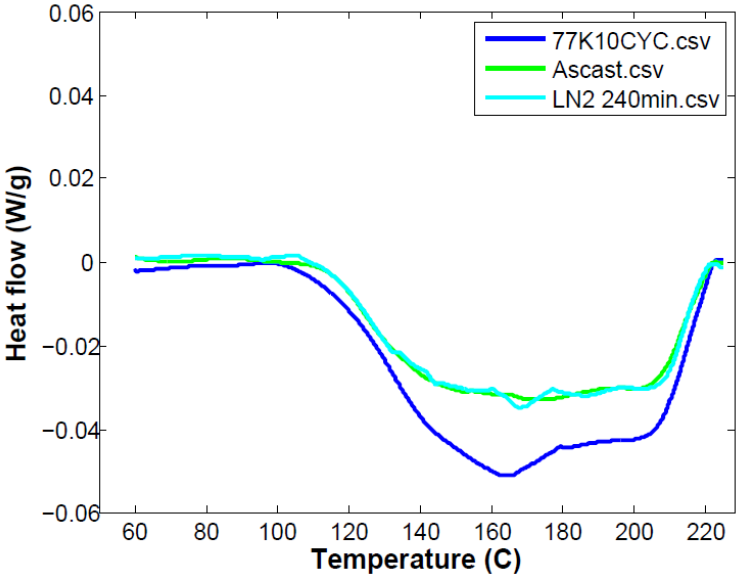

Grafico 6.3.1.5: spettro DSC di rilassamento per campioni che hanno subito 10 cicli termici in azoto liquido, ricottura in azoto liquido di 240 minuti e un campione non trattato.

Il campione ricotto appare molto simile al campione non trattato mentre il trattamento di ciclo termico ha indotto un aumento nel volume libero del materiale e un conseguente aumento del fenomeno di rilassamento.

6.3.2 Test di compressione

L'introduzione di volume libero nella struttura di un vetro metallico comporta una, anche notevole, modificazione delle proprietà fisiche, tra cui quelle meccaniche. Infatti ad una struttura più aperta si associa generalmente una deformazione più omogenea, sia essa per flusso viscoso o per nucleazione e propagazione di un superiore numero di *shear bands* che distribuiscono la deformazione più equamente su tutto il campione.

Nel test presente campioni di vetro metallico di composizione $Cu_{46}Zr_{46}Al_7Gd_1$ sono stati preparati in forma di parallelepipedo di opportune dimensioni, sono stati lappati per raggiungere finiture adeguate, 0.3 µm, e hanno infine subito un trattamento termico di 10 cicli tra 293K e 77K.

Sono stati testati e trattati termicamente tre differenti stati, lo stato as-cast, una parziale ricottura (400°C per 1 ora) e una ricottura più profonda (410°C per 1 ora e mezza). I risultati ottenuti dalle prove di compressione sono riportati nei grafici sottostanti, Grafico 6.3.2.1-6.3.2.3.

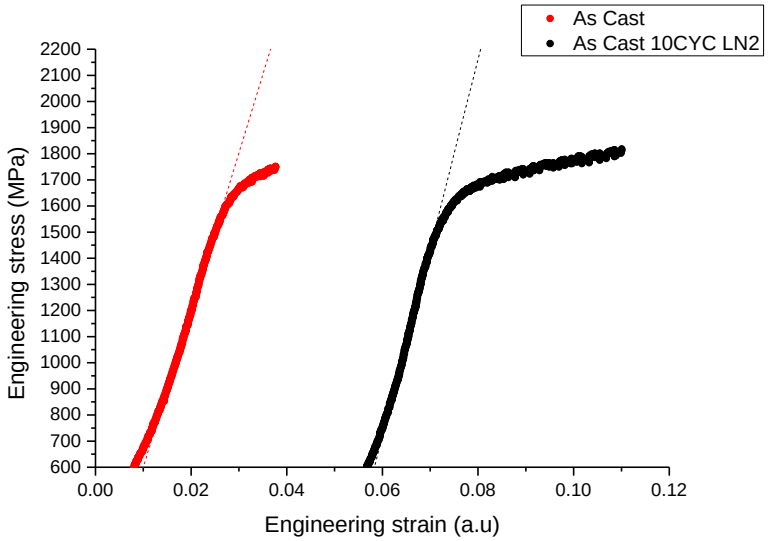

Grafico 6.3.2.1: curve ingegneristiche di sforzo e deformazione per i campioni as-cast.

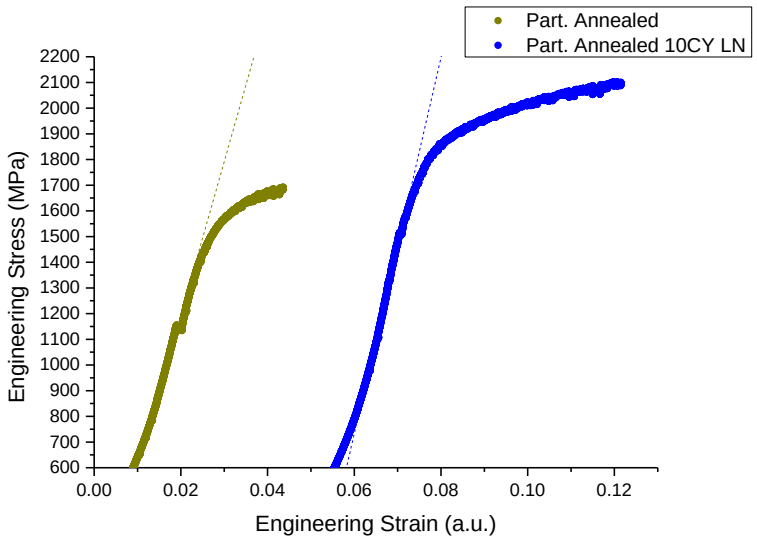

Grafico 6.3.2.2: curve ingegneristiche di sforzo e deformazione per i campioni parzialmente ricotti.

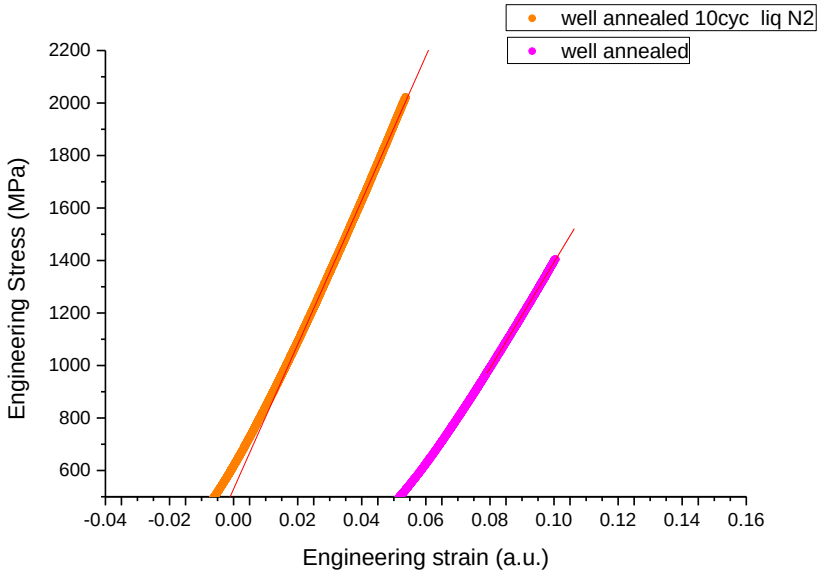

Grafico 6.3.2.3: curve ingegneristiche di sforzo e deformazione per i campioni più profondamente ricotti.

Tranne che per il Grafico 6.3.2.3, si può notare un comportamento più duttile per i campioni che hanno subito il trattamento termico ciclico. Nella tabella seguente vengono riportati le caratteristiche delle varie curve sforzo-deformazione, Tabella 6.3.2.1:

	Tensione di snervamento (MPa)	**Deformazione plastica (%)**
as-cast	1560	2.2
as-cast+10cicli	1430	6.1

parz. ricotto	1358	2.7
parz. ricotto+10cicli	1500	7.9
compl. ricotto	1405	0
compl. ricotto+10cicli	1620	0

Tabella 6.3.2.1: tensione di snervamento e deformazione plastica per i vari campioni testati.

Il trattamento termico non comporta solamente una maggiore duttilità, infatti analizzando il regime plastico in particolare la quantità e l'ampiezza della caduta degli sforzi si è riscontrato che per i campioni trattati il numero di queste cadute è sensibilmente più elevato. Oltre a ciò anche l'ampiezza di queste cadute di sforzo è minore per i campioni trattati. Se ne deduce quindi che la deformazione è avvenuta per formazione di un maggiore numero di shear bands, la loro densità è aumentata, e ciò spiega il netto aumento della deformazione plastica sostenuta. La deformazione infatti risulta meno localizzata per effetto dell'introduzione nella struttura di un maggior numero di "difetti", STZs, che promuovono la nucleazione e la propagazione di numerose shear bands. Questo incremento nella popolazione di STZs è promosso dagli sforzi che si generano per effetto del cambio ciclico di temperatura; la deformazione termica per questo caso quindi può definirsi non affine.

6.3.3 Indentazioni

Nanoindentazioni e indentazioni Vickers sono state eseguite sui vetri metallici di composizione $La_{55}Al_{25}Ni_{20}$, $La_{55}Al_{35}Ni_{10}$, ovvero sia su *ribbon* che *bulk*. Nanoindentazioni sono state svolte in grande numero su campioni trattati e as-cast. La specifiche della prova sono le seguenti: carico massimo pari a 40mN, velocità di carico 0.5mN/s e tempo di permanenza al carico massimo pari a 60s. Nei Grafici 6.3.3.1 e 6.3.3.2 sono riportate distribuzione cumulative della tensione di snervamento per vari nastri testati.

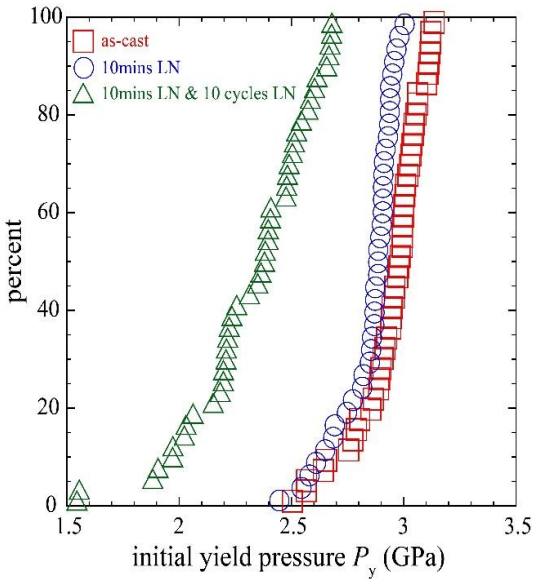

Grafico 6.3.3.1: distribuzione cumulativa della tensione di snervamento per ribbon as-cast, ricotto in azoto liquido per 10 minuti e che ha subito 10 cicli in azoto liquido.

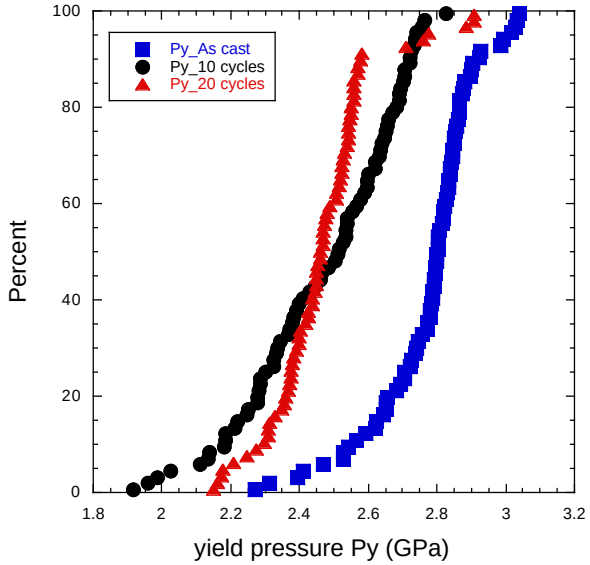

Grafico 6.3.3.2: distribuzione cumulativa della tensione di snervamento per ribbon as-cast, e che ha subito 10 cicli e 20 cicli in azoto liquido.

Si può notare ancora una volta che è presente un effetto di ringiovanimento e che esso si esplica maggiormente nella riduzione della tensione di snervamento. E ciò è in accordo con quanto dedotto e osservato dalle analisi precedenti, ovvero che il trattamento termico realizza un'attivazione delle STZs e un conseguente aumento del loro numero e/o della loro dimensione.

Nel grafico 6.3.3.2 inoltre si può notare come la deformazione termica non affine prodotta dal trattamento termico introduce di fatto un danno nella struttura, e questo danno viene

accumulato all'aumentare del numero di cicli. Si nota infatti un'ulteriore diminuzione della tensione di snervamento for 20 cicli, al contrario di quanto misurato con analisi calorimetriche.

Un andamento del tutto analogo si è riscontrato anche per il vetro metallico a base La *bulk* , seppure la diminuzione della tensione di snervamento è apparsa meno marcata. Per questo campione si è osservato un aumento della lunghezza del primo evento plastico, pop-in, all'aumentare del numero di cicli e anche per valori di questi che altre analisi non avevano captato (DSC). Tabella 6.3.3.1 riporta questi valori come % del numeri di questi eventi che mostra una certa lunghezza.

	% pop-in				
	>1 nm	**1.5-2nm**	**2-3 nm**	**3-5 nm**	**>5 nm**
as-cast	78	**13**	**33**	20	11
5 cicli	81	**25**	0	**40**	0
15 cicli	94	7	**25**	**48**	2
30 cicli	94	4	**41**	2	**44**

Tabella 6.3.3.1: percentuale del numero di pop-in che presentano una determinata lunghezza all'aumentare del numero di cicli termici subiti.

Misure di durezza Vickers sono state effettuate per osservare le caratteristiche delle zone deformate e l'estensione di tali zone. Nella tabella sottostante, Tabella 6.3.3.2, sono riportati i valori di durezza calcolati. Si nota un leggero decremento della durezza all'aumentare del numero di cicli, probabilmente imputabile ad un effetto di ringiovanimento.

	as-cast	**5 cicli**	**10 cicli**	**15 cicli**
HV media	235.5	226.1	229.7	224.4
Deviazione standard	1.9	3.6	2.9	1.9
decremento % rispetto a as-cast	--	4%	3%	5%

Tabella 6.3.3.2: durezza vickers media, relativa deviazione standard e decremento % rispetto allo stato non trattato all'aumentare del numero di cicli per campione bulk di vetro metallico a base di La.

Il decremento di durezza è relativamente piccolo, ma dall'osservazione con microscopio ottico delle impronte vickers si può notare la presenza di *shear bands* che hanno raggiunto la superficie solo nelle impronte dopo il trattamento termico, Figura 6.3.3.1.

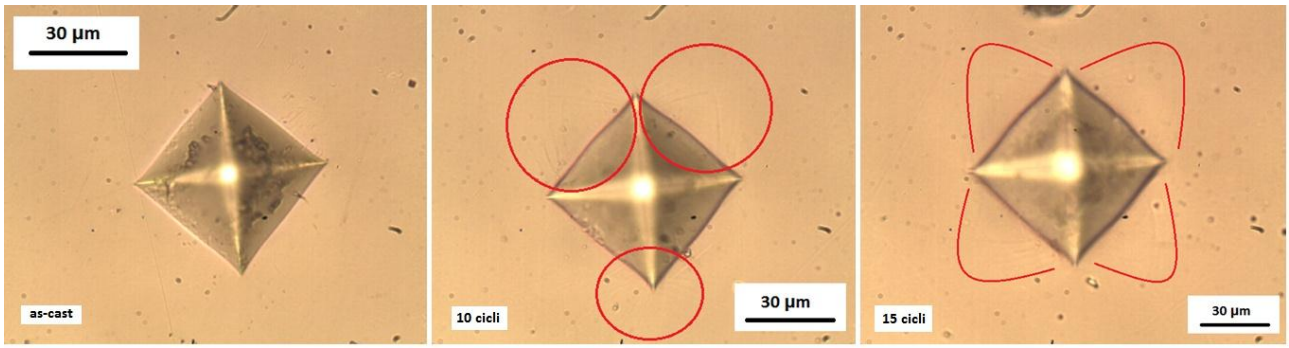

Figura 6.3.3.1: micrografie 500x di impronte vickers effettuate dopo vari cicli termici; da sinistra as-cast, 10 cicli e 15 cicli. Cerchiate o evidenziate in rosso sono shear bands e/o le zone deformate.

Si osservato che la densità di *shear bands* cresce progressivamente con il numero di cicli termici, a dimostrazione del fatto è in atto un meccanismo di accumulo del danneggiamento indotto dai cicli termici. La presenza di *shear bands* è di per se già molto significativa perché dimostra che il regime elastico/elasto-plastico è stato ridotto come conseguenza di una maggiore facilità di flusso plastico (abbassamento del limite elastico).

Dato che anche la zona deformata attorno alle indentazione sembra estendersi con il numero di cicli sono state eseguite misure AFM sulle indentazioni stesse. È risultato che tali indentazioni presentano una maggiore estensione di tali zone sia verticalmente che longitudinalmente.